

Mahidol University Center for Scientific Computing

## 2015 Midyear Report

C. Boonyasiriwat, T. Chanthanasaro, H. Intarak, P. Niranartlumpong,  
N. Pongchanwit, P. Pukhamwong, N. Rotchananirunkit, J. Sinsawasmongkol,  
P. Sitsungnoen, K. Supa, and W. Thongyoy

July 15, 2015



# Contents

Least-squares finite difference operator <i>Wisart Thongyoy and Chaiwoot Boonyasiriwat</i> .....	1
Simulation of solitary wave at an artificial coastline using FUNWAVE <i>Pawin Sitsungnoen and Chaiwoot Boonyasiriwat</i> .....	19
Simulation of electromagnetic cloaking using transformation optics <i>Panuwat Pukhamwong and Chaiwoot Boonyasiriwat</i> .....	31
Simulation of flow past a square cylinder <i>Nattapon Pongchanwit and Chaiwoot Boonyasiriwat</i> .....	39
Simulation of smoke in two dimensions using finite difference method in MATLAB <i>Thanakorn Chanthanasaro and Chaiwoot Boonyasiriwat</i> .....	43
Simulation of Rayleigh-Taylor instability in two dimensions using finite difference method in MATLAB <i>Kanisorn Supa and Chaiwoot Boonyasiriwat</i> .....	49
A new chaotic circuit based on a single 555 timer IC <i>Peera Niranarthumpong, Chaiwoot Boonyasiriwat, and Michael A. Allen</i>	55
Mathematical modeling of magnetic pendulum <i>Harirak Intarak and Chaiwoot Boonyasiriwat</i> .....	65
PML formulation for full-waveform modeling of P-SV wave propagation <i>Chaiwoot Boonyasiriwat</i> .....	73



## MCSC MIDYEAR REPORT 2015

This technical report summarizes the midyear 2015 research accomplishments of the researchers of the Mahidol University Center for Scientific Computing (MCSC). Our research includes numerical simulations of fluid flows, seismic, electromagnetic, and tsunami wave propagation, and dynamical systems.

Currently, MCSC members are composed of one lecturer, one administrative staff, one software developer, six Ph.D. students, five M.Sc. students, and three B.Sc. students.

Chaiwoot Boonyasiriwat and colleagues  
Mahidol University Center for Scientific Computing  
Department of Physics, Faculty of Science, Mahidol University  
272 Rama VI Road, Ratchathewi, Bangkok 10400, THAILAND  
Phone: 66-8-0938-4132  
Fax: 66-2-354-7159  
Email: [chaiwoot@gmail.com](mailto:chaiwoot@gmail.com)  
Website: <http://mcsc.sc.mahidol.ac.th>



# Least-Squares Finite Difference Operator

Wisart Thongyoy and Chaiwoot Boonyasiriwat

## ABSTRACT

Finite difference (FD) method is a numerical method for solving partial differential equations (PDEs). When it is applied to solve the wave equation with a large grid size, numerical dispersion can occur. To minimize the numerical dispersion, one can use least-squares optimization to obtain FD coefficients with higher accuracy. Zhang and Yao (2013a) suggested to use simulated annealing, a global optimization method, for optimization in the infinity norm. However, this method is very time consuming. In this work, we show that optimized FD coefficients with comparable accuracy to the previous work can be obtained with much less computation time using least-squares optimization. Another benefit of least-squares optimization in this case is that the resulting problem is linear and the global solution can be obtained easily. We also observe that both our results and the results from Zhang and Yao (2013a) have high dispersion coefficient error at low wavenumbers, so we construct an objective function based on dispersion coefficient. The result shows smaller dispersion error, but the range of wavenumber coverage is also narrower. Finally, we also show the efficiency and effectiveness of optimized FD compared to conventional FD in a synthetic study.

## INTRODUCTION

Finite difference (FD) method is one of the most widely used methods for solving PDEs. The main drawback of the conventional FD method is that when it is applied to wave propagation problem using a coarse grid, large numerical dispersion occur. One of the methods to improve the conventional FD method was proposed by Zhang and Yao (2013a) and Zhang and Yao (2013b). The idea is to seek for a set of FD coefficients that minimizes numerical dispersion. They constructed an objective function to

evaluate the accuracy of the optimized FD operator, then tried to select a proper error limitation and build three criteria that the optimized FD operators should obey. Finally, they applied the simulated annealing algorithm (proposed by Kirkpatrick et al. (1983)) to search for the operator that best satisfies the constraint.

In this work, we try to find a better way to seek for a group of optimized coefficients. Since the simulated annealing algorithm is based on randomness, the searching for the FD operator can be a lot slower than gradient methods such as Newtons, and Conjugate gradient. First, we construct a new objective function based on least-squares by transforming an approximation to the Fourier domain. The results show that our least-squares optimization give a comparable results as the previous work with a little narrower wavenumber coverage. The simulations of 2D wave propagation in homogeneous medium also suggested almost the same results as previous work, optimized FD can reduce numerical dispersions. We also observe a dispersion coefficient of our results and the result of Zhang and Yao (2013a), we found that the dispersion coefficient of both results have a high error event at small wavenumbers.

According to the disadvantages, the high error at small wavenumber, we construct a new objective function with dispersion coefficient based. The accuracy analysis show that this dispersion based objective function give narrower wavenumber coverage than the original objective function, but, the error is smaller due to the vary of error which is small in a small wavenumber region and larger when it approach maximum wavenumber coverage. The simulations of 2D wave propagation in homogeneous medium show that the dispersions of dispersion based method is higher than original one, however, it can better conserve the shape of wavelet.

Finally, we do an efficiency analysis to describe the improvement of optimized FD. The numerical results show that optimized FD have to use grid points per wavelength only 60% of that of conventional method. However, the

simulation result show that the optimized FD is comparable to conventional method when using grid points per wavelength at 90%.

Unexpectedly, we also found the our work is not a novel work, our first objective function was also published by Liu (2013), they also discuss about the relation of changing upper limit of wavenumber and error-threshold. Our dispersion based method was also published by his paper with a bit difference of designing the objective function.

### CONVENTIONAL FINITE-DIFFERENCE OPERATOR

Based on the Taylor's expansion, the Finite-Difference(FD) method can approximate derivatives by truncation of higher-order terms. For example, the approximation by FD of first and second derivative with second-order approximation (the error term), respectively, are

$$\frac{df(x)}{dx} = \frac{1}{\Delta x} \frac{f(x + \Delta x) - f(x - \Delta x)}{2} + \mathcal{O}(\Delta x^2), \quad (1)$$

$$\frac{d^2 f(x)}{dx^2} = \frac{1}{(\Delta x)^2} [f(x + \Delta x) - 2f(x) + f(x - \Delta x)] + \mathcal{O}(\Delta x^2), \quad (2)$$

where  $\Delta x$  is grid interval of spatial direction  $x$ , and  $\mathcal{O}(\Delta x^n)$  is the error of approximation. We can also write these approximations in a more generalized form as

$$\frac{d^m f(x)}{dx^m} \approx \frac{1}{(\Delta x)^m} \sum_{n=-N/2}^{N/2} b_n f_n, \quad (3)$$

where  $m$  is the order of derivative,  $f_n = f(x + n\Delta x)$ ,  $b_n$  are constant FD coefficients, and  $N$  is the order of approximation. In this work, we aim to seek for an optimized set of FD coefficients ( $b_n$ ).

### SPATIAL DERIVATIVE IN THE FOURIER DOMAIN

We transform the spatial derivatives into the wavenumber domain as follows (see Appendix A)

$$\frac{\partial^m f(x)}{\partial x^m} \Rightarrow (ik_x)^m F(k_x), \quad (4)$$

where  $k_x$  is wavenumber and  $i = \sqrt{-1}$ . By using Fourier transform, we can exactly evaluate the spatial derivative in wavenumber domain. Next, we transform equation 3 into the wavenumber domain for  $m = 1$  and  $m = 2$ , respectively as (see Appendix A)

$$ik_x \approx \frac{i}{\Delta x} \sum_{n=-N/2}^{N/2} b_n \sin(nk_x \Delta x), \quad (5)$$

$$-k_x^2 \approx \frac{1}{(\Delta x)^2} \sum_{n=-N/2}^{N/2} b_n \cos(nk_x \Delta x). \quad (6)$$

### OPTIMIZED FINITE DIFFERENCE OPERATOR BY LEAST-SQUARES

#### Optimized Finite-Difference Operator Through Least-Squares Inversion

We seek for coefficients  $b_n$  of optimized FD operator that minimized the least-squares objective functions

$$E = \frac{1}{2} \left( k_x \Delta x - \sum_{n=-N/2}^{N/2} b_n \sin(nk_x \Delta x) \right)^2, \quad \text{for } m = 1, \quad (7)$$

$$E = \frac{1}{2} \left( -k_x^2 (\Delta x)^2 - \sum_{n=-N/2}^{N/2} b_n \cos(nk_x \Delta x) \right)^2, \quad \text{for } m = 2. \quad (8)$$

Now we can see that our objective functions depend only on one value of  $k_x$ , so if any value of  $k_x$  is used with these objective function we will get a difference group of coefficient based on a value of  $k_x$ . However, we can eliminate this disadvantage by summing up all the objective functions from difference value of  $k_x$  that we want to minimize, this brings the new objective function as follows. For  $m = 1$ ,

$$E = \sum_i^{k_c} \frac{1}{2} \left( k_{(x,i)} \Delta x - \sum_{n=-N/2}^{N/2} b_n \sin(nk_{(x,i)} \Delta x) \right)^2. \quad (9)$$

For  $m = 2$ ,

$$E = \sum_i^{k_c} \frac{1}{2} \left( -k_{(x,i)}^2 (\Delta x)^2 - \sum_{n=-N/2}^{N/2} b_n \cos(nk_{(x,i)} \Delta x) \right)^2, \quad (10)$$

where  $k_c$  is a selectable upper limit. Now our objective functions can calculate a group of coefficients that minimized in some region of  $k_x (0 \sim k_c)$ , but what  $\Delta x$  should be. By considering the range of value of  $k_x$ , for any signal, the greatest wave number that can be detected is the Nyquist wavenumber which is equal to  $k_{(x,max)} = \pi/\Delta x$ , and the minimum value of  $k_x$  is  $k_{(x,min)} = 0$ , thus,  $k_x \in [0, \pi/\Delta x]$ . Here, we define a new variable  $k = k_x \Delta x$ , so our new variable has a range as follow  $k \in [0, \pi]$ . Then we substitute  $k_x \Delta x$  with  $k$ , which give our final objective function as

$$E = \sum_i^{k_c} \frac{1}{2} \left( k_i - \sum_{n=-N/2}^{N/2} b_n \sin(nk_i) \right)^2, \quad \text{for } m = 1, \quad (11)$$

$$E = \sum_i^{k_c} \frac{1}{2} \left( -k_i^2 - \sum_{n=-N/2}^{N/2} b_n \cos(nk_i) \right)^2, \quad \text{for } m = 2. \quad (12)$$

## Optimization by linear least-squares

Generally the least-squares optimization problem can be solved by using conventional gradient like methods such as steepest descend or Newton's method, but for our problem the Hessian matrix is constant which bring a linear problem. Therefore, the problem can be solved easily by solving a matrix equation. Before going through these matrix equations, the two criteria are set up based on the conventional FD, (1) the coefficient should be real number  $b_n \in R$ , and the operator should be symmetric for even order derivatives (i.e.,  $b_{-n} = b_n$ ) and be anti-symmetric for odd order derivatives (i.e.,  $b_{-n} = -b_n$ ); (2) for even order derivatives,  $\sum_{n=-N/2}^{N/2} b_n = 0$ , this comes from the case of  $k_x = 0$  (i.e.  $k_x = 0$  for  $-k_i^2 = \sum_{n=-N/2}^{N/2} b_n \cos(nk_i)$ ). For odd derivative, the equation is automatically true since  $\sin(0) = 0$ .

By using these rules, the number of coefficients that we have to seek for are reduced to only  $N/2$ , since  $b_0 = -2 \sum_{n=1}^{N/2} b_n$  for even derivatives and  $b_0 = 0$  for odd derivatives. Thus we can find the whole operator by purely determine the independent coefficients  $b_1 \sim b_{N/2}$  (or  $b_{-N/2} \sim b_{-1}$ ).

Thus, the matrix equation for first derivative is

$$2 \begin{pmatrix} \sin(k_0) & \sin(2k_0) & \sin(3k_0) & \cdots & \sin(Nk_0/2) \\ \sin(k_1) & \sin(2k_1) & \sin(3k_1) & \cdots & \sin(Nk_1/2) \\ \vdots & \vdots & \vdots & \ddots & \vdots \\ \sin(k_c) & \sin(2k_c) & \sin(3k_c) & \cdots & \sin(Nk_c/2) \end{pmatrix} \begin{pmatrix} b_1 \\ b_2 \\ \vdots \\ b_{N/2} \end{pmatrix} = \begin{pmatrix} k_0 \\ k_1 \\ \vdots \\ k_c \end{pmatrix}, \quad (13)$$

and for the second derivative is

$$-2 \begin{pmatrix} \cos(k_0) & \cos(2k_0) & \cos(3k_0) & \cdots & \cos(Nk_0/2) \\ \cos(k_1) & \cos(2k_1) & \cos(3k_1) & \cdots & \cos(Nk_1/2) \\ \vdots & \vdots & \vdots & \ddots & \vdots \\ \cos(k_c) & \cos(2k_c) & \cos(3k_c) & \cdots & \cos(Nk_c/2) \end{pmatrix} \begin{pmatrix} b_1 \\ b_2 \\ \vdots \\ b_{N/2} \end{pmatrix} = \begin{pmatrix} k_0^2 \\ k_1^2 \\ \vdots \\ k_c^2 \end{pmatrix} \quad (14)$$

In this work, instead of using the real value of  $k$  we use  $k$  as percent of the maximum value ( $\pi$ ), thus,  $k_0 = 0$  and  $k_{i+1} = k_i + dk$ , where  $dk = 0.01$ , and  $k_{max} = 100$ .

## The error threshold

As we can see from the results of Zhang and Yao (2013a), the effect of the optimization is to slightly vibrate the error in the region of small values of  $k$ , here the limitation of the vibration's amplitude is defined as our error threshold. The job is to seek for  $k_c$  that obey this rule. To compare our result with the previous work, the error threshold is set to be  $\epsilon = 0.0001$ .

## Numerical results

Figure 1 and Figure 2 show the results of plotting between percentage of Nyquist wave number and the error of approximation of 1st and 2nd derivative respectively. We can see that, for both method, the error curves of optimized FD coefficients vibrate within the error limitation. The error curves proposed from Zhang and Yao (2013a) can cover wavenumber a bit greater than optimization by

least-squares. However, the amplitude of the vibration before the last peak of least-square is a bit less than Zhang and Yao (2013a).

## 2D wave propagation in homogeneous medium

To discuss further about accuracy, we simulate a 2D wave that propagate in homogeneous medium with condition show in Table 3, where the appearance of Ricker wavelet is shown in Figure 3.

To analyze the dispersions, we adopt a 2D wave simulation by Spectral method which has very high accuracy and can be implied as an exact solution (very small dispersions).

Figure 4 show the comparison of 2D wave propagation between conventional FD 12th-order, Spectral method, conventional FD 8th-order, and optimized FD 8th-order. We can see that when using the same FD order, 8th-order, the result show that optimized FD gives smaller dispersions than conventional FD, its dispersions also comparable to the result of conventional FD 12th-order. However, we also observed that optimized FD give extra wavelets near the main wavelet as can be seen as extra lines next to the main wavelet. This should come from the error that we accepted (error-threshold) when we designed an objective function.

To see the effect of the error-threshold, we plot the comparison between 8-th order optimized FD with various error threshold, which is shown in Figure 5.

From Figure 5, the increasing of the error-threshold, which means the increasing of wavenumber coverage, can reduce the dispersion events, but, the form of wavelet also be out of shape as much as the increasing of the error-threshold.

## Advantages and flexibility of optimization by Least-Squares

Since the optimization by least-squares can be prepared by solving a matrix equation, the optimization uses less time than random method such as simulated annealing. The optimization by least-squares also flexible to choose the error-threshold by changing the value of  $k_c$  as show in Figure 6. The figure shows the accuracy of 8th-order FD of 2nd derivative, the use of less  $k_c$  automatically decreases the error-threshold. Thus, we can find the group of optimized FD coefficients that fit to any value of error-threshold. The minimum value of error-threshold is the conventional FD. However, the least error-threshold also brings the least coverage of wave number as well.

## Dispersion analysis

One of the best way to analyze the accuracy of FD is to use a dispersion analysis. By considering the 1D frequency-domain scalar wave equation, and one-way frequency-domain

scalar wave equation

$$\frac{\partial^2 P}{\partial x^2} = -\frac{\omega^2}{v^2} P, \quad \text{two-way wave equation,} \quad (15)$$

$$\frac{\partial P}{\partial x} = i\frac{\omega}{v} P, \quad \text{one-way wave equation,} \quad (16)$$

where  $v$  is the velocity,  $\omega$  is the angular frequency, and  $P$  is the scalar wave field. The dispersion coefficient of these two equations can be written as (see Appendix B). For two-way wave equation,

$$\frac{v_{ph}}{v} = \frac{\omega/k_x}{v} = \left( -\frac{b_0 + 2 \sum_{n=1}^{N/2} b_n \cos(nk)}{k^2} \right)^{1/2}. \quad (17)$$

For one-way wave equation,

$$\frac{v_{ph}}{v} = \frac{\omega/k_x}{v} = \frac{2 \sum_{n=1}^{N/2} b_n \sin(nk)}{k}, \quad (18)$$

where  $v_{ph}$  is phase-velocity, and  $k = k_x \Delta x$ . To see the accuracy of optimized FD, we plot the dispersion coefficient that used optimized coefficients with percentage of Nyquist wave number.

Figure 7 and Figure 8 show the disadvantage of this method, we can see that in the range of low value of  $k$  there are a huge error of dispersion coefficient. The error at the low value of  $k$  can effect a very long wavelength ( $k = 2\pi/\lambda$ ), which can bring a lot of error to an approximation.

## AN OBJECTIVE FUNCTION BASED ON DISPERSION COEFFICIENTS

To eliminate the disadvantage, one can construct a new objective function based on dispersion analysis. Since  $V_{ph}/v$  should equal to one, then we can construct the objective functions as follows. For two-way wave equation,

$$E(k) = \left( 1 + \frac{b_0 + 2 \sum_{n=1}^{N/2} b_n \cos(nk)}{k^2} \right)^2. \quad (19)$$

For one-way wave equation,

$$E(k) = \left( 1 - \frac{2 \sum_{n=1}^{N/2} b_n \sin(nk)}{k} \right)^2. \quad (20)$$

For two-way wave equation, we use  $(V_{ph}/v)^2 = 1$  instead to keep the linearity of the objective function. Then, as before, by summing up all objective function from difference value of  $k$ , we get, for two-way wave equation,

$$E(k_i) = \sum_i^{k_c} \left( 1 + \frac{b_0 + 2 \sum_{n=1}^{N/2} b_n \cos(nk_i)}{k_i^2} \right)^2, \quad (21)$$

and for one-way wave equation

$$E(k_i) = \sum_i^{k_c} \left( 1 - \frac{2 \sum_{n=1}^{N/2} b_n \sin(nk_i)}{k_i} \right)^2. \quad (22)$$

## Numerical results

To compare the dispersion based and the original one, we seek for a group of FD coefficients by using dispersion based objective function, but, we observe the error-threshold by passing the calculated groups of FD coefficients through equation 11 or 12, again we set the error-threshold equal to 0.0001.

Figure 9 and 10 show the accuracy comparison between our original least-squares and dispersion based, both figure show the characteristic of both methods in the same way, we can see that dispersion based method gives less wavenumber coverage than the original one. Furthermore, the characteristic of the vibration is difference, for the original least-squares, the error vibrate almost steadily. However, for dispersion based method, the amplitude of the vibration increases exponentially with the increasing of wavenumber. The another interesting point is that dispersion based method gives a very low error in the low region of wavenumber.

Figure 11 and 12 show the dispersion coefficient comparison between our original least-squares and dispersion based. The results show the successful of dispersion based method since the the error of dispersion coefficient in the low region of wavenumber are decreased. However, the wavenumber coverage also decrease, and some of the highest peak error also increase, for example, the peak error of 4th- and 6th-order of both derivative.

## 2D wave propagation in homogeneous medium

To analyze further, as in Chapter 3, we simulate 2D wave which propagate in homogeneous with the properties shown in Table 3.

Figure 13 compare the dispersions and wavelet between conventional FD 8th-order, Spectral method, optimized FD with dispersion coefficient based 8th-order, and original optimized FD 8th-order. The result show that dispersion based optimized FD give dispersions less than conventional method and comparable to original optimized FD, but, has a bit greater dispersions. To discuss further, as before, we increase the error-threshold for both methods as show in Figure 15 for dispersion based and 5 which is replotted in 14.

By comparing Figure 14 and 15, we can see that the dispersions of dispersion based optimized FD are decreased less than original optimized FD with the increasing of the error-threshold, but, it is clear that dispersion based method can better conserve the shape of wavelet than original method.

## EFFICIENCY ANALYSIS

### Numerical results

According to our results, we can see that optimized FD brings a greater wavenumber coverage to the approximation. To measure the improvement, we compare the value of grid points per wavelength which is the value that can

implies to the computational time (the more grid point the more computational time) or the accuracy of approximation. Since the wavenumber coverage from Zhang and Yao (2013a) and the original least-squares are almost the same, and we want to analyze only the effect of optimization FD compare to conventional FD, then the results from Zhang and Yao (2013a) are omitted.

Table 6 and 7 show the amount of grid points per wavelength, from the result, it clearly that optimized FD (both methods) uses a calculation time approximately only 60% of the conventional method, or if we keep the amount of grid points constant, it bring greater accuracy. This amount of grid points per wavelength can also change by changing the error-threshold, for example, if greater error is accepted the grid points per wavelength is fewer.

## 2D wave propagation in homogeneous medium

As we before, again, we discuss further by considering 2D wave which propagates in homogeneous medium. In this section, we vary a grid size ( $\Delta x$ ) which implies to grid points per wavelength by the relation grid points/wavelength =  $\lambda/\Delta x$ . The numerical results suggested that the grid points per wavelength of optimized FD (both method) is approximately 60% of that of conventional FD, so we simulate the 2D wave by using 8th-order convention FD with smaller grid size to compare with the optimized FD with grid size equal to 5 m.

Figure 16 and 17 show the dispersions comparison between conventional FD 8th-order with grid spacing 3.5, 4, and 4.5m with optimized FD 8th-order with grid spacing 5m. The results show that, for both methods of optimization, the dispersions of optimized FD 8th-order with grid spacing 5m are comparable to the dispersions of conventional FD 8th-order with grid spacing 4.5m, this result suggest that the grid spacing or grid points per wavelength of optimized FD should be approximately 90% of that of conventional FD instead of 60% which the numerical results suggested.

## CONCLUSION

We have tried to construct new approaches that can overcome disadvantages of searching a minimized group of FD coefficients by simulated annealing, suggested by Zhang and Yao (2013a) and Zhang and Yao (2013b), which is computational expensive. We construct a objective function based on least-square optimization then setting up two criterias and use the virtue of nyquist wavenumber. Finally, we construct an objective function and found that it is a linear problem which can be solved easily by solving a matrix equation, this bring a very low calculation time. After comparing our result with Zhang and Yao (2013a), with the same error-threshold  $\epsilon = 0.0001$ , we found that our results can cover wavenumber a bit less than Zhang and Yao (2013a) but the overall error is lower. Accordingly, the simulation result also suggest that optimized FD can reduce the dispersions event of simulation. We

also found the advantages and flexibility of optimization by least-squares, first, it is very fast compare to simulated annealing. Second, it can easily change the error-threshold by changing the upper limit of interested region of wavenumber( $k_c$ ). Thus, we can construct a group of FD coefficients that best fit to any error-threshold. To discuss further, we analyze the results by using dispersion coefficient, the analysis show that our results and the results of Zhang and Yao (2013a) have a high error of dispersion coefficient in a low value region of wavenumber.

The disadvantage of high error is solved by constructing a new objective function based on dispersion coefficients, this objective function is still linear and can be solved by matrix equation, the results show the successful of the objective function, the errors in the low value region of wavenumber are decreased. The simulation results show that the original method can reduce dispersions better than dispersion based method, but the dispersion based can better conserve the shape of wavelet.

For the efficiency, we compare amount of grid points per wavelength of conventional and optimized FD, the results show that the calculation time of optimized FD is about 60% of the conventional method for  $\epsilon = 0.0001$ . However, the simulation results suggest that it should be 90% instead, this should be come from the effect of error that we accept to our objective function (error-threshold).

To sum up, optimized FD can reduce dispersions of increase accuracy of approximation of PDEs. We construct to objective function one based on error in Fourier domain, and one based on dispersion coefficient, both method bring lower dispersion and higher accuracy than conventional method. However, when we compare between these two methods we found that original method is better when reducing dispersion, but dispersion based is better for conserve the shape of wavelet or the answer.

Finally, we also found the our work is not a novel work, our first objective function was also published by Liu (2013), they also discuss about the relation of changing upper limit of wavenumber and error-threshold. Our dispersion based method was also published by his paper with a bit difference of designing the objective function.

## REFERENCES

- Cohen, G. C., 2002, Higher-order numerical methods for transient wave equations: Springer.
- Kirkpatrick, Gelatt, and Vecchi, 1983, Optimization by simulated annealing: *Science*, **220**, 671–680.
- Liu, Y., 2013, Globally optimal finite-difference schemes based on least squares: *Geophysics*, **78**, T113–T132.
- Zhang, J. and Z. Yao, 2013a, Optimized explicit finite-difference schemes for spatial derivatives using maximum norm: *Journal of Computational Physics*, **250**, 511–526.
- , 2013b, Optimized finite-difference operator for broadband seismic wave modeling: *Geophysics*, **78**, A13–A18.

Table 1: Finite-difference coefficients for 1st derivative.

	4th-Order	6th-Order	8th-Order	10th-Order	12th-Order
$k_c$	17.82	30.87	41.47	49.73	56.16
$k$ coverage	16.97	30.02	40.7	49.05	55.55
$b_1$	0.67827896	0.77700725	0.83932599	0.88039931	0.90832181
$b_2$	-0.08933900	-0.17303105	-0.24273904	-0.29712380	-0.33830663
$b_3$		0.02310905	0.05931084	0.09864430	0.13502083
$b_4$			-0.00800178	-0.02481461	-0.04667635
$b_5$				0.00347582	0.01209163
$b_6$					-0.00178613

Table 2: Finite-difference coefficients for 2nd derivative.

	4th-Order	6th-Order	8th-Order	10th-Order	12th-Order
$k_c$	25.42	39.20	49.91	58.00	64.16
$k$ coverage	24.50	38.33	49.13	57.31	63.54
$b_0$	-2.55390016	-2.81798742	-2.96923230	-3.06185527	-3.12141583
$b_1$	1.36982232	1.57378592	1.70096941	1.78304206	1.83763174
$b_2$	-0.09287224	-0.18208568	-0.25604913	-0.31259844	-0.35436474
$b_3$		0.01729347	0.04469233	0.07387528	0.10009236
$b_4$			-0.00499645	-0.01535231	-0.02831548
$b_5$				0.00196105	0.00661843
$b_6$					-0.00095440

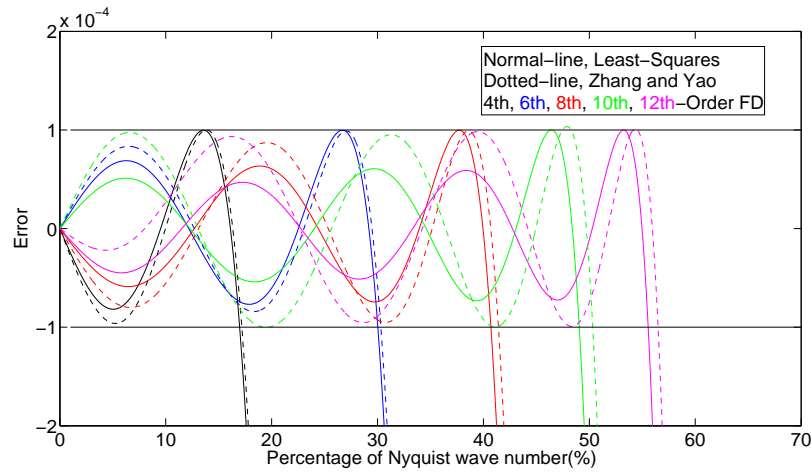


Figure 1: Accuracy comparison between optimized FD operator for the 1st derivative by Least-squares and by Zhang and Yao (2013a)

Table 3: Properties of simulated 2D wave

<b>Dimension</b>	512x512	<b>Grid spacing</b>	5m
<b>Time step</b>	5e-04	<b>Velocity</b>	1500 m/s
<b>Ricker wavelet</b>	40 Hz peak	<b>Snapshots</b>	1.5 s

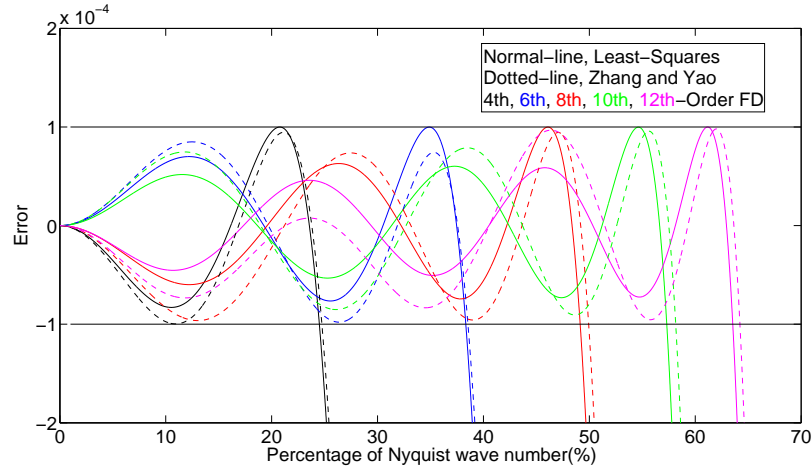


Figure 2: Accuracy comparison between optimized FD coefficients for the 2nd derivative by least-squares and by Zhang and Yao (2013a)

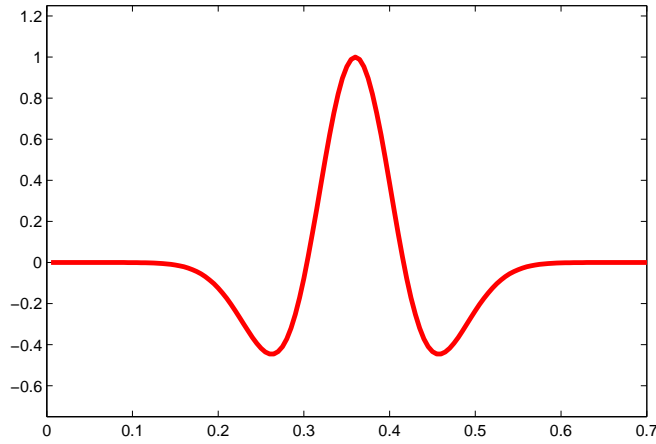


Figure 3: Ricker wavelet

Table 4: Finite-difference coefficients for 1st derivative (Dispersion based).

	4th-Order	6th-Order	8th-Order	10th-Order	12th-Order
$k_c$	17.14	29.21	39.54	47.83	54.42
$k$ coverage	15.66	28.03	38.57	47.01	53.71
$b_1$	0.67500890	0.77070762	0.83217633	0.87369847	0.90255480
$b_2$	-0.08756464	-0.16729465	-0.24273904	-0.28794981	-0.32961431
$b_3$		0.02130997	0.05452901	0.09161233	0.12705023
$b_4$			-0.00678679	-0.02153328	-0.04161276
$b_5$				0.00270335	0.00993314
$b_6$					-0.00128438

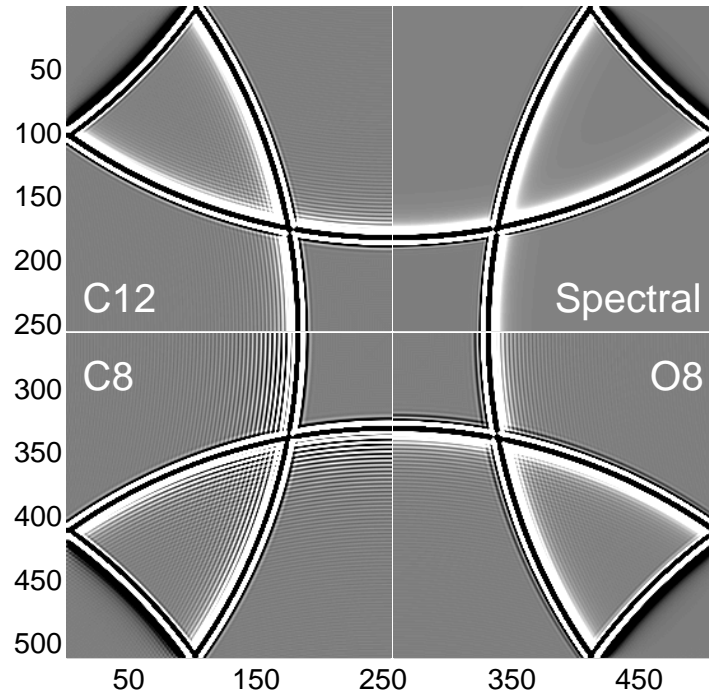


Figure 4: 2D wave propagation comparison between C12 : conventional FD 12th-order, Spectral method, C8 : conventional FD 8th-order, and O8 : optimized FD 8th-order

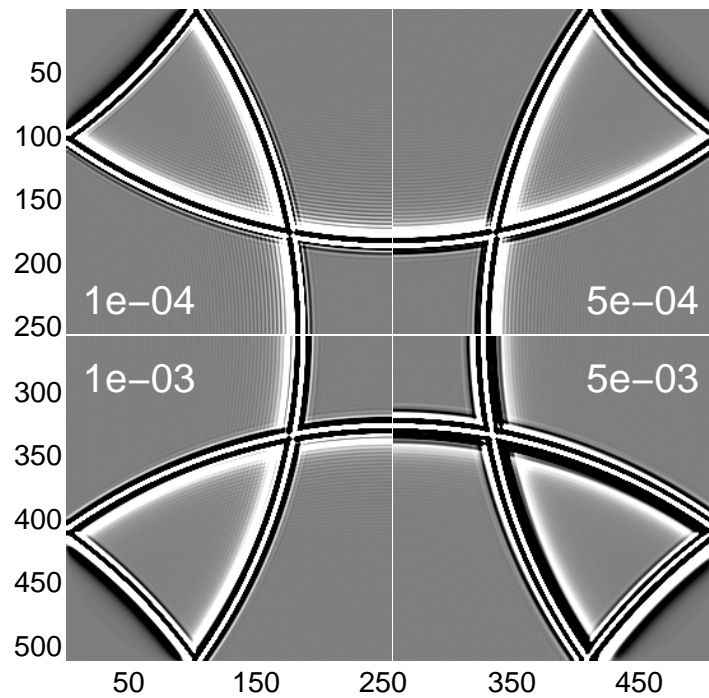


Figure 5: 2D wave propagation comparison between 8th-order optimized FD with error-threshold 1e-04, 5e-04, 1e-03, and 5e-03.

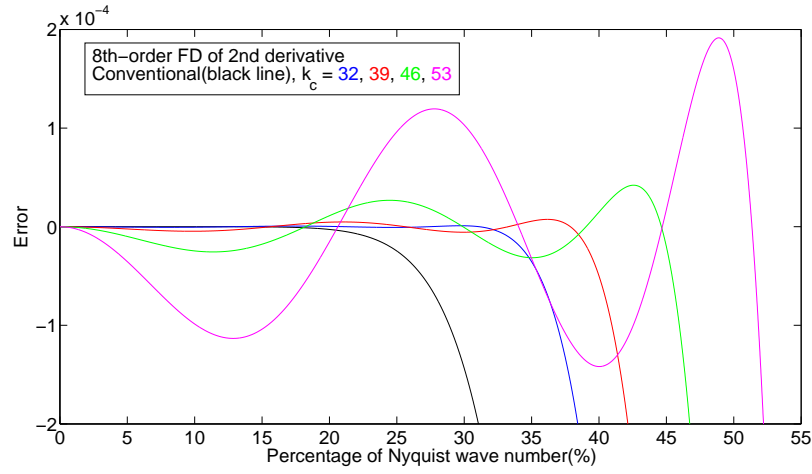


Figure 6: Accuracy of 8th-order FD of 2nd derivative optimized by least-squares using  $k_c = 32, 39, 46,$  and  $53,$  and the conventional FD

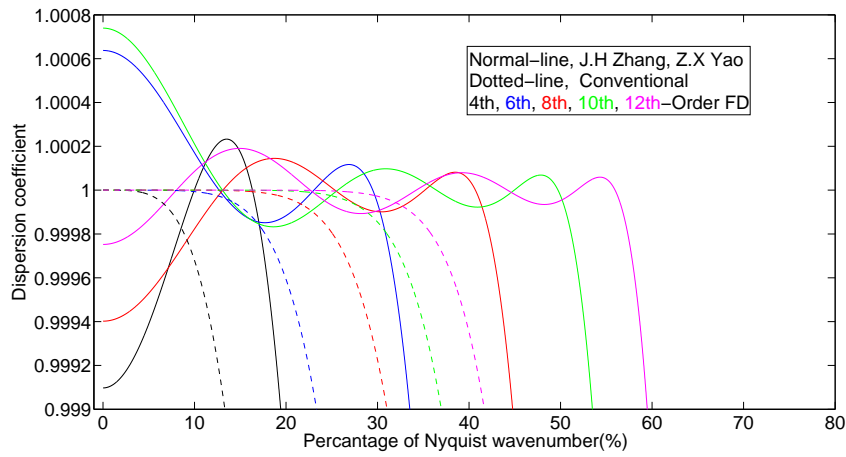


Figure 7: The plot between dispersion coefficient and percentage of Nyquist wave number of 1st derivative, Zhang and Yao (2013a) and conventional FD.

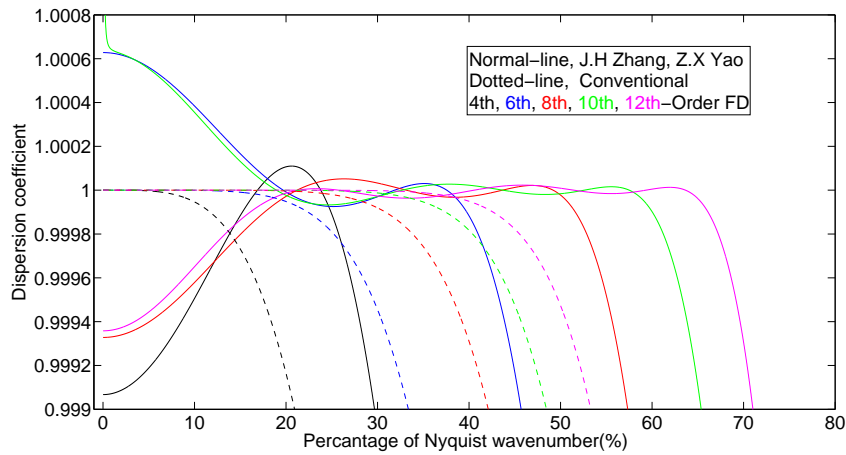


Figure 8: The plot between dispersion coefficient and percentage of Nyquist wave number of 2nd derivative, Zhang and Yao (2013a) and conventional FD.

Table 5: Finite-difference coefficients for 2nd derivative (Dispersion based).

	4th-Order	6th-Order	8th-Order	10th-Order	12th-Order
$k_c$	24.24	36.00	46.13	54.28	60.73
$k$ coverage	21.88	34.41	44.91	53.29	59.9
$b_0$	-2.53337462	-2.78496423	-2.93447476	-3.03074442	-3.09537133
$b_1$	1.35568966	1.54775149	1.67136772	1.75528930	1.81367860
$b_2$	-0.08900235	-0.16995123	-0.23816462	-0.29307839	-0.33584722
$b_3$		0.01468186	0.03761362	0.06344350	0.08826335
$b_4$			-0.00357934	-0.01145663	-0.02231877
$b_5$				0.00117443	0.00439305
$b_6$					-0.00048335

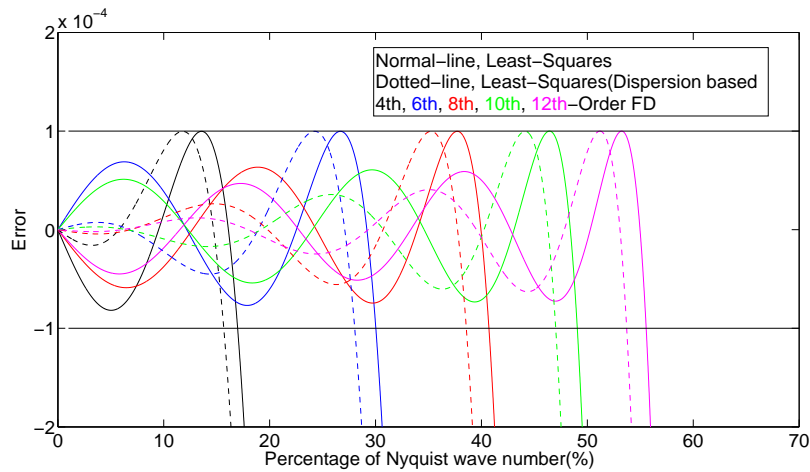


Figure 9: Accuracy comparison between optimized FD operator for the 1st derivative by original least-squares and by dispersion based

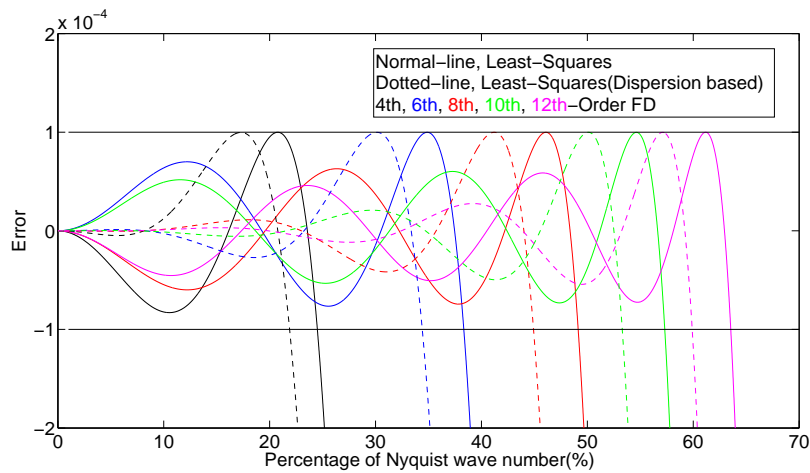


Figure 10: Accuracy comparison between optimized FD operator for the 2nd derivative by original least-squares and by dispersion based

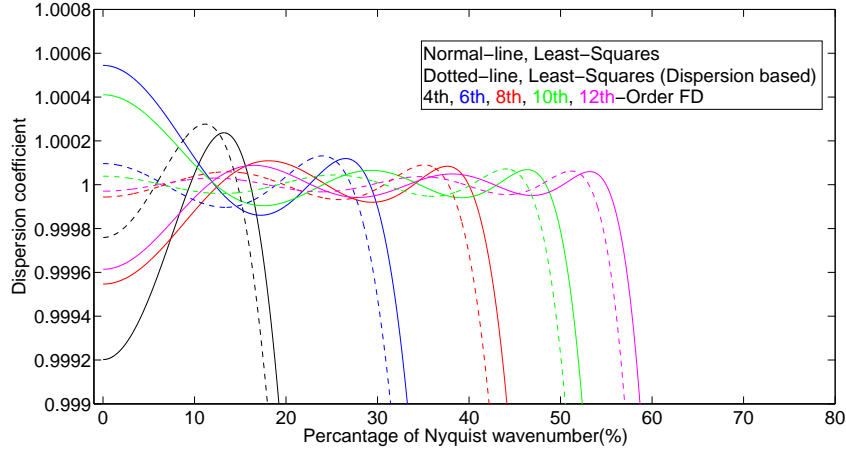


Figure 11: The plot between dispersion coefficient and percentage of Nyquist wave number of 1st derivative of least-squares and dispersion based.

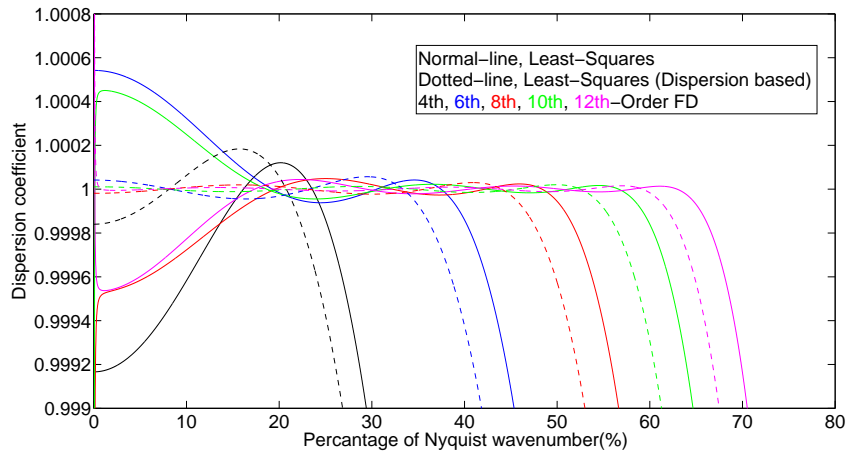


Figure 12: The plot between dispersion coefficient and percentage of Nyquist wave number of 2nd derivative of least-squares and dispersion based.

Table 6: Grid points per wavelength comparison

Method	Grid points per wavelength				
	4th-Order	6th-Order	8th-Order	10th-Order	12th-Order
<b>Conventional</b>					
1st-derivative	20.04	11.47	8.40	6.88	5.97
2nd-derivative	13.74	8.92	6.92	5.85	5.19
<b>Original least-squares</b>					
1st-derivative	11.79	6.66	4.91	4.08	3.60
2nd-derivative	8.16	5.21	4.07	3.49	3.15
<b>Dispersion based</b>					
1st-derivative	12.77	7.14	5.19	4.25	3.72
2nd-derivative	9.14	5.81	4.45	3.75	3.34

Table 7: Grid points per wavelength comparing with conventional FD  
 Grid points per wavelength (%)

Method	4th-Order	6th-Order	8th-Order	10th-Order	12th-Order
<b>Conventional</b>					
1st-derivative	100.00	100.00	100.00	100.00	100.00
2nd-derivative	100.00	100.00	100.00	100.00	100.00
<b>Original least-squares</b>					
1st-derivative	58.83	58.06	58.45	59.30	60.30
2nd-derivative	59.39	58.41	58.82	59.66	60.69
<b>Dispersion based</b>					
1st-derivative	63.72	62.25	61.79	61.77	62.31
2nd-derivative	66.52	65.13	64.31	64.10	64.35

## APPENDIX

## A. Finite difference method in the wavenumber domain

1. The definition of Fourier transforms used in this work is given as

$$F(k_x) = \int_{-\infty}^{\infty} f(x) e^{-ik_x x} dx, \quad (23)$$

$$f(x) = \frac{1}{2\pi} \int_{-\infty}^{\infty} F(k_x) e^{ik_x x} dk_x. \quad (24)$$

Differentiating both sides of equation 24 with respect to  $x$ , yields

$$\frac{df(x)}{dx} = \frac{1}{2\pi} \int_{-\infty}^{\infty} ik_x F(k_x) e^{ik_x x} dk_x, \quad (25)$$

$$\frac{d^2 f(x)}{dx^2} = \frac{1}{2\pi} \int_{-\infty}^{\infty} i^2 k_x^2 F(k_x) e^{ik_x x} dk_x. \quad (26)$$

Examining equations 23-26, we can conclude that

$$\frac{\partial^m f(x)}{\partial x^m} \Rightarrow (ik_x)^m F(k_x). \quad (27)$$

2. Fourier transform of  $\partial f(x)/\partial x = \frac{1}{\Delta x} \sum_{n=-N/2}^{N/2} b_n f_n$ ,

Substituting equation 24 into  $\partial f(x)/\partial x = \frac{1}{\Delta x} \sum_{n=-N/2}^{N/2} b_n f_n$ , we get

$$\begin{aligned} \frac{1}{2\pi} \int_{-\infty}^{\infty} ik_x F(k_x) e^{ik_x x} dk_x &= \frac{1}{\Delta x} \frac{1}{2\pi} \left[ \sum_{n=-N/2}^{N/2} b_n \int_{-\infty}^{\infty} F(k_x) e^{ik_x(x+n\Delta x)} dk_x \right], \\ &= \frac{1}{\Delta x} \frac{1}{2\pi} \left[ b_0 \int_{-\infty}^{\infty} F(k_x) e^{ik_x x} dk_x + \sum_{n=1}^{N/2} b_n \int_{-\infty}^{\infty} F(k_x) (e^{ik_x(x+n\Delta x)} - e^{ik_x(x-n\Delta x)}) dk_x \right], \quad b_n = -b_{-n}, \\ &= \frac{1}{\Delta x} \frac{1}{2\pi} \left[ b_0 \int_{-\infty}^{\infty} F(k_x) e^{ik_x x} dk_x + \sum_{n=1}^{N/2} b_n \int_{-\infty}^{\infty} F(k_x) e^{ik_x x} (2i \sin(k_x n \Delta x)) dk_x \right], \\ 0 &= \int_{-\infty}^{\infty} F(k_x) e^{ik_x x} \left( ik_x - \frac{1}{\Delta x} \left[ b_0 + 2i \sum_{n=1}^{N/2} b_n \sin(k_x n \Delta x) \right] \right) dk_x. \end{aligned}$$

Since  $b_0 = 0$  for odd derivative, thus,

$$ik_x = \frac{i}{\Delta x} \sum_{n=-N/2}^{N/2} b_n \sin(k_x n \Delta x). \quad (28)$$

3. Fourier transform of  $\partial^2 f(x)/\partial x^2 = \frac{1}{(\Delta x)^2} \sum_{n=-N/2}^{N/2} b_n f_n$ ,

Substituting equation 24 into  $\partial^2 f(x)/\partial x^2 = \frac{1}{(\Delta x)^2} \sum_{n=-N/2}^{N/2} b_n f_n$ , we get

$$-\frac{1}{2\pi} \int_{-\infty}^{\infty} k_x^2 F(k_x) e^{ik_x x} dk_x \Big|_{x=0} = \frac{1}{(\Delta x)^2} \frac{1}{2\pi} \left[ \sum_{n=-N/2}^{N/2} b_n \int_{-\infty}^{\infty} F(k_x) e^{ik_x(x+n\Delta x)} dk_x \right],$$

$$\begin{aligned}
&= \frac{1}{(\Delta x)^2} \frac{1}{2\pi} \left[ b_0 \int_{-\infty}^{\infty} F(k_x) e^{ik_x x} dk_x + \sum_{n=1}^{N/2} b_n \int_{-\infty}^{\infty} F(k_x) (e^{ik_x(x+n\Delta x)} + e^{ik_x(x-n\Delta x)}) dk_x \right], \quad b_n = b_{-n}, \\
&= \frac{1}{(\Delta x)^2} \frac{1}{2\pi} \left[ b_0 \int_{-\infty}^{\infty} F(k_x) e^{ik_x x} dk_x + \sum_{n=1}^{N/2} b_n \int_{-\infty}^{\infty} F(k_x) e^{ik_x x} (2 \cos(k_x n \Delta x)) dk_x \right], \\
0 &= \int_{-\infty}^{\infty} F(k_x) e^{ik_x x} \left( k_x^2 + \frac{1}{(\Delta x)^2} \left[ b_0 + 2 \sum_{n=1}^{N/2} b_n \cos(k_x n \Delta x) \right] \right) dk_x.
\end{aligned}$$

Thus,

$$-k_x^2 = \frac{1}{(\Delta x)^2} \sum_{n=-N/2}^{N/2} b_n \cos(k_x n \Delta x). \quad (29)$$

## B. The prove of dispersion coefficients

From 1D frequency-domain scalar wave equation, and one-way frequency-domain scalar wave equation

$$\frac{\partial^2 P}{\partial x^2} = -\frac{\omega^2}{v^2} P, \quad \text{two-way wave equation,} \quad (30)$$

$$\frac{\partial P}{\partial x} = i\frac{\omega}{v} P, \quad \text{one-way wave equation,} \quad (31)$$

apply FD to these equation, which gives

$$\frac{\sum_{n=-N/2}^{N/2} b_n P_n}{(\Delta x)^2}, = -\frac{\omega^2}{v^2} P(x) \quad \text{two-way wave equation,} \quad (32)$$

$$\frac{\sum_{n=-N/2}^{N/2} b_n P_n}{\Delta x}, = i\frac{\omega}{v} P(x) \quad \text{one-way wave equation.} \quad (33)$$

Note that,  $P_n = P(x+n\Delta x)$ . To obtain a dispersion coefficient, we use a plane wave solution  $P(x+n\Delta x) = A \exp(i(x+n\Delta x)k)$ , where  $A$  is amplitude. Substitute the plane wave solution to the equations above, which give (Note that: for 2nd derivative  $b_n = b_{-n}$ , and for 1st derivative  $b_n = -b_{-n}$ )

$$\frac{\omega}{v} = \left( -\frac{b_0 + 2 \sum_{n=1}^{N/2} b_n \cos(nk_x \Delta x)}{(\Delta x)^2} \right)^{1/2}, \quad \text{two-way wave equation,} \quad (34)$$

$$\frac{\omega}{v} = \frac{2 \sum_{n=1}^{N/2} b_n \sin(nk_x \Delta x)}{\Delta x}, \quad \text{one-way wave equation,} \quad (35)$$

divide both side of equation by  $k_x$ , using  $k = k_x \Delta x$ , and  $v_{ph} = \omega/k_x$ , we get

$$\frac{v_{ph}}{v} = \frac{\omega/k_x}{v} = \left( -\frac{b_0 + 2 \sum_{n=1}^{N/2} b_n \cos(nk)}{k^2} \right)^{1/2}, \quad \text{two-way wave equation,} \quad (36)$$

$$\frac{v_{ph}}{v} = \frac{\omega/k_x}{v} = \frac{2 \sum_{n=1}^{N/2} b_n \sin(nk)}{k}, \quad \text{one-way wave equation.} \quad (37)$$

For more information about dispersion coefficient, please visit Cohen (2002).

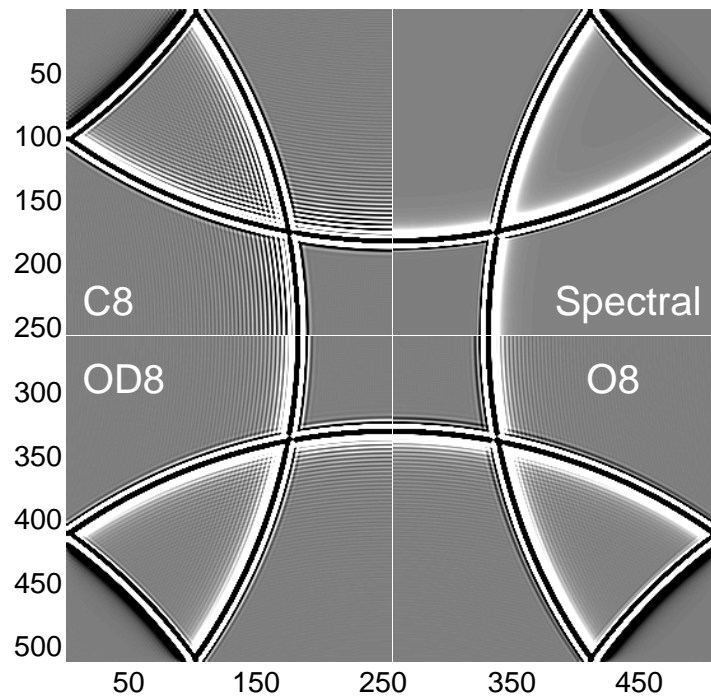


Figure 13: 2D wave propagation comparison between C8 : conventional FD 8th-order, Spectral method, OD8 : optimized FD with dispersion coefficients based 8th-order, and O8 original optimized FD 8th-order

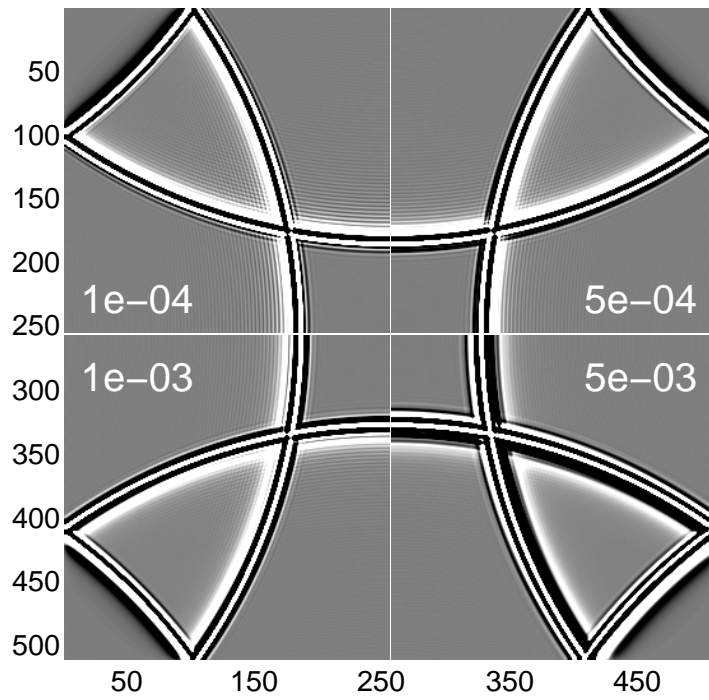


Figure 14: 2D wave propagation comparison between 8th-order optimized FD (original) with error-threshold 1e-04, 5e-04, 1e-03, and 5e-03

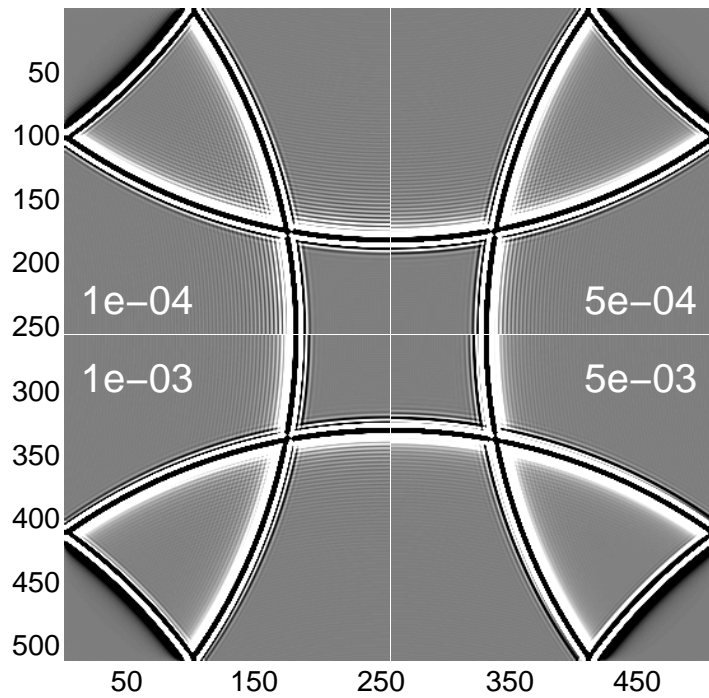


Figure 15: 2D wave propagation comparison between 8th-order optimized FD (dispersion based) with error-threshold 1e-04, 5e-04, 1e-03, and 5e-03

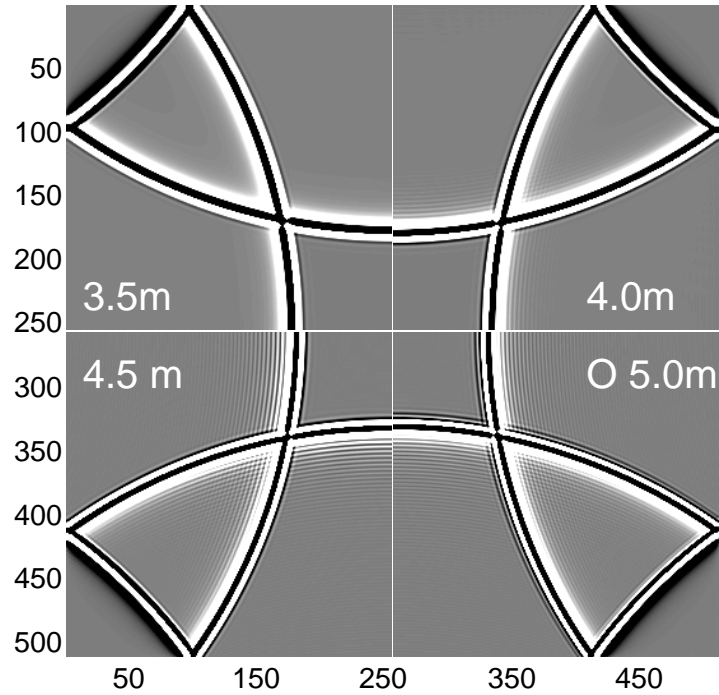


Figure 16: 2D wave propagation comparison between conventional FD 8th-order with grid spacing 3.5, 4, and 4.5m and original optimized FD 8th-order with grid spacing 5m

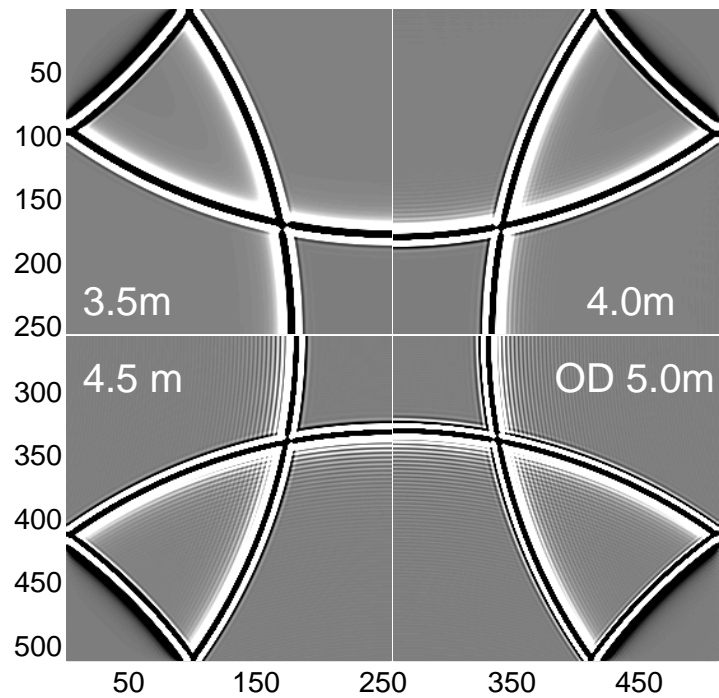


Figure 17: 2D wave propagation comparison between conventional FD 8th-order with grid spacing 3.5, 4, and 4.5m and dispersion based optimized FD 8th-order with grid spacing 5m



# Simulation of Solitary Wave at An Artificial Coastline using FUNWAVE

Pawin Sitsungnoen and Chaiwoot Boonyasiriwat

## ABSTRACT

FUNWAVE program is developed by James T. Kirby and his colleagues in Delaware University. This program widely use in oceanic waves and waves near coastline problems. This is based on the fully-nonlinear Boussinesq equations that are explained gravity surface wave motion by the conserved surface elevation and their horizontal velocities. FUNWAVE is continuously developed by Shi and Kirby (2012) with Total Variation Diminishing (TVD) method. Moreover, he guides process to use this program by five examples. Now this work use some examples to simulate the one-dimensional and two-dimensional solitary wave at an artificial coastline on computational domain. A numerical experiment setting is used for numerical parameters testing. The computational time consuming and height of breaking wave are measured by a various numerical grid spacings and a various initialized solitary waves. For one-dimensional solitary wave, we found that a decreasing numerical spacing grid causes an increasing computational time consuming and height of breaking wave when the wave arrives near coastline. Furthermore, we found that a decreasing of initialized amplitude causes a decreasing of computational time consuming in two-dimensional solitary wave simulation. However, we has some problem about the computational time consuming when we simulate a two-dimensional domain. This problem relieves by MPI parallel programming on server computer.

## INTRODUCTION

FUNWAVE is program that developed by James T. Kirby and his colleagues at the Center for Applied Coastal Research, Department of Civil and Environmental Engineering, University of Delaware. This program greatly performs some oceanic and coastal waves simulation. Tsunamis

simulation is one of applications to use this program because of better accuracy. Moreover, tsunamis application gives a development of tsunamis warning system to understand mechanism and increase warning time. However, we do not apply on tsunami simulation because we would like to study and numerical practice for the basic of this program in solitary wave.

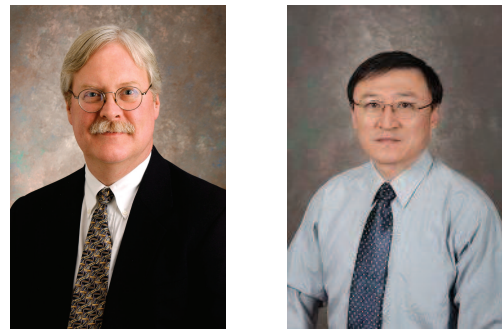


Figure 1: James T. Kirby (left) and Fengyan Shi (right) who develop FUNWAVE program.

Furthermore, FUNWAVE based on the fully-nonlinear Boussinesq equations. These equations are further developed from the shallow water equations with including dispersive property. The detail of these equations are presented and explained in Boussinesq equations section.

(Shi and Kirby, 2012) afterward develops FUNWAVE by using the Total Variation Diminishing (TVD) method. He guides process to use this program by five examples: 1. Breaking waves on a beach, 2. Random wave shoaling and breaking on a slope, 3. Wave propagation over a shoal, 4. Solitary wave on a conical island, and 5. Solitary wave runup on a shelf with an island.

This work verifies three of five examples that are the breaking waves on a beach, the random wave shoaling and breaking on a slope and the the solitary wave runup on a shelf with an island examples. Then we use these examples to design numerical experiments for a simulation

of one-dimensional and two-dimensional solitary wave at an artificial coastline. We test the effect of numerical grid spacings to computational time consuming and height of breaking wave in one-dimensional simulation. In addition, we test the effect of various initialized solitary wave to computational time consuming. The computational setting and numerical results for each type of simulation are presented in the simulation of one-dimensional and two-dimensional solitary wave at an artificial coastline.

### FULLY-NONLINEAR BOUSSINESQ EQUATIONS

For two-dimensional oceanic and coastal waves, we can describe wave motion by fully-nonlinear Boussinesq equations. These equations are based on the two basic of conservation law. The first is conservation of mass that explains the surface elevation variable ( $\eta$ ),

$$\frac{\partial \eta}{\partial t} + \nabla \cdot \vec{M} = 0, \quad (1)$$

where  $\vec{M}$  is mass flux.

The second is conservation of momentum that explains horizontal velocity variables ( $\vec{u}_\alpha$ ),

$$\frac{\partial \vec{u}_\alpha}{\partial t} + (\vec{u}_\alpha \cdot \nabla) \vec{u}_\alpha + g \nabla \eta + \vec{V}_1 + \vec{V}_2 + \vec{V}_3 + \vec{R} = 0, \quad (2)$$

where  $\vec{V}_1$  and  $\vec{V}_2$  are the dispersive Boussinesq terms,  $\vec{V}_3$  is the expression of the cross product between vorticity and particle velocity vectors ( $\vec{\omega} \times \vec{u}$ ), and  $\vec{R}$  is the diffusive and dissipative term.

To simulate some coastal waves, the fully-nonlinear Boussinesq equations must be solved by using the Total Variation Diminishing (TVD) method. Because this method is widely applied in shock wave or breaking wave effect near coastlines. This effect occurs when the field variables (such as a velocities field) has some discontinuous solution. In addition, this method decreases the misleading oscillation of shock wave. However, TVD method requires the governing equations. So the fully-nonlinear Boussinesq equations are modified into the generalized conservative form as

$$\frac{\partial \vec{\Psi}}{\partial t} + \nabla \cdot \vec{\Theta}(\Psi) = \vec{S}, \quad (3)$$

where  $\vec{\Psi}$  and  $\vec{\Theta}(\Psi)$  are the conserved variables vector and the flux vector function, respectively, and are given by

$$\vec{\Psi} = \begin{pmatrix} \eta \\ \vec{U} \\ \vec{V} \end{pmatrix}, \quad \vec{\Theta} = \begin{pmatrix} P\hat{x} + Q\hat{y} \\ \left[ \frac{P^2}{H} + \frac{1}{2}g(\eta^2 + 2\eta h) \right] \hat{x} + \frac{PQ}{H} \hat{y} \\ \frac{PQ}{H} \hat{x} + \left[ \frac{P^2}{H} + \frac{1}{2}g(\eta^2 + 2\eta h) \right] \hat{y} \end{pmatrix},$$

$$\text{and} \quad \vec{S} = \begin{pmatrix} 0 \\ g\eta \frac{\partial h}{\partial x} + \psi_x + HR_x \\ g\eta \frac{\partial h}{\partial y} + \psi_y + HR_y \end{pmatrix}.$$

To reduce difficulty, equation (3) is transformed into a Riemann solvers. nevertheless, the detail about method-

ology of TVD method are not explained in this work. So we skip to present a simulation of solitary wave in one-dimensional and two-dimensional problems.

### THE SIMULATION OF ONE-DIMENSIONAL SOLITARY WAVE AT AN ARTIFICIAL COASTLINE

This section are presented numerical experiment and numerical results of the one-dimensional solitary wave simulation. The details of problematic setting and the numerical results are clearly explained in the next paragraph.

### Numerical Experiment

The following paragraph introduces concept of simulated problems, and then explained the strategy of numerical experiment.

First of all, we verify three selected examples from (Shi and Kirby, 2012). There are the breaking waves on a beach, the random wave shoaling and breaking on a slope and the solitary wave runup on a shelf with an island examples.

Then the first two examples are modified to simulate the solitary wave near a slope that is represented an artificial coastline. This simulated problem is called the simulation of one-dimensional solitary wave at a coastline.

Now, we would like to study the effect of numerical grid spacings ( $dx$ ) to the height of breaking wave and computational time consuming.

The hypothesis of this experiment is that the decrease of  $dx$  will contribute the increase of the height of breaking wave and computational time consuming. A problematic setting for verifying this hypothesis is illustrated in the next paragraph.

#### The problematic Setting

It can be illustrated by Figure 2.

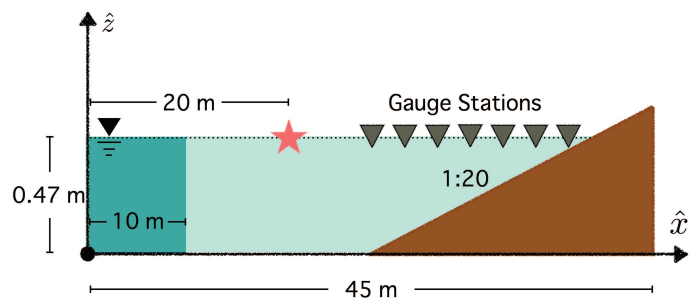


Figure 2: The illustration of computational domain.

For spatial setting, a horizontal distance is fixed 45 m. The water depth is limited in 0.47 m. The regular spacing grid is 0.20 m. For temporal setting, total computational time is 40 sec with numerical time step size 0.08325 sec. So

this experiment has 480 time steps to simulate the solitary wave propagation. Numerical result is shown by some of snapshots.

Then we install 12 gauge stations at depth  $h = 47, 35, 30, 25, 20, 17.5, 15, 12.5, 10, 7.5, 5,$  and  $2.5$  cm in Figure 2. The surface elevation is measured as a time series in numerical results section.

Finally, we vary  $dx$  as  $0.20, 0.10, 0.08, 0.06, 0.04,$  and  $0.02$  m. Both computational time consuming and the height of breaking wave are measured and are presented in Table 1. In addition, the snapshots of breaking wave at any  $dx$  are shown too in numerical result section.

### Initialization

In input file, the initial conditions can be adjusted in FUNWAVE program. We use only solitary wave by setting `WAVEMAKER = INL_SOL` at line 89. From Figure 2, a position of source located 20 m far from the left edge by setting `XWAVEMAKER = 20.0` at line 98. The shape of initialized solitary wave can be shown as Figure 3.

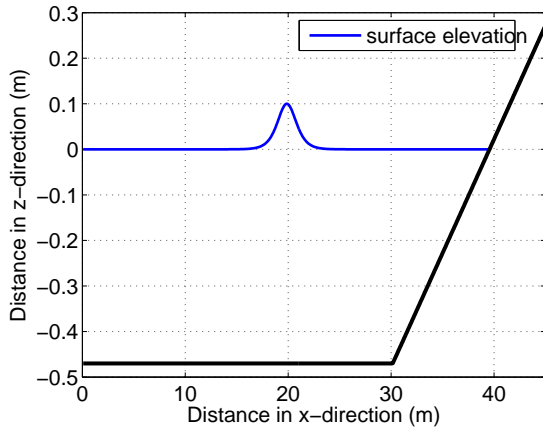


Figure 3: The illustration of computational domain.

Furthermore, there has any parameters to flexibly adjust. The amplitude of solitary wave can be changed by setting `AMP = 0.1` at line 95. Because the water depth is  $0.47$  m, so we have to set `DEP = 0.47` at line 96.

### Boundaries Conditional Setting

This problem has two boundaries that are the left and the right edges of computational domain. For the left edge, there is an absorbing boundary condition. We can adjust the absorbing layer that equal to  $10$  m in Figure 2. In input file, the absorbing layer is changed by setting `Sponge_west_width = 10.0` at line 135. For the right edge, it is a Dirichlet boundary condition by setting the conserved variables to zero.

In addition, we use the runup condition at a slope. This condition can solve runup effect of solitary wave when they arrive to a slope that is represented as an artificial

coastline. We can clearly see this effect in the simulation of two-dimensional solitary wave at a coastline.

## The Execution

To run some works in FUNWAVE program, the source code should be compiled by using command “make” in terminal window. Then we receive `mytvd` file, and copy this file to any example folders.

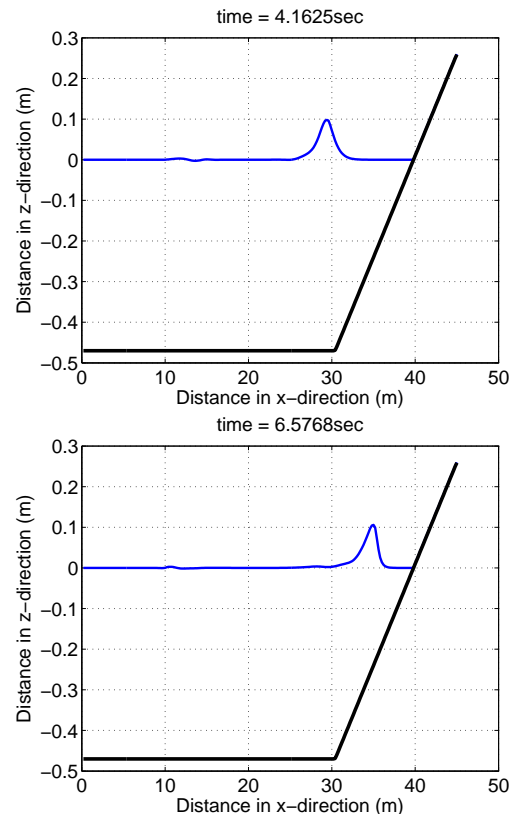
For this problem, we copy `mytvd` file into `example_1` folder. Then we set some parameters in `input` file. Back to terminal window, we already to run work and measured computational time consuming by using command “time `./mytvd`”.

## Numerical Results

This part presents numerical results from the simulation of one-dimensional solitary wave. There have numerical snapshots at some time step, numerical snapshot near coastline for some numerical grid spacings, table of numerical experiment results, time series of surface elevation for some gauge stations and the comparison of time series of surface elevation for some selected gauge stations.

### Numerical snapshots at some time step

Remember that the regular numerical grid spacing is  $0.20$  m. So some of numerical snapshots are presented when time =  $4.1625, 6.5768, 7.5758$  and  $16.6500$  sec.



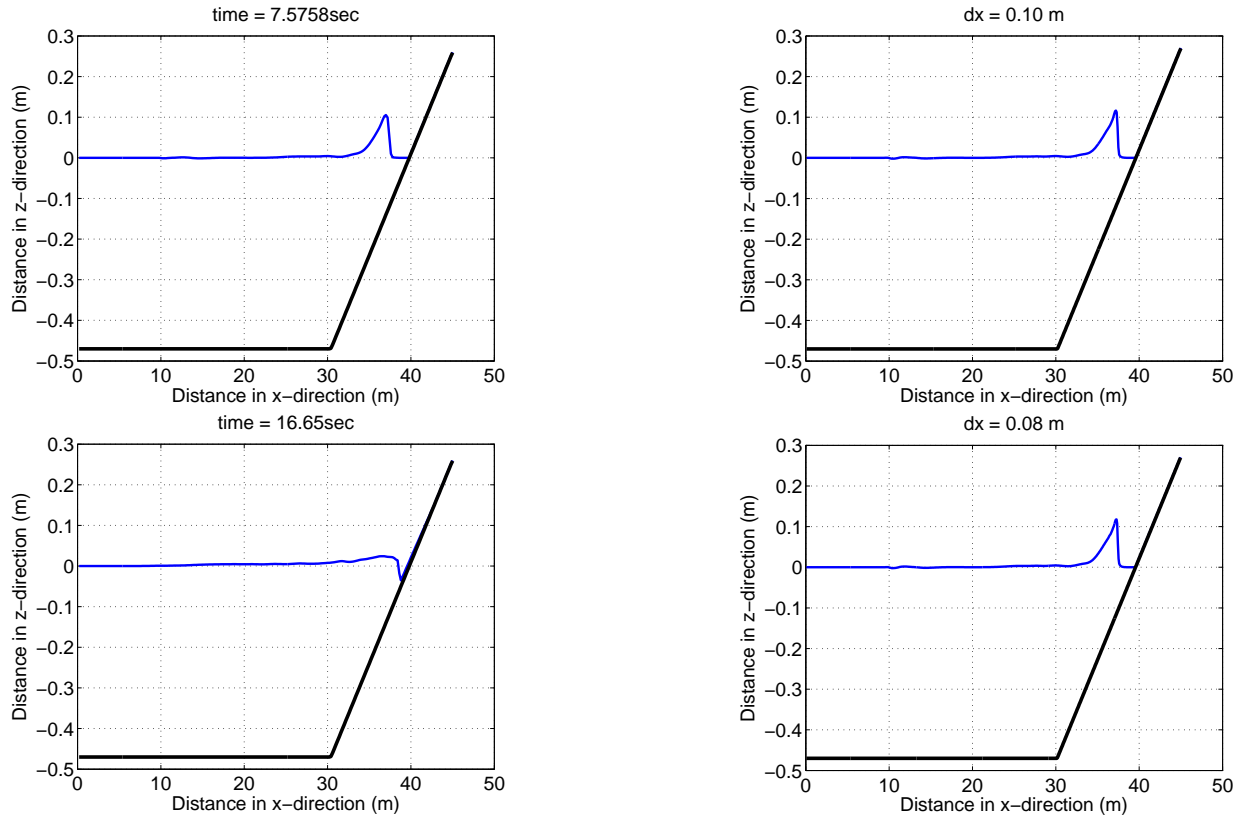
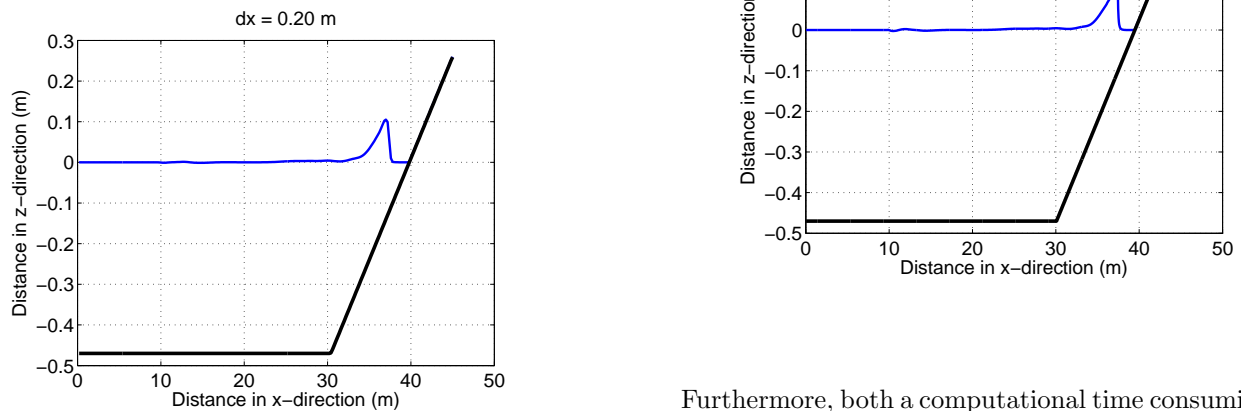


Figure 4: Numerical snapshots for  $dx = 0.20$  when time = 4.1625, 6.5768, 7.5758 and 16.6500 sec.

From Figure 4, we can exactly see the shock or breaking wave effect of solitary wave at near coastline. This means that the fully-nonlinear Boussinesq equations not only explained dispersive effect but also describe breaking wave effect.

*Numerical snapshots for some numerical grid spacings*

Now we vary numerical grid spacings to 0.10, 0.08, 0.06, 0.04, 0.02 m. Numerical snapshots of this wave near an artificial coastline can be presented by Figure 5.



Furthermore, both a computational time consuming and a height of breaking wave are measured and shown by Table 1. From this table, we can clearly conclude that the

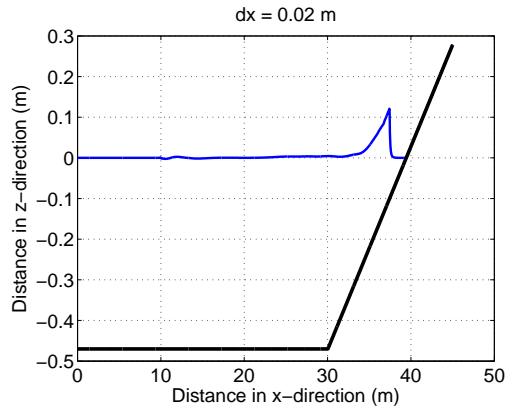


Figure 5: Numerical snapshots near coastline for  $dx = 0.20, 0.10, 0.08, 0.06, 0.04$  and  $0.02$  m.

decreasing numerical spacing grid causes increasing computational time consuming and height of breaking wave.

Table 1: Numerical experiment results

Numerical grid spacing (meters)	Computational time consuming (seconds)	Height of breaking wave (meters)
0.20	13.3696	0.1053
0.10	26.8349	0.1165
0.08	40.5737	0.1178
0.06	68.1620	0.1192
0.04	151.1063	0.1201
0.02	420.0931	0.1209

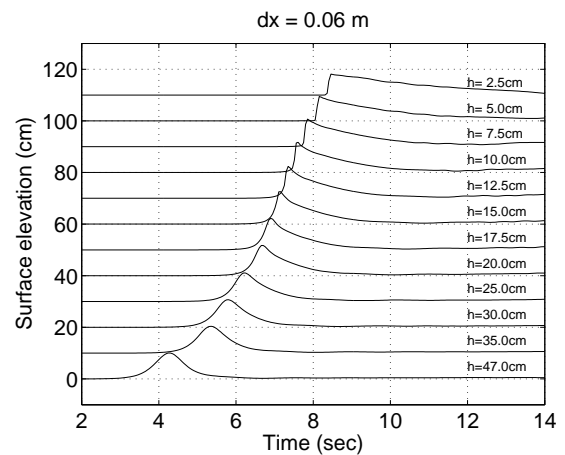
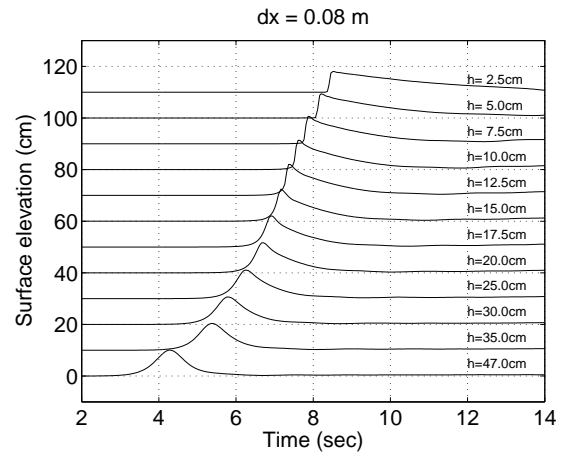
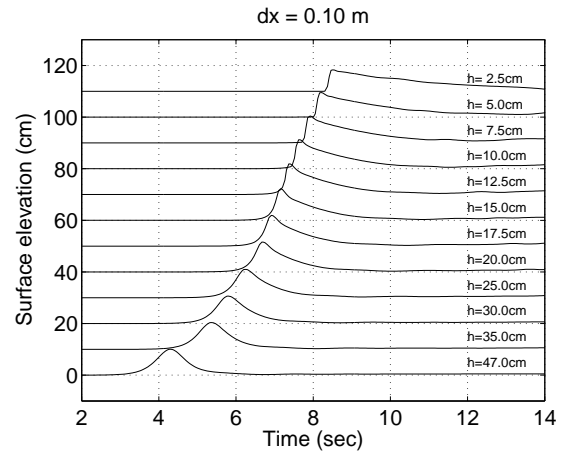
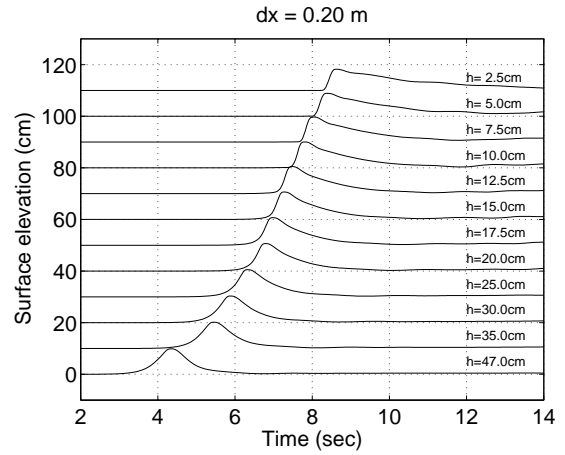
#### *A time series of surface elevation for some gauge stations*

Because we install 12 gauge stations to measured surface elevation along coastline, so this part would like to show time series of surface elevation as Figure 6.

In addition, the time series of surface elevation for some selected gauge stations are presented by Figure 7. When we zoom in each gauge stations, we confirm that the decreasing of numerical spacing grid causes a increasing of height of breaking wave.

### THE SIMULATION OF TWO-DIMENSIONAL SOLITARY WAVE AT AN ARTIFICIAL COASTLINE

The example 5 of Shi and Kirby (2012) is used for testing a computational time consuming due to a numerical parameter of solitary wave. Now this section presents nu-



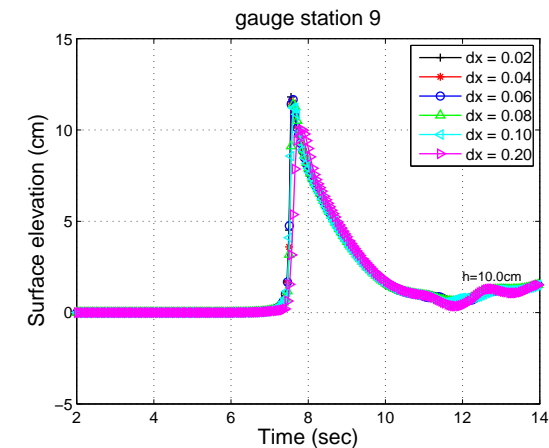
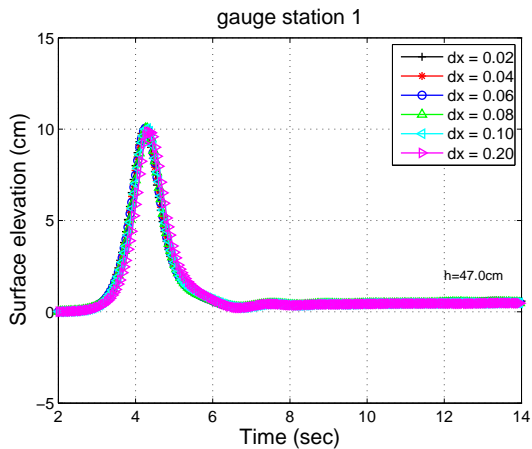
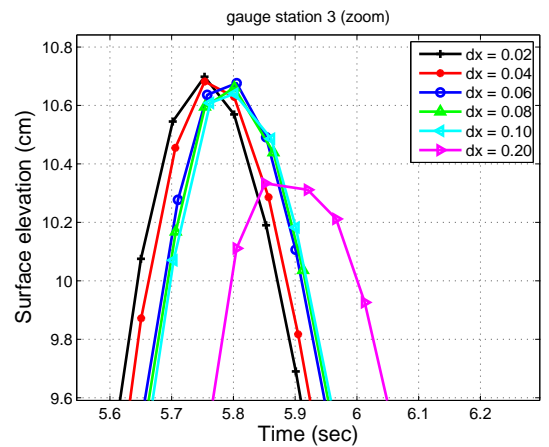
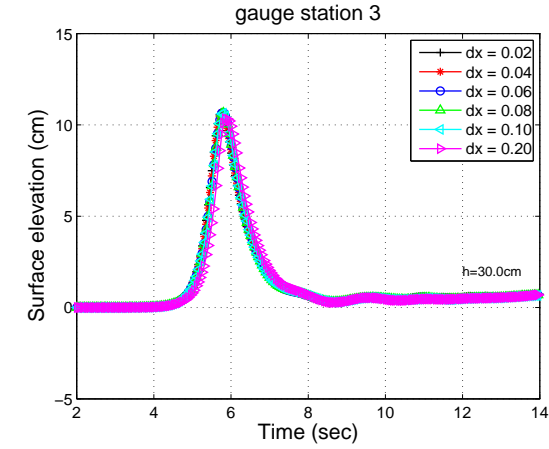
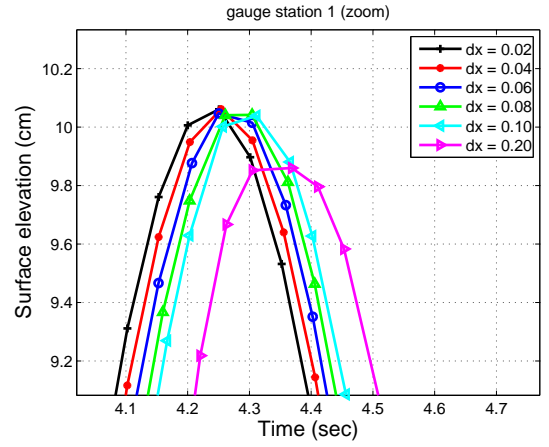
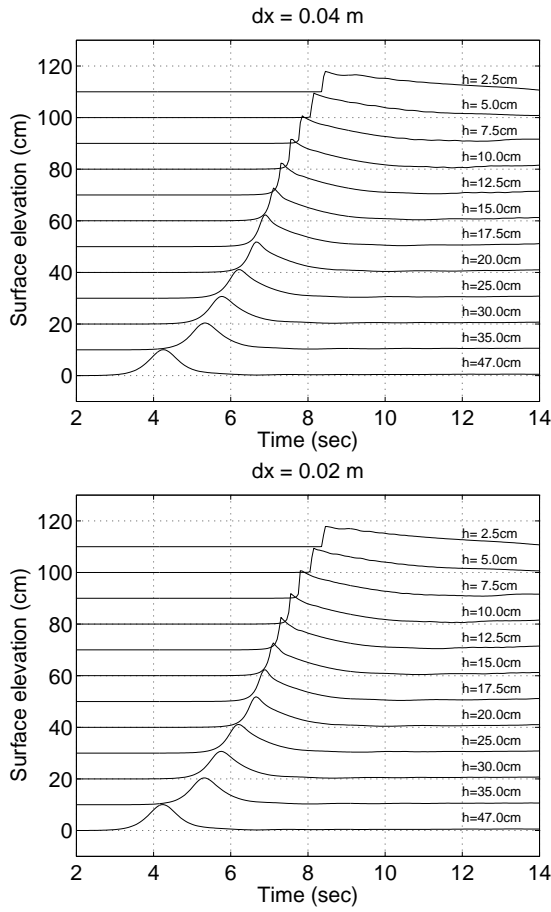


Figure 6: Time series of surface elevation for 12 gauge stations along coastline at depth  $h = 47, 35, 30, 25, 20, 17.5, 15, 12.5, 10, 7.5, 5,$  and  $2.5$  cm when numerical grid spacing =  $0.20, 0.10, 0.08, 0.06, 0.04,$  and  $0.02$  m.

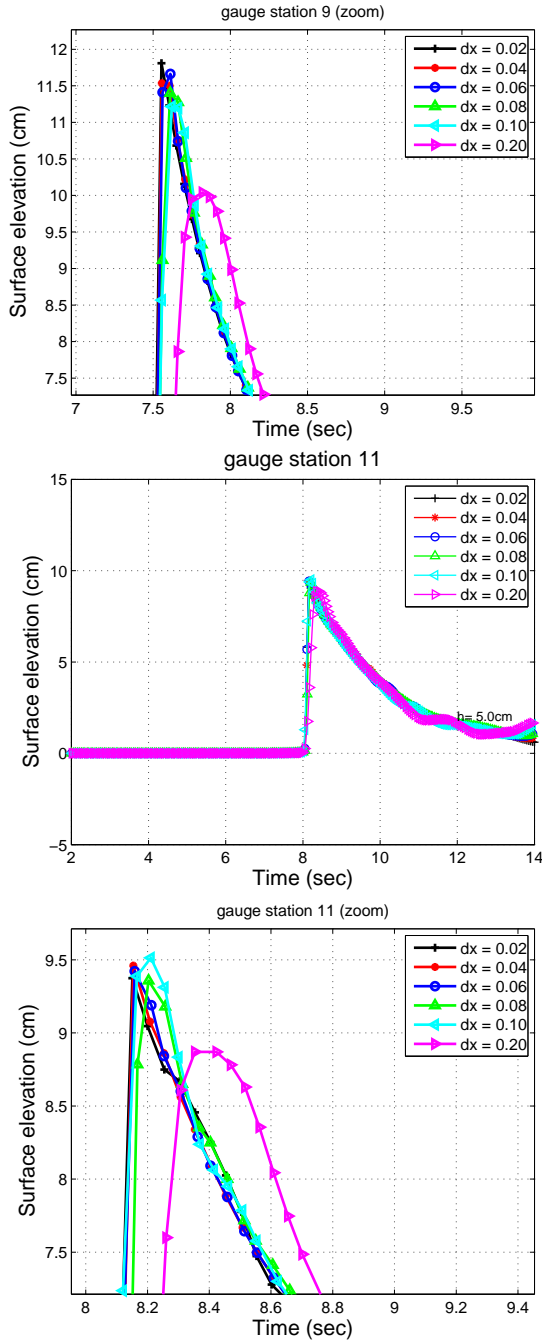


Figure 7: Time series of surface elevation for gauge station number 1, 3, 9, and 11.

numerical setting and numerical results of the simulation of two-dimensional solitary wave at a coastline.

This is not a numerical experiment like in the previous problem. But it is a numerical case study for a two-dimensional inundation of solitary wave. Now we focus on the variation of initialized solitary wave. Moreover, the problematic setting is not same previous problem. They are carefully explained in the next paragraph.

## Numerical Experiment

This paragraph introduces the problematic setting, then this is explained the strategy of numerical testing.

### *The problematic Setting*

A computational domain is reconstructed. The distance in x-direction and y-direction are changed to 48.8 m and 26.5 m, respectively. Then we set the numerical grid spacing in x- and y- directions to 0.1 m. The deepest water depth is changed to in 0.78 m. In addition, the artificial coastline includes a shelf and a inverse cone island as Figure 8.

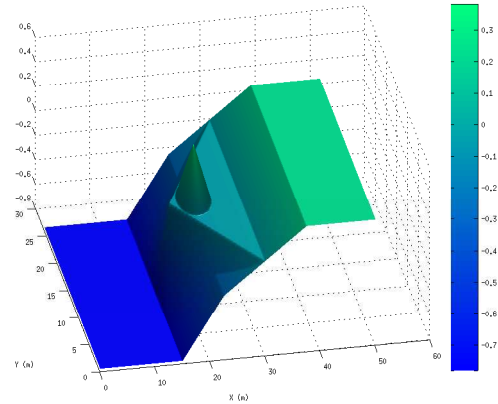


Figure 8: The side view of an artificial coastline.

For temporal setting, total computational time is changed to 45 sec. A numerical time step size is increased to 0.2 sec. So we get 226 time steps to simulate the solitary wave propagation. Numerical results is shown by some snapshots.

### *Initialization*

Now we use a line source of solitary as an initial condition by setting some parameters in input file. Position of source located 10 m far from the left edge in x-direction by setting  $XWAVEMAKER = 10.0$  at line 98. The regular amplitude of solitary source is 0.55 m by setting  $AMP = 0.55$  at line 95. The shape of solitary wave can be presented by Figure 9.

Now we vary the amplitude of initialized solitary wave to 0.32, 0.16, 0.08, 0.04, and 0.02 m. The computational time consuming is measured and shown in Table 2. The numerical snapshots are present in numerical results paragraph.

### *Boundaries Conditional Setting*

This problem has four boundaries. For the left edge, there is an absorbing boundary condition. We can adjust

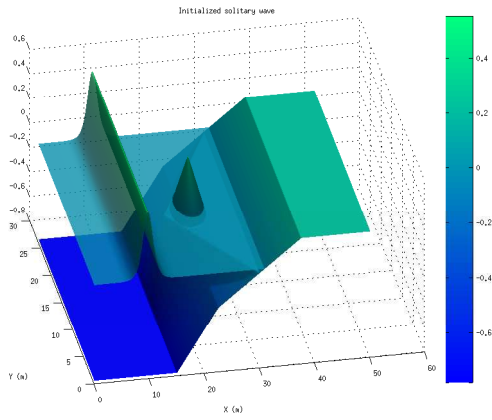


Figure 9: The initialized solitary wave with amplitude 0.55 m.

the absorbing layer that equal to 2 m. In input file, the absorbing layers are changed by setting `Sponge_west_width = 2.0` at line 135. the right edge remain an absorbing condition. We set `Sponge_east_width = 2.0` at line 136 in input file.

The North and South of domain are solid wall boundaries condition. These satisfied

$$\bar{U} = 0, \quad \text{and} \quad \bar{V} = \text{conts.}$$

In addition, this problem is exactly shown the runup effect in numerical results paragraph.

### The Execution

Now we still have `mytvd` file. Next we copy `mytvd` file into `example_5/work` folder. Then we setting some parameters in `input` file. Back to terminal window, we already to run work and measured computational time consuming by using command “time ./mytvd”.

### Numerical Results

This part presents numerical results of the simulation of two-dimensional solitary wave. There have numerical snapshots at some of time step when we vary the initialized amplitude of solitary wave, and table of computational time consuming result.

#### *Numerical snapshots at some of time step*

We remember that the regular initialized amplitude is 0.55 m. This means that Figure 10 is numerical snapshot of simulation at time is 2, 5, 11 and 21 sec.

Now these are numerical snapshots when we decrease the initialized amplitude to 0.32, 0.16, 0.08, 0.04, and 0.02 m.

We can notice that a decreasing of initialized amplitude effects a decreasing of wave runup. So this program

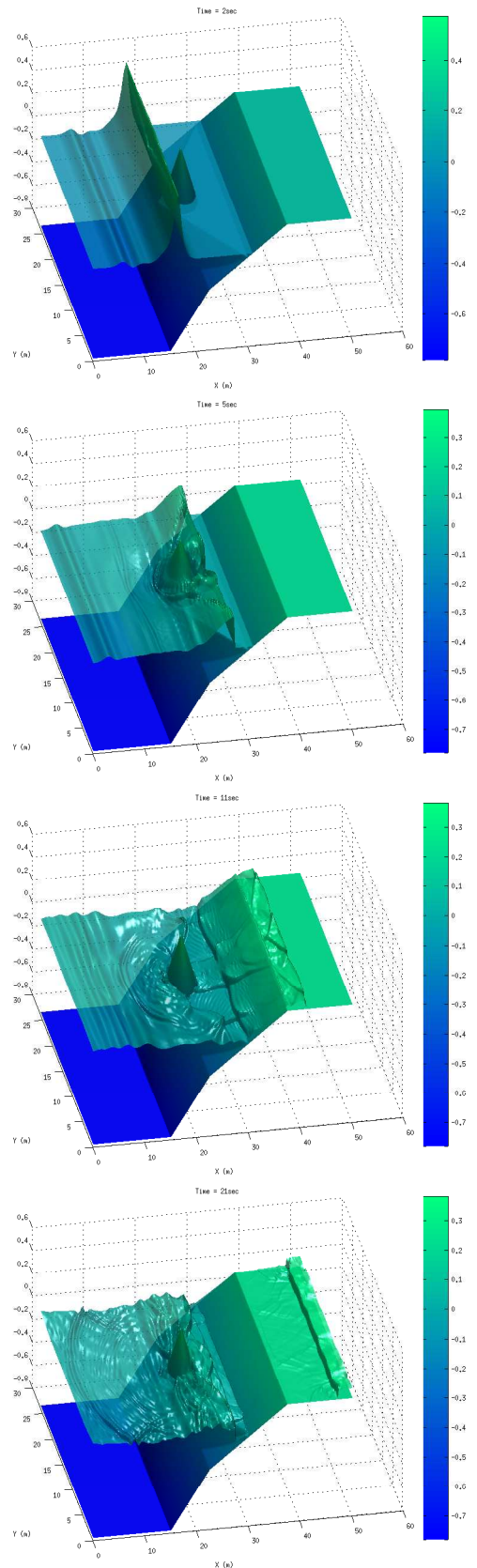


Figure 10: Numerical snapshots when time = 2, 5, 11, and 21 sec.

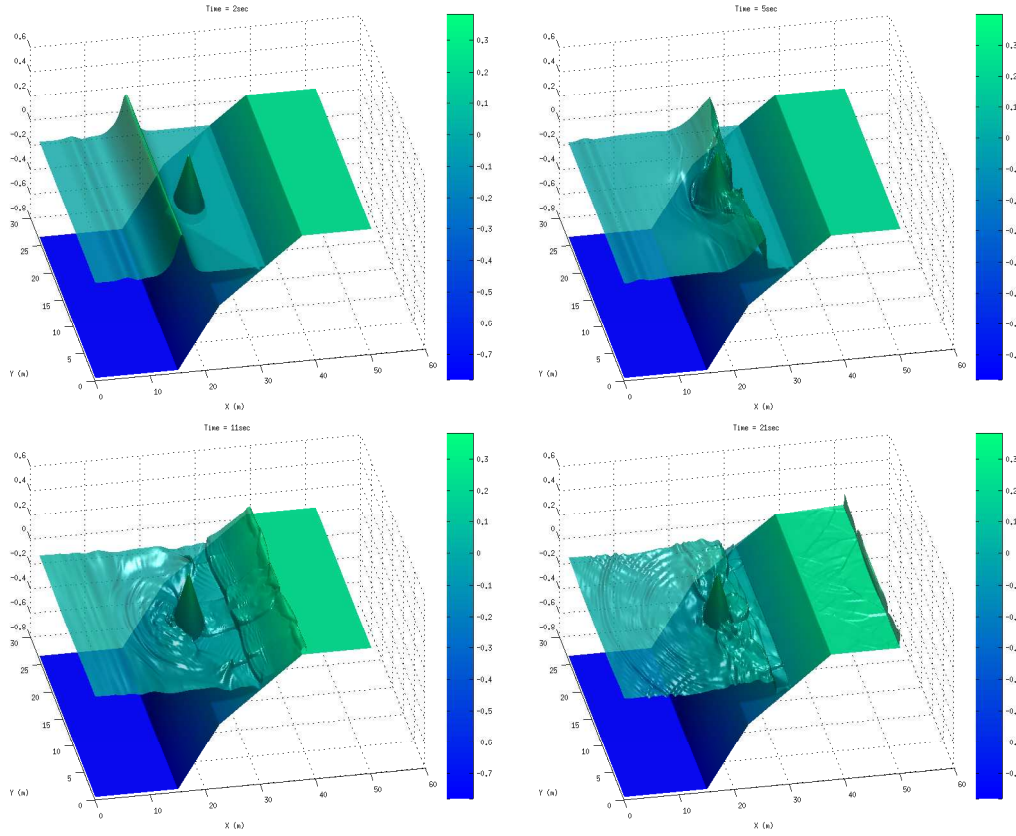


Figure 11: Numerical snapshots when time is 2, 5, 11, and 21 sec for an initialized amplitude is 0.32 m.

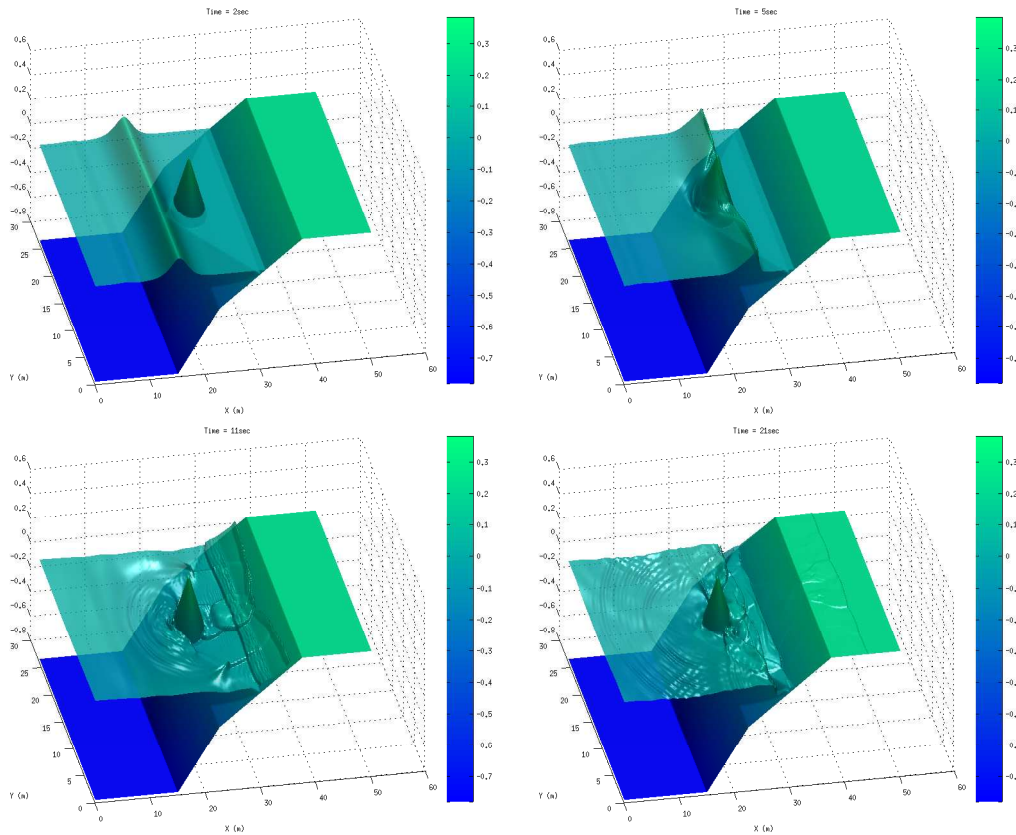


Figure 12: Numerical snapshots when time is 2, 5, 11, and 21 sec for an initialized amplitude is 0.16 m.

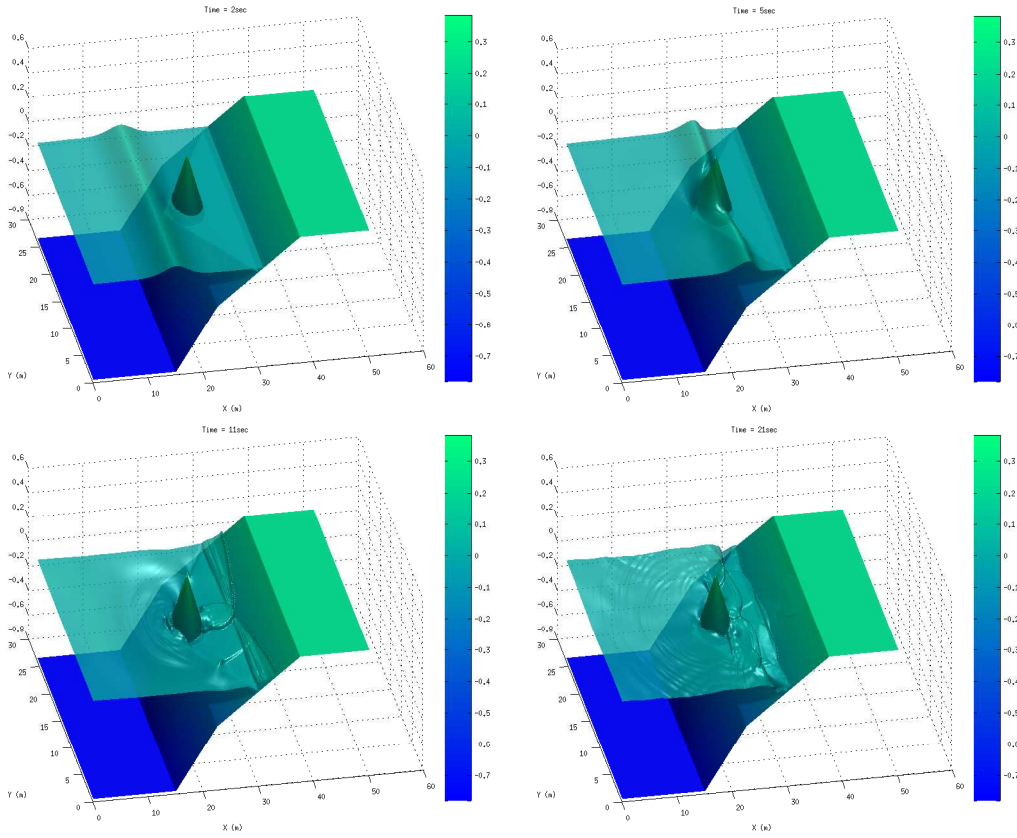


Figure 13: Numerical snapshots when time is 2, 5, 11, and 21 sec for an initialized amplitude is 0.08 m.

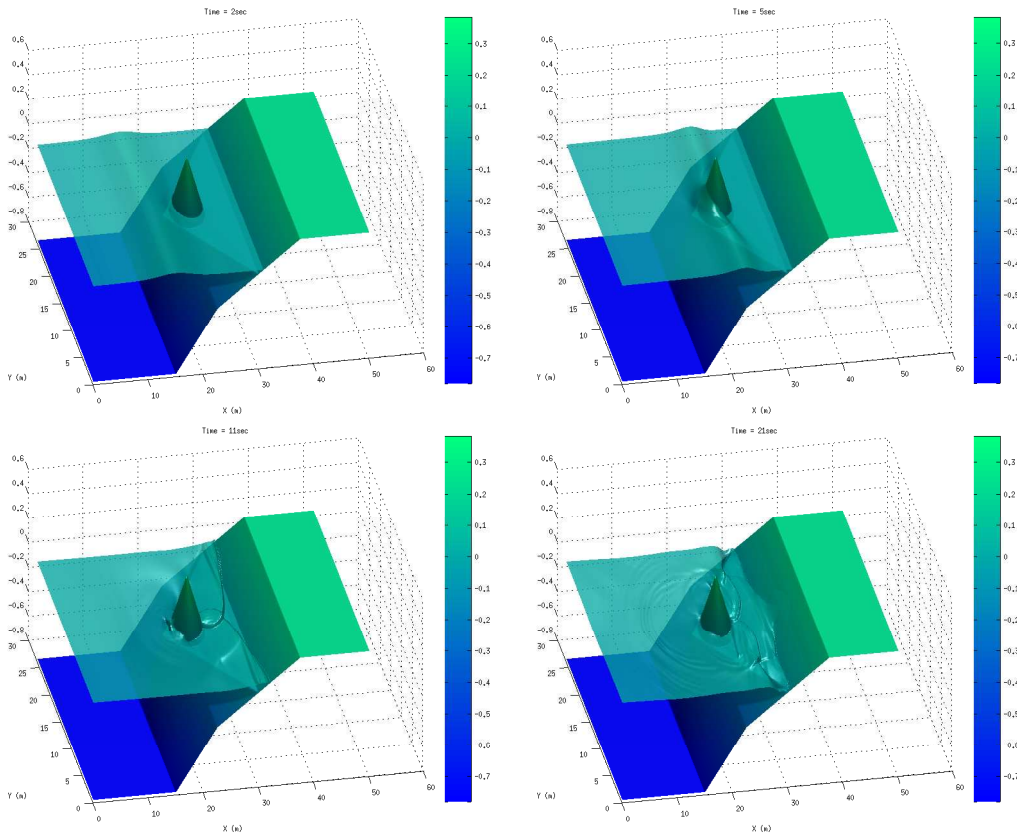


Figure 14: Numerical snapshots when time is 2, 5, 11, and 21 sec for an initialized amplitude is 0.04 m.

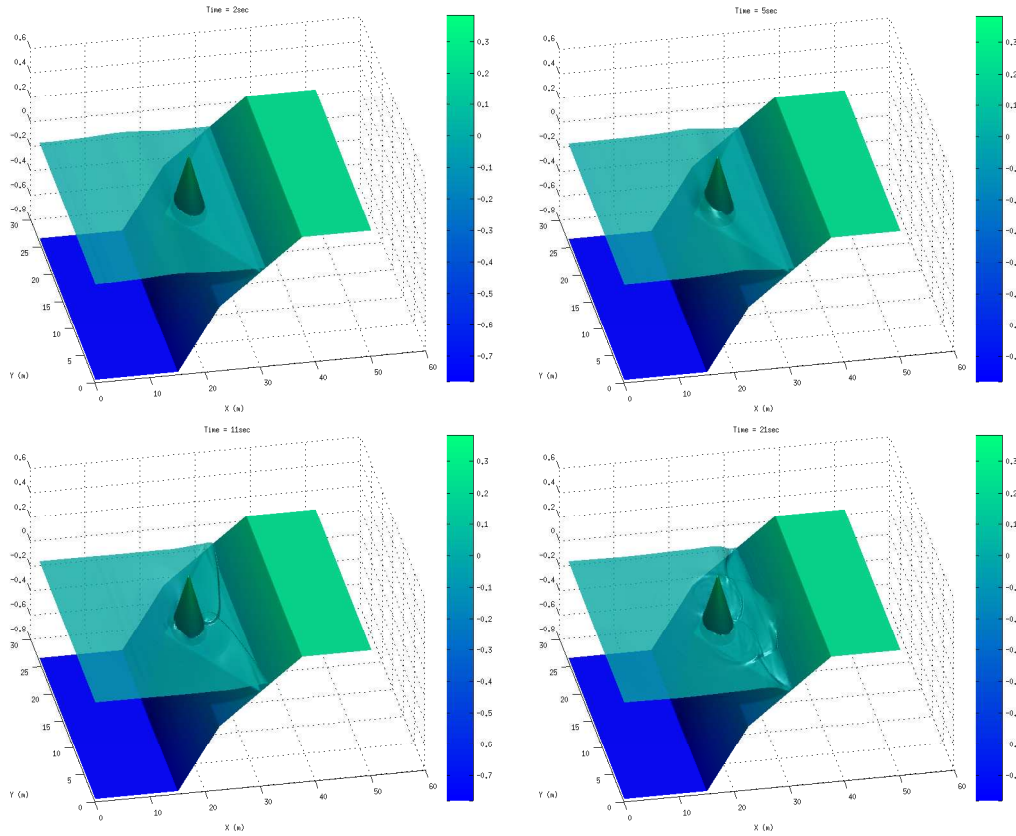


Figure 15: Numerical snapshots when time is 2, 5, 11, and 21 sec for an initialized amplitude is 0.02 m.

has high performance for simulation of various initialized amplitudes. In other word, we can simulate tsunamis inundation, and can estimate about tsunamis hazard when tsunamis attack any human's assets on coastline zone.

However, we not measure runup testing because of located gauge stations setting problem. So we measure only computational time consuming when we vary an initialized amplitude in Table 2.

Table 2: Numerical experiment results

Initialized Amplitude (meters)	Computational time consuming (minuets and seconds)
0.55	41 m 59.258 s
0.32	39 m 31.897 s
0.16	37 m 15.319 s
0.08	36 m 39.716 s
0.04	35 m 43.115 s
0.02	35 m 24.082 s

We surprisingly found that a decreasing of initialized amplitude causes a decreasing of computational time consuming. However, this problem consume a lot of computational time (about 40 minutes). So this problem should be solved by using a parallel programming.

## FUTURE WORKS

This work is a detail in 2004 Indian Ocean tsunami simulation project. It means that there is a lot of future works. First, the computational time consuming problem should be solved when FUNWAVE extended in MPI parallel programming in server computer. Then the two-dimensional solitary wave simulation is transformed into a spherical coordinates with Coriolis effect. Finally, the surface elevation near coastline is compared to a surface elevation data from gauge stations of Thailand for estimation of tsunamis hazard.

## REFERENCES

Shi, F. and J. T. Kirby, 2012, A high-order adaptive time-stepping tvd solver for boussinesq modeling of breaking waves and coastal inundation: Ocean Modelling, 36–51.



# Simulation of Electromagnetic Cloaking using Transformation Optics

Panuwat Pukhamwong and Chaiwoot Boonyasiriwat

## ABSTRACT

Metamaterials are artificial material with a wide range of values of electromagnetic properties such as permittivity and permeability. They can be used to build unconventional electromagnetic devices such as electromagnetic cloaking. In this work, we study an electromagnetic cloaking system using a computational approach. To simulate electromagnetic cloaking, appropriate values of material electromagnetic properties must be used to manipulate electromagnetic wave to reduce the scattered field due to the cloaking system. We design an electromagnetic cloaking by using an optical transformation to obtain the required value of permittivity and permeability. Then we perform simulation of full-waveform electromagnetic cloaking using finite-difference time-domain (FDTD) method. The numerical result shows that there is still some scattered field due to the cloaking system. This problem is still needed to be solved in our future work.

## INTRODUCTION

There are metamaterials which can be achieved either vary large or vary small value of permittivity and permeability, including negative value. Metamaterials can also be obstructed to have continually various value of permittivity and permeability in spatial space. Because of these, metamaterial have a lot of applications. One interesting application of these materials is that they are possible to use in building electromagnetic cloaking device.

Invisibility or electromagnetic cloaking have been appealing from mankind for several years. There are many way to approach this system. Based on a coordinate transformation approach, Pendry et al. (2006) have reported and the simulation of Cummer et al. (2006) verifies this system. We study the system which use transformation optics to obtain parameter of device which metamaterials have been used in constructing as shown in Figure 1.

The outline of this paper is as follows. We first introduce metamaterials and transformation optics. Then numerical method used for simulation is presented followed by numerical results Finally a summary is drawn.

## THEORY

### Metamaterials

Metamaterial is a artificial structure whose dimensions are much smaller than the wavelength which interact with to satisfy the condition which we can treat the metamaterial as a average medium. This medium can be modeled by constitutive parameters. In case of electromagnetic, the medium is characterized by electric permittivity and magnetic permeability. The permittivity and permeability of material describe the response of medium to electromagnetic wave.

The common benefits of metamaterials are that they are compound materials, we can construct material to have a various value of permittivity and permeability, and the other is that they can provide convenient permittivity and permeability.

When light travel through different materials or space it change direction. The parameters of material which involve the interaction between electromagnetic wave and that material are Electric permittivity and magnetic permeability. The permittivity and permeability of material could be derived from the methodology of transformation optic. This process will give us how those parameters of electromagnetic cloaking device could be.

### Transformation optics

Consider a coordinate transformation from the Cartesian space  $(x, y, z)$  to an arbitrary curved space described by coordinates  $(u, v, w)$

$$\begin{aligned}x &= f_1(u, v, w), \\y &= f_2(u, v, w),\end{aligned}$$

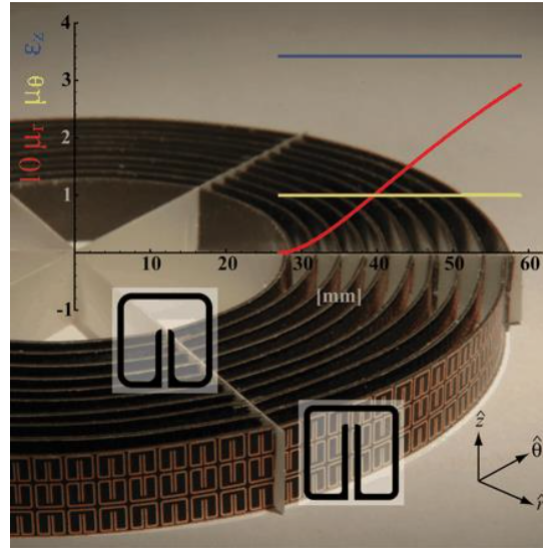


Figure 1: The experimental of transformation-based cloaking at microwave frequencies. (After Schurig et al. (2006))

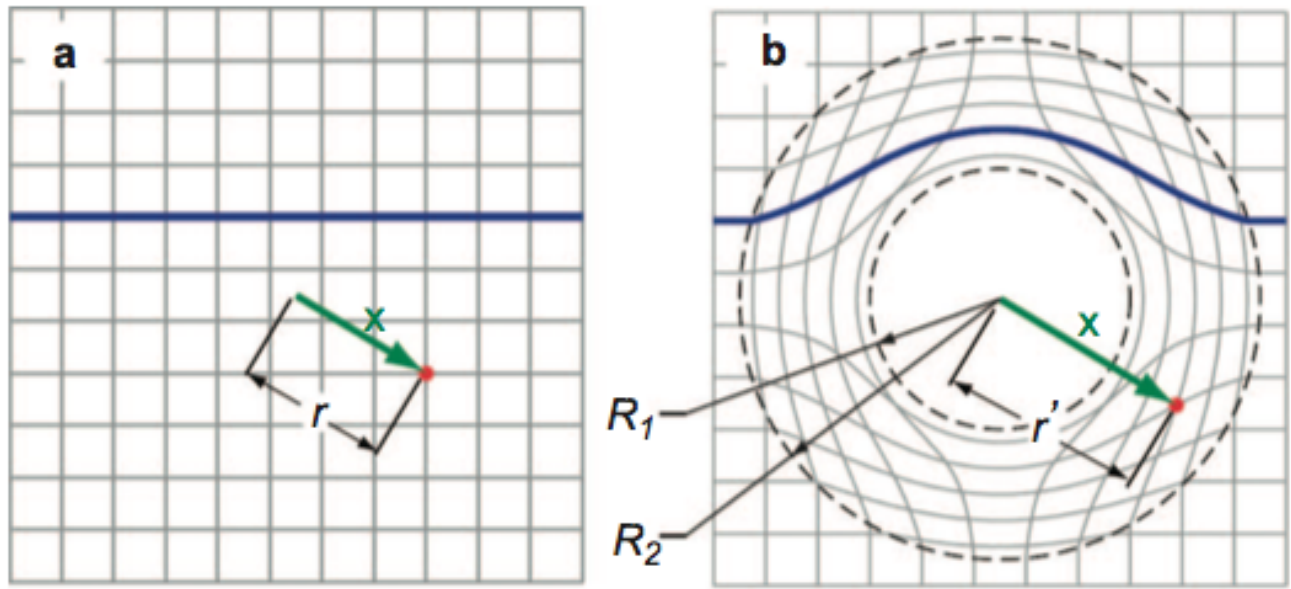


Figure 2: (left) Field line in free space with the back-ground Cartesian coordinate grid shown. (right) Distorted field line with the background coordinates distorted. (After Pendry et al. (2006))

$$z = f_3(u, v, w)$$

In order to keep invariant forms of Maxwells equations, the new permittivity and permeability tensors have to be

The Jacobian transformation matrix is written as

$$\Lambda = \begin{bmatrix} \frac{\partial x}{\partial u} & \frac{\partial x}{\partial v} & \frac{\partial x}{\partial w} \\ \frac{\partial y}{\partial u} & \frac{\partial y}{\partial v} & \frac{\partial y}{\partial w} \\ \frac{\partial z}{\partial u} & \frac{\partial z}{\partial v} & \frac{\partial z}{\partial w} \end{bmatrix} \quad (1)$$

$$\bar{\epsilon}_{new} = \det(\Lambda)(\Lambda)^{-1}\bar{\epsilon}(\Lambda)^{-T} \quad (2)$$

$$\bar{\mu}_{new} = \det(\Lambda)(\Lambda)^{-1}\bar{\mu}(\Lambda)^{-T} \quad (3)$$

We consider the comparison space as free space and then transform to real space.

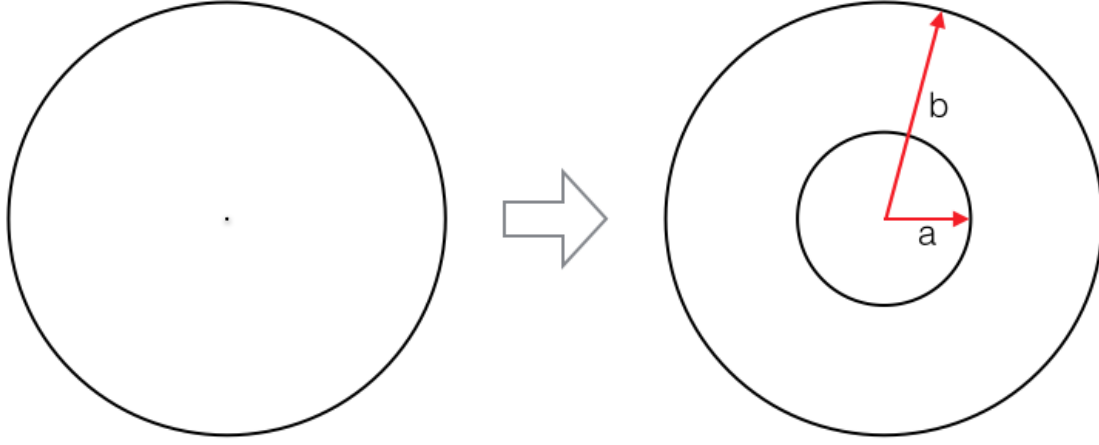


Figure 3: (left) comparison space, (right) real space.

The relation between two spaces should be (for linear transform)

$$r' = \frac{b-a}{b}r + a \quad (4)$$

The total Jacobian transformation could be

$$\Lambda = \Lambda_{xr} \Lambda_{rr'} \Lambda_{r'x'} \quad (5)$$

where  $\Lambda_{xr}$  denotes change of Cartesian coordinates to cylindrical coordinates,  $\Lambda_{rr'}$  denote the transformation from the original cylindrical coordinates to new cylindrical coordinates,  $\Lambda_{r'x'}$  denotes change of the new cylindrical coordinates back to Cartesian coordinates.

$$\epsilon_{xx} = \frac{r-a}{r} \cos^2 \phi + \frac{r}{r-a} \sin^2 \phi \quad (6)$$

$$\epsilon_{yy} = \frac{r-a}{r} \sin^2 \phi + \frac{r}{r-a} \cos^2 \phi \quad (7)$$

$$\epsilon_{xy} = \epsilon_{yx} = \left( \frac{r-a}{r} - \frac{r}{r-a} \right) \cos \phi \sin \phi \quad (8)$$

$$\mu_{zz} = \left( \frac{b}{b-a} \right)^2 \left( \frac{r-a}{r} \right) \quad (9)$$

another are zero.

note that: These are relative permittivity and relative permeability.

## METHODS

We simulate electromagnetic wave using Maxwell's equation, Faraday's law and Ampere's law, as governing equations (eq 2.7). The other two equations describe interaction between electromagnetic wave and space.

$$\frac{\partial \vec{B}}{\partial t} = -\nabla \times \vec{E} \quad (\text{Faraday's law}) \quad (10)$$

$$\frac{\partial \vec{D}}{\partial t} = \nabla \times \vec{H} \quad (\text{Ampere's law}) \quad (11)$$

$$\vec{D} = \bar{\epsilon} \vec{E} \quad (12)$$

$$\vec{B} = \bar{\mu} \vec{H} \quad (13)$$

## 2D TE mode

For the 2D TE mode, we assume that there are no variations of either the fields or the excitation in z direction. Faraday's law and Ampere's law are reduced to

$$\frac{\partial B_z}{\partial t} = \frac{\partial E_x}{\partial y} - \frac{\partial E_y}{\partial x} \quad (14)$$

$$\frac{\partial E_x}{\partial t} = \frac{\partial H_z}{\partial y} \quad (15)$$

$$\frac{\partial E_y}{\partial t} = -\frac{\partial H_z}{\partial x} \quad (16)$$

## Finite different time domain (FDTD)

FDTD was applied to solve the PDE

$$\frac{\partial f}{\partial x} \approx \frac{f(x+h) - f(x-h)}{2h}, \quad (17)$$

$$\frac{\partial f}{\partial t} \approx \frac{f(t+\Delta t) - f(t)}{\Delta t}. \quad (18)$$

We proceed with discretization of Maxwells equations based on staggered grid as show in Figure 4.1.

the spatial positions of the two electric field components and the single magnetic field component. The  $E_x$  and  $D_x$  component is located at half x and integer y grid points, while the  $E_y$  and  $D_y$  component is located at integer x and half y grid points, and the magnetic component  $H_z$  and  $B_z$  is located at half x and half y grid points.

The spatially discretized of the component Maxwells Equa-

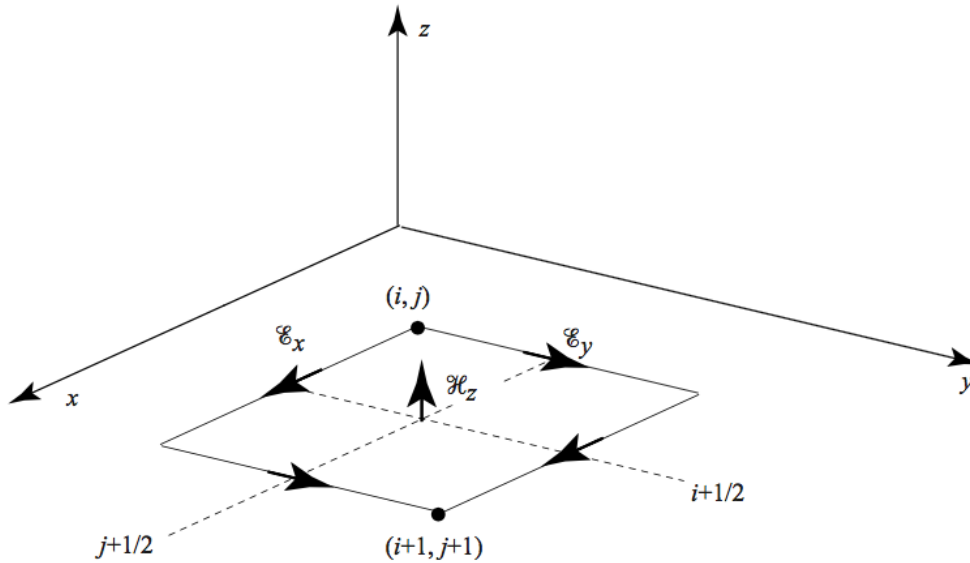


Figure 4: Staggered grid for an FDTD unit cell for transverse electric (TE) waves. (After Inan and Marshall (2011))

tions are

$$\begin{aligned}
 B_z^{n+1,i,j} &= B_z^{n,i,j} + \frac{\Delta t}{\Delta x} [E_x^{n,i,j+1} - E_x^{n,i,j}] \\
 &\quad - \frac{\Delta t}{\Delta y} [E_y^{n,i+1,j} - E_y^{n,i,j}] \\
 D_x^{n+1,i,j} &= D_x^{n,i,j} + \frac{\Delta t}{\Delta y} [H_z^{n,i,j} - H_z^{n,i,j-1}] \\
 D_y^{n+1,i,j} &= D_y^{n,i,j} - \frac{\Delta t}{\Delta x} [H_z^{n,i,j} - H_z^{n,i-1,j}]
 \end{aligned}$$

## Anisotropic media

The result from transformation optics provide an anisotropic media which is the parameters of media are function of vector direction of electric and magnetic field.

The permittivity and permeability are written in tensor form.

$$\bar{\epsilon} = \epsilon_0 \begin{bmatrix} \epsilon_{xx} & \epsilon_{xy} & \epsilon_{xz} \\ \epsilon_{yx} & \epsilon_{yy} & \epsilon_{yz} \\ \epsilon_{zx} & \epsilon_{zy} & \epsilon_{zz} \end{bmatrix} \quad (19)$$

$$\bar{\mu} = \mu_0 \begin{bmatrix} \mu_{xx} & \mu_{xy} & \mu_{xz} \\ \mu_{yx} & \mu_{yy} & \mu_{yz} \\ \mu_{zx} & \mu_{zy} & \mu_{zz} \end{bmatrix} \quad (20)$$

From eq 2.7 we can written as

$$\frac{\partial \bar{D}}{\partial t} = \nabla \times \bar{H} \quad (21)$$

$$\bar{E} = [\bar{\epsilon}]^{-1} \bar{D} \quad (22)$$

$$\frac{\partial \bar{B}}{\partial t} = -\nabla \times \bar{E} \quad (23)$$

$$\bar{H} = [\bar{\mu}]^{-1} \bar{B} \quad (24)$$

## Interface

Because we solve the problem in Cartesian coordinates, to get more accuracy about interface which is cylindrical we average the parameter at interface.

The result of this process is showed below (Figure 2.5).

## NUMERICAL RESULTS

The cylindrical cloak was constructed in middle of square domain of the model. We generate plane wave form of electromagnetic wave at left of model. The right edge of model is absorbing boundary, one way wave. The top and bottom of model are Neumann's boundary to satisfy plane wave. Siting of model is showed below.

The relative permittivity and relative permeability which we obtain from transformation are showed below (Figure 3.2). The parameter at inner boundary of a cylindrical cloak is inherently singular, make inverse value go to infinity. We avoid this problem by remove a thin layer from the inner boundary and replace with a thin perfect electric conductor (PEC) shell. The result of full wave form simulation are showed below. The result from our simulation are comparable to the result from simulation in Cummer et al. (2006) (Figure 3.4).

## SUMMARY

Our simulate cloaking system without effect of dispersion of permittivity and permeability are comparable to the simulation in the simulation of Cummer et al. (2006). To predict and match experiment about the loss and the narrow bandwidth limit of metamaterials we have to implement dispersion effect of media.

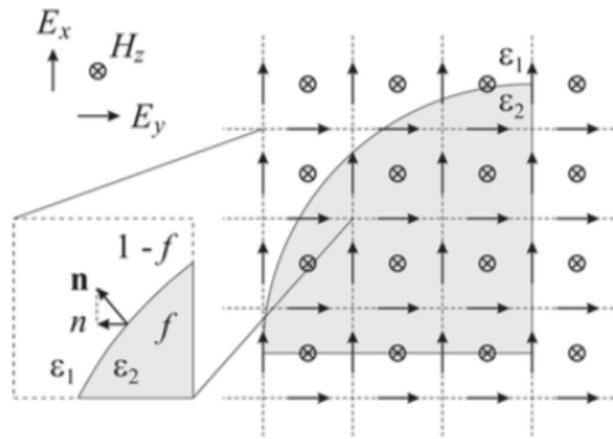


Figure 5: Parameter  $f$  is the ratio of material in each square area. (After Zhao and Hao (2007))

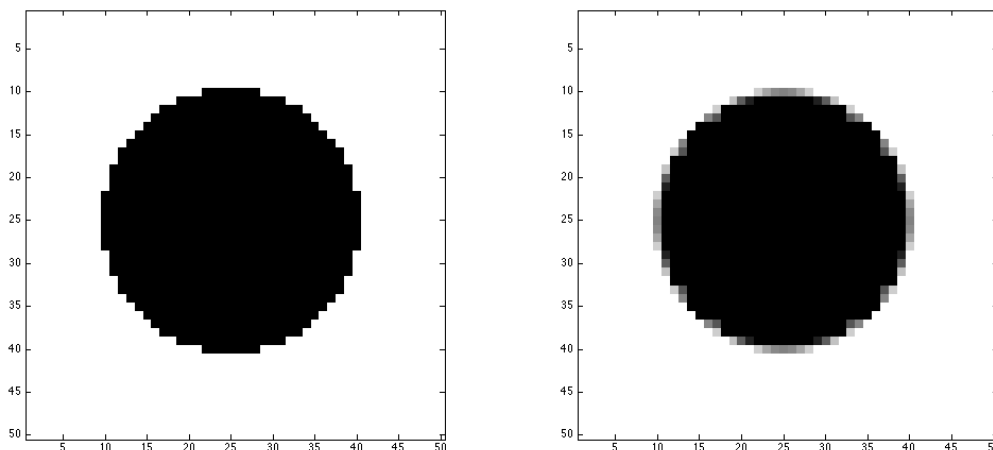


Figure 6: The result of average area, color show the ratio of material, black equal to one and white equal to zero

### ACKNOWLEDGMENTS

We would like to thank members of the Mahidol University Center for Scientific Computing (MCSC) group for comments and suggestions.

### REFERENCES

- Cummer, S. A., B.-I. Popa, D. Schurig, D. R. Smith, and J. Pendry, 2006, Full-wave simulations of electromagnetic cloaking structures: *Physical Review E*, **74**, no. 036621.
- Inan, U. S. and R. A. Marshall, 2011, *Numerical electromagnetics the fdtd method*: Cambridge University Press.
- Pendry, J., D. Schurig, and D. Smith, 2006, Controlling electromagnetic fields: *Science*, **312**, 1780–1782.
- Schurig, D., J. J. Mock, B. J. Justice, S. A. Cummer, J. B. Pendry, A. F. Starr, and D. R. Smith, 2006, Metama-

terial electromagnetic cloak at microwave frequencies: *Science*, **314**, 977980.

- Zhao, Y. and Y. Hao, 2007, Finite-difference time-domain study of guided modes in nano-plasmonic waveguides: *IEEE Transactions on Antennas and Propagation*, **55**, no. 11, 30703077.

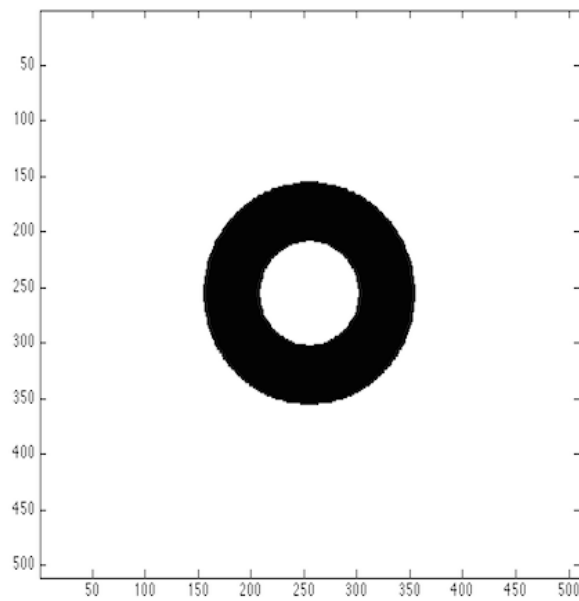
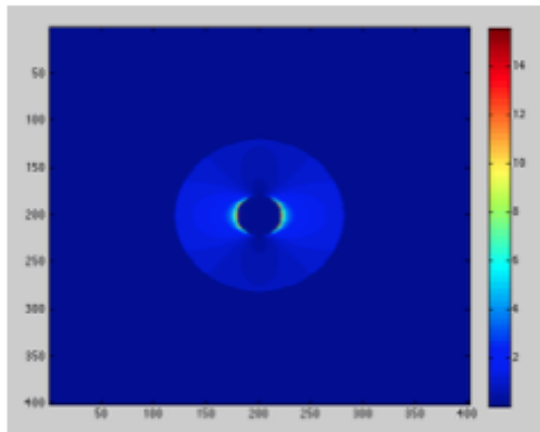
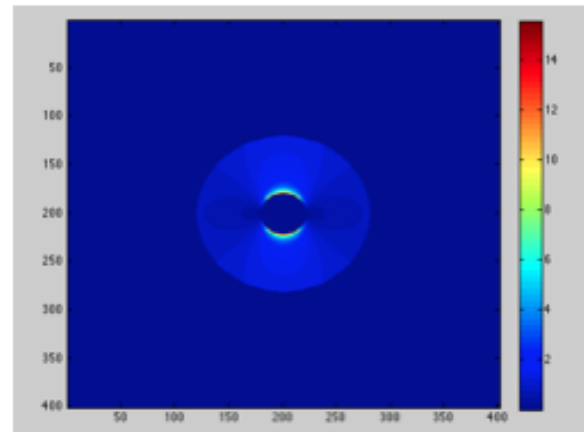


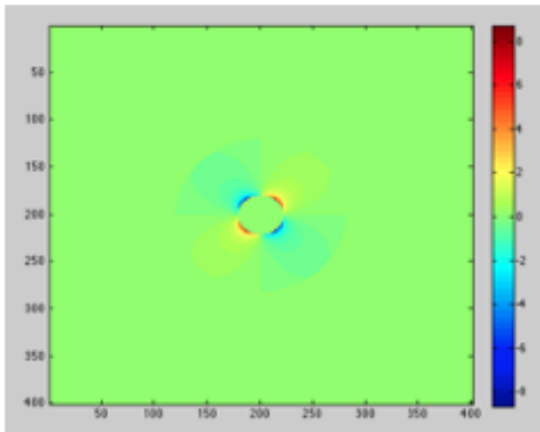
Figure 7: White is free space, Black is the cloaking device which have values  $a = 27.1$  mm and  $b = 58.9$  mm.



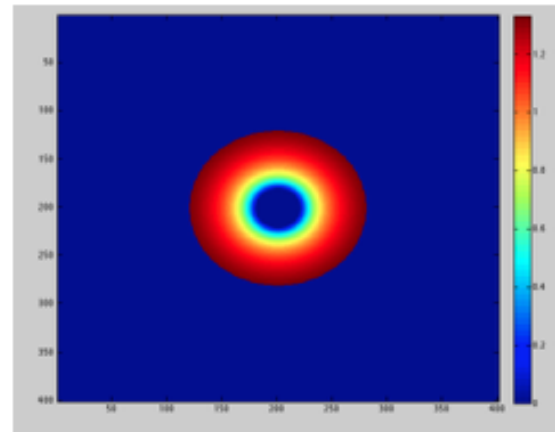
permittivity (xx)



permittivity (yy)



permittivity (xy, yx)



permeability (zz)

Figure 8: The relative permittivity and relative permeability in model

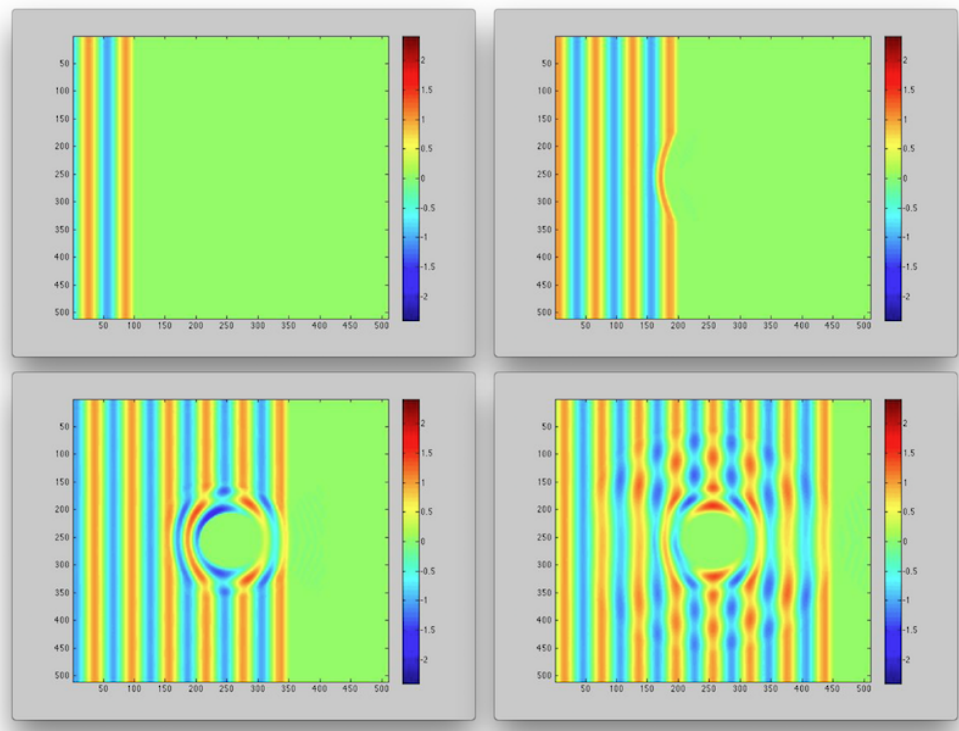


Figure 9: The simulation result with operating source 8.5 GHz of frequency. Source is plane wave that coming from the left of model.

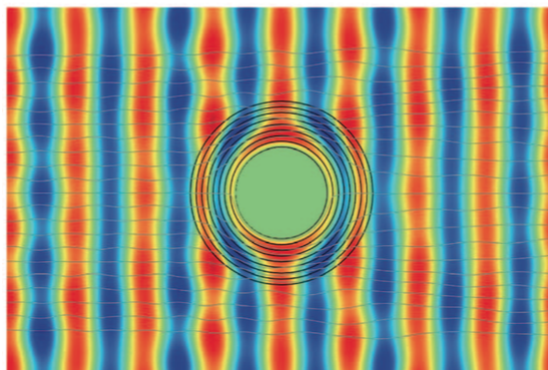


Figure 10: The simulation of approximation of the ideal parameters. (After Cummer et al. (2006))

# Simulation of Flow Past a Square Cylinder

Nattapon Pongchanwit and Chaiwoot Boonyasiriwat

## ABSTRACT

We simulate flow around a square cylinder by solving the incompressible Navier-Stokes equations to study the characteristics and flow pattern for various Reynolds numbers (Re). The 2D time-dependent problem is solved on a rectangular domain by using a finite difference method on a staggered grid, an implicit viscosity step, and a projection method for the pressure. For a steady-state laminar flow between fixed parallel plates (without square cylinder), the velocity profiles is consistent with the theory. With the present of a body, we can simulate the von Karman vortex street.

## INTRODUCTION

Most fluid dynamics problems cannot be solved analytically. One way to obtain their approximate solutions is a numerical approximation. The numerical accuracy depends on numerical method used. Numerical solutions can then be visualized as images to aid the analysis of the problem.

Actually, drag force do not depends only on velocity of fluid flow. The drag coefficient is not a constant along the trajectory of a object. The drag force can compute from pressure around the object. Thus, we need to know the characteristics of fluid flow to compute the pressure. Obviously fluid mechanic play a role in this work.

The flow past bluff bodies, especially cylinders, have been an attraction in all kinds of fluid mechanical investigations for a long time. Most of these studies were concerned with circular and square cylinder cases under free flow condition. In this work, we study the pattern of flow past a square cylinder at various Reynolds numbers (Re) by following Seibold's process Seibold (2008) using the physical setting proposed by Breuer (Breuer and Bernsdorf, 2000)

## THEORY

We consider the 2D incompressible Navier-Stokes equations in nondimensional forms on a rectangular domain (Fox et al., 2006).

$$\begin{aligned}\frac{\partial u}{\partial t} + \frac{\partial p}{\partial x} &= -u \frac{\partial u}{\partial x} - v \frac{\partial u}{\partial y} + \frac{1}{\text{Re}} \left( \frac{\partial^2 u}{\partial x^2} + \frac{\partial^2 u}{\partial y^2} \right) \\ \frac{\partial v}{\partial t} + \frac{\partial p}{\partial x} &= -u \frac{\partial v}{\partial x} - v \frac{\partial v}{\partial y} + \frac{1}{\text{Re}} \left( \frac{\partial^2 v}{\partial x^2} + \frac{\partial^2 v}{\partial y^2} \right) \\ \frac{\partial u}{\partial x} + \frac{\partial v}{\partial y} &= 0\end{aligned}$$

where  $u$  is the flow velocity in x axis,  $v$  is the flow velocity in y axis,  $p$  is the pressure, and Re is the Reynolds number ( $\rho U d / \mu$ ).

The momentum equations (2.1) and (2.2) describe the time evolution of the velocity field under inertial and viscous forces. The conservation of mass is achieved through the continuity equation (2.3) for incompressible flow. The Reynolds number is defined as the ratio of inertial forces to viscous forces. The Reynolds number can be used to determine dynamic similitude between laminar and turbulent cases of fluid flow. Laminar flow occurs at low Reynolds numbers, where viscous forces are dominant, and is characterized by smooth, constant fluid motion. Turbulent flow occurs at high Reynolds numbers and is dominated by inertial forces, which tend to produce chaotic eddies.

## Numerical Solution Approach

We split the whole process by computing intermediate velocities ( $u^*$ ,  $v^*$ ,  $u^{**}$ , and  $v^{**}$ ) to obtain the solution at next time step ( $u^{n+1}$ ,  $v^{n+1}$ , and  $p^{n+1}$ ). The general approach of the code is described in Section 6.7 in the book *Computational Science and Engineering* (Strang, 2007).



tered stencil.

$$\left(\frac{\partial^2 u}{\partial x^2}\right)_{i,j} + \left(\frac{\partial^2 u}{\partial y^2}\right)_{i,j} \approx \frac{u_{i-1,j} - 2u_{i,j} + u_{i+1,j}}{h_x^2} + \frac{u_{i,j-1} - 2u_{i,j} + u_{i,j+1}}{h_y^2} \quad (4)$$

### SETTING

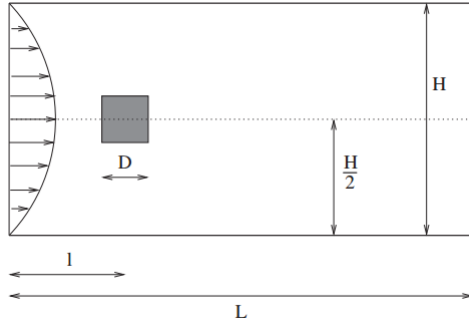


Figure 2: Setting Condition

The problem configuration is similar to the one by Breuer as shown in Figure 3.2: it has a cylinder with square cylinder with diameter (width)  $D$  mounted and centered inside a plane channel of  $H$  with blockage ratio  $B = 1/8$ . The channel length  $L$  was fixed at  $L/D = 50$  to reduce the influence of in flow and out flow boundary condition.

### Boundary Condition

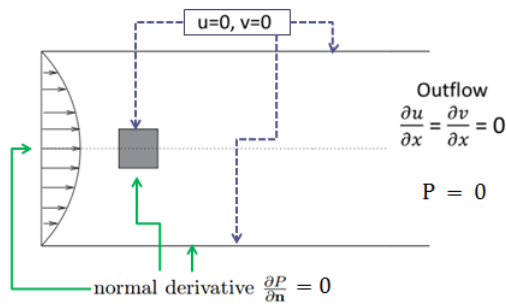


Figure 3: Boundary Condition

In order to simulate a fully developed laminar channel flow upstream of the square cylinder, a parabolic velocity profile is prescribed at the channel inlet. The velocity in normal direction to boundary does not changes in the outlet. we apply no-slip condition at the wall and square cylinder. A stagnation pressure condition assumes stagnation conditions outside the boundary so that the velocity at the boundary is zero. Zero static pressure condition assumes only that the normal fluid velocity at the boundary has a zero gradient.

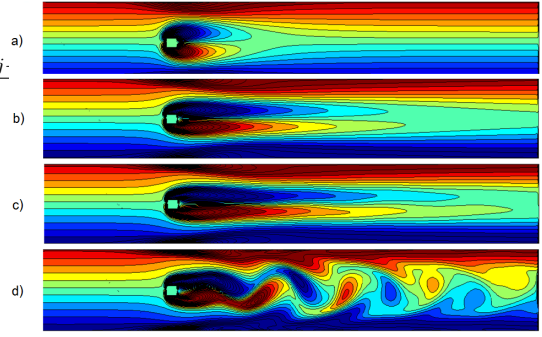


Figure 4: Vorticity contour plot of results at  $t = 15$ : a)  $Re = 10$ ; b)  $Re = 40$ ; c)  $Re = 60$ ; d)  $Re = 80$ .

### NUMERICAL RESULTS

At small Reynolds numbers ( $10 < Re < 70$ ), the flow separates at the trailing edges of the cylinder and a closed steady recirculation region consisting of two symmetric vortices is observed behind the body. The size of the recirculation region increases with increase in  $Re$ . When a critical Reynolds number  $Re_{cri}$  is exceeded about 80, the well-known von Karman vortex street with periodic vortex shedding from the cylinder can be detected in the wake.

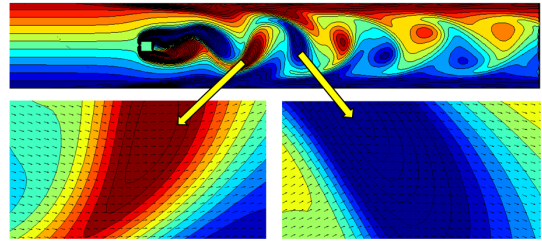


Figure 5: Vorticity contour plot of results at  $t = 15$  for  $Re = 120$

Vorticity contour plot ( $\vec{\omega} = \nabla \times \vec{u}$ ) describes the rotation of fluid. As in the bottom left of figure 3, the fluid is moving in a counter-clockwise direction but is moving in a clockwise direction in the bottom right. Vortices move backward, so the fluid move and oscillate behind a square cylinder.

Since this problem is symmetrical flow around a square cylinder, then why increase of  $Re$  results in the symmetry breaking of the flow. We expect vortex streets start on one side of a body or the other due to some slight random fluctuation from upstream symmetry in physical experiments and due to rounding error. And we try to investigate why asymmetry occur at low  $Re$  ( $Re = 10$ ) in our future work.

## CONCLUSION

We simulate flow around a square cylinder by solving the incompressible Navier-Stokes equations by using a finite difference method on a staggered grid, an implicit viscosity step, and a projection method. Finally, The von Karman vortex street can be simulated when  $Re_{crit} \approx 80$ . And the method will diverge about  $Re \approx 190$  (for time step = 0.02).

As we expect the symmetry breaking occur because of rounding error. To test the hypothesis, we can do it by decreasing of grid space and time step to check whether the von Karman vortex street occurring at the same Reynolds number. And this is our future work.

## ACKNOWLEDGMENTS

We would like to thank Benjamin Seibold for prototype code of the lid driven cavity problem.

## REFERENCES

- Breuer, M. and J. Bernsdorf, 2000, Accurate computations of the laminar flow past a square cylinder based on two different methods: lattice-boltzmann and finite-volume: *International Journal of Heat and Fluid Flow*, **21**, no. 2, 186–196.
- Fox, R. W., A. T. McDonald, and P. J. Pritchard, 2006, *Introduction to fluid mechanics*: John Wiley & Sons Inc.
- Seibold, B., 2008, A compact and fast matlab code solving the incompressible navier-stokes equations on rectangular domains. MIT Technical Report.
- Strang, G., 2007, *Computational science and engineering*: Wellesley-Cambridge Press.

# Simulation of Smoke in Two Dimensions using Finite Difference Method in MATLAB

Thanakorn Chanthanasaro and Chaiwoot Boonyasiriwat

## ABSTRACT

In this work, smoke from a candle is modeled as an incompressible, viscous fluid. The governing equations including the continuity equation, the Navier-Stokes equations, the advection-diffusion equations for heat and smoke concentration were numerically solved using the finite difference method on a staggered grid and the pressure-correction method. A simulation program was developed in MATLAB based on the code of Seibold (2008). Our program was successfully used to simulate smoke in a 2D rectangular domain. Numerical results show that symmetric flows were obtained when kinematic viscosity was higher than  $10^{-4}$  while asymmetric flows occurred when kinematic viscosity was lower than the critical value. Flow patterns also depend on the time lag between the releases of heat and smoke sources as expected but the simulated patterns are not consistent with real observations. Further work must be performed to improve the simulation results.

## INTRODUCTION

Simulating realistic fluids is a challenging problem both in computer graphic and fluid dynamics studying Fedkiw et al. (2001), Stam (1999). Though there are many software that can simulate things easily nowadays, but understanding its physics behind is important. All we have to do when simulate water is solving Navier-Stokes equations. In case of smoke, advection-diffusion equation of heat and smoke are needed to be solved together. In this work, we study the effect of viscosity and the existence of fluid flow to the flow pattern. Since these equations are hard to be solved analytically, numerical method is used to numerically solve these equations. My MATLAB code is modified from code of Seibold (2008). In the theory part, I follow the book Fluid Simulation for Computer Graphics Bridson (2008).

## THEORY

When the flow's velocity is well below the speed of sound. The compressible effect of the flow can be neglected. Flow behavior is described by incompressible Navier-Stokes equations given by

$$\nabla \cdot \mathbf{u} = 0 \quad (1)$$

$$\frac{\partial \mathbf{u}}{\partial t} + (\mathbf{u} \cdot \nabla) \mathbf{u} = -\frac{1}{\rho} \nabla p + \nu \nabla^2 \mathbf{u} + \mathbf{f} \quad (2)$$

where  $\mathbf{u} = (u, v, w)$  or  $(u, v, 0)$  in two-dimensional is the fluid's velocity,  $p$  is its pressure,  $\rho$  is its density,  $\nu$  is its kinematic viscosity, and  $\mathbf{f}$  is an external force. Navier-Stokes equations state that the velocity should conserve both mass (Equation (1)) and momentum (Equation (2)). Momentum equation is solved from Newton's equation. LHS of momentum equation is rate of change of velocity. Its second term is the rate due to moving of the fluid. Where RHS of momentum equation is the force accounted. Its first term is from the gradient of the pressure and its second term is from the viscosity effect.

In case of smoke simulation, there are two more equation needed for the evolution of two scalar variables temperature  $T$  and concentration of the smoke  $s$  given by

$$\frac{\partial T}{\partial t} + (\mathbf{u} \cdot \nabla) T = k_T \nabla^2 T + r_T (T_{source} - T) \quad (3)$$

$$\frac{\partial s}{\partial t} + (\mathbf{u} \cdot \nabla) s = k_s \nabla^2 s + r_s \quad (4)$$

where  $k_T$  and  $k_s$  are diffusion coefficient of temperature and concentration of smoke respectively,  $r_T$  is the rate that the heat is released,  $r_s$  is the rate that smoke is released, and  $T_{source}$  is the temperature of the source point. Equation (3) and (4) are called advection-diffusion equation of heat and concentration of smoke. They account rate of change of each variable due to moving of the fluid (the second term of LHS) and the diffusion effect (the first term of RHS). The last terms of equations (3) and (4) are source terms.

Next, the fluid density is linearly approximated to be function of temperature  $T$  and concentration of smoke  $s$  as

$$\rho = \rho_0[1 + \alpha s - \beta(T - T_{amb})] \quad (5)$$

where  $\rho_0$  is the smoke-free air density at ambient temperature,  $\alpha$  and  $\beta$  are two positive constants, and  $T_{amb}$  is ambient temperature. Plugging this into momentum equation. The static pressure  $\rho_0 \mathbf{g}$  is added to the variation pressure to new pressure. Using the *Boussinesq* approximation, assume that  $|\alpha s - \beta \Delta T| \ll 1$ , leading to

$$\frac{\partial \mathbf{u}}{\partial t} + (\mathbf{u} \cdot \nabla) \mathbf{u} = -\frac{1}{\rho_0} \nabla p + \nu \nabla^2 \mathbf{u} + (\alpha s - \beta \Delta T) \mathbf{g} \quad (6)$$

where  $\Delta T = T - T_{amb}$ . The last term of equation (6) is the external force. Smoke falls down due to gravity force and rises up due to hot air. Note that when  $s = 0$  and  $T = T_{amb}$ , this force is zero.

## METHODS

2D smoke is simulated on a rectangular domain using finite difference method, discretized on staggered grid shown in figure 1, and projection method for the pressure. The solution of next time step ( $u^{n+1}, v^{n+1}, p^{n+1}, T^{n+1}$ , and  $s^{n+1}$ ) is solved by splitting the whole process by compute intermediate velocities ( $u^*, u^{**}, v^*, v^{**}$ , and  $v^{***}$ ), temperature ( $T^*$ , and  $T^{**}$ ), and smoke concentration ( $s^*$ , and  $s^{**}$ ). The velocity is solved first follow by the temperature and smoke concentration.

### Advection terms of momentum equation

$$\begin{aligned} \frac{u^* - u^n}{\Delta t} &= -\frac{\partial(u^n)^2}{\partial x} - \frac{\partial(u^n v^n)}{\partial y} \\ \frac{v^* - v^n}{\Delta t} &= -\frac{\partial(u^n v^n)}{\partial y} - \frac{\partial(v^n)^2}{\partial y} \end{aligned}$$

Intermediate velocity  $u^*$  and  $v^*$  are solved explicitly by rearranging the advection term of momentum equation as above. This introduces a CFL condition which limits the time step by a constant times the spacial resolution.

### Viscosity terms

$$\begin{aligned} \frac{u^{**} - u^*}{\Delta t} &= \nu \left( \frac{\partial^2 u}{\partial x^2} + \frac{\partial^2 u}{\partial y^2} \right) \\ \frac{v^{**} - v^*}{\Delta t} &= \nu \left( \frac{\partial^2 v}{\partial x^2} + \frac{\partial^2 v}{\partial y^2} \right) \end{aligned}$$

Intermediate velocities ( $u^{**}$  and  $v^{**}$ ) are solved implicitly. Thus, we have to solve two linear systems in each time step.

### Force term

There is a force only in  $y$ -direction. It is solve explicitly.

$$\frac{v^{***} - v^{**}}{\Delta t} = -(\alpha s - \beta \Delta T) g$$

### Pressure term

The fluid is made incompressible by compute the pressure needed to make the divergence of the velocity at next time step to be zero. In the vector notation

$$\frac{\mathbf{u}^{n+1} - \mathbf{u}^{***}}{\Delta t} = -\frac{1}{\rho_0} \nabla p$$

Applying the divergence to both sides yields the linear system

$$\nabla^2 p = \frac{\rho_0}{\Delta t} \nabla \cdot \mathbf{u}^{***}$$

we solve this Poisson's equation to find the pressure and use it to calculate the velocity at next time step  $\mathbf{u}^{n+1}$ . The temperature and smoke concentration are then solved after the velocity is solved.

### Advection terms of advection-diffusion equations

Advection terms are solved explicitly to obtain intermediate temperature  $T^*$  and smoke concentration  $s^*$ .

$$\begin{aligned} \frac{T^* - T^n}{\Delta t} &= -\left(u \frac{\partial T}{\partial x} + v \frac{\partial T}{\partial y}\right) \\ \frac{s^* - s^n}{\Delta t} &= -\left(u \frac{\partial s}{\partial x} + v \frac{\partial s}{\partial y}\right) \end{aligned}$$

### Source terms

Intermediate temperature  $T^{**}$  and smoke concentration  $s^{**}$  are solved explicitly.

$$\begin{aligned} \frac{T^{**} - T^*}{\Delta t} &= r_T (T_{source} - T) \\ \frac{s^{**} - s^*}{\Delta t} &= r_s \end{aligned}$$

### Diffusion terms

$$\begin{aligned} \frac{T^{n+1} - T^{**}}{\Delta t} &= k_T \nabla^2 T \\ \frac{s^{n+1} - s^{**}}{\Delta t} &= k_s \nabla^2 s \end{aligned}$$

Diffusion terms are solved explicitly to obtain temperature and smoke concentration at next time step  $T^{n+1}$  and  $s^{n+1}$

## FINITE DIFFERENCE METHOD

The first derivative of spatial domain is approximated using central finite difference.

$$\frac{\partial u}{\partial x} \approx \frac{u(x + \Delta x) - u(x - \Delta x)}{2\Delta x}$$

The approximation of the second derivative is given by

$$\frac{\partial^2 u}{\partial x^2} \approx \frac{u(x + \Delta x) - 2u(x) + u(x - \Delta x)}{\Delta x^2}$$

In time domain, forward finite difference is used

$$\frac{\partial u}{\partial t} \approx \frac{u(t + \Delta t) - u(t)}{\Delta t}$$

## STAGGERED GRID

Staggered grid is the grid where different variables are stored at different location. The pressure, temperature, and smoke concentration are sampled at the middle of the cells. The fluid velocity in  $x$ -direction  $u$  is sampled at the middle of the vertical cell faces. The fluid velocity in  $y$ -direction  $v$  is sampled at the middle of the horizontal cell faces. It is shown in Figure 2.1. If the value required is not at the location, it is interpolated.

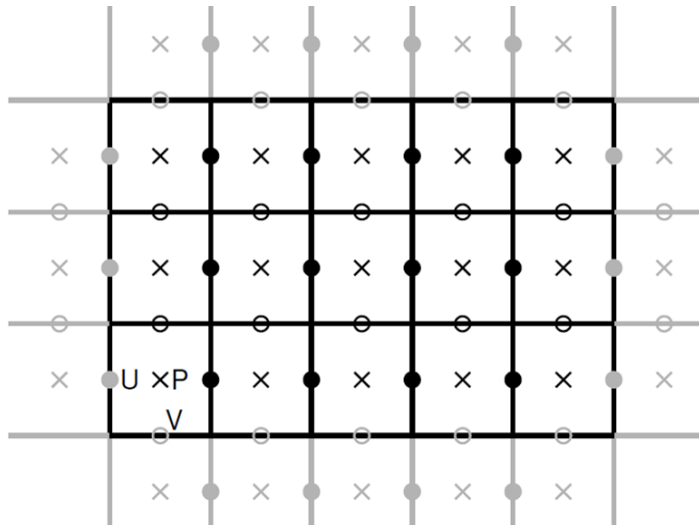


Figure 1: Staggered grid used. x at the middle of the cell is the location of pressure, temperature, and smoke concentration. Black circle the fluid velocity in  $x$ -direction  $u$ . White circle is the location of fluid velocity in  $y$ -direction  $v$ .

## DISCRETIZATION AND INDEX

The rectangular domain is discretized into many square cells.  $L_x$ , the horizontal length of domain, is discretized into  $n_x \Delta x$ . Where  $n_x$  is integer and  $\Delta x$  is grid spacing. Discretization is the same for  $L_y = n_y \Delta y$ . At location  $(i\Delta x, j\Delta y)$ , the variable is indexed by subscript  $(i, j)$ , for example, temperature is indexed  $T_{i,j}$ . The velocity in  $x$ -direction  $u$  is indexed by half integer, e.g.,  $u_{i+1/2,j}$ . In

time domain, the time is discretized into the time step times integer  $t_n = n\Delta t$ . The variable is indexed by superscript, for example, smoke concentration at time  $t_n$  is  $s^n$ .

## BOUNDARY CONDITIONS

Boundary conditions are needed in solving differential equation. In this work, smoke is simulated in a 2D box. The boundary condition for the velocities both in  $x$  and  $y$ -direction is Dirichlet boundary condition, i.e., the velocity is zero at the boundary. The boundary condition for temperature is at the boundary, temperature is equal to ambient temperature. And the boundary condition for smoke is at the boundary, smoke concentration is zero. The boundary condition for pressure is Neumann boundary condition, i.e.,  $\frac{\partial p}{\partial \mathbf{n}} = 0$ . Where  $\mathbf{n}$  is the normal direction to the boundary.

## RESULTS

First, we study the effect of viscosity to the flow pattern at  $T_{amb} = 300$  K,  $T_{source} = 400$  K,  $\alpha = 0.001$ ,  $\beta = 0.0033$ ,  $\rho_0 = 1.289$  km/m<sup>3</sup>,  $k_T = k_s = 0.0001$ ,  $r_T = 0.01$ ,  $r_s = 1$ ,  $\Delta t = \Delta x = \Delta y = 0.01$ . The result is shown in Figure 2 and 3. At high kinematic viscosity ( $\nu > 10^{-4}$ ), the flow is symmetric. The big vortex appears at the top of the flow. When the kinematic viscosity is lower than the critical value  $10^{-4}$ . The symmetry is broken. The small vortex at the top of the flow is observed. Since the system is asymmetric (the source is not placed rightly at the middle of domain but slightly left), this may cause the flow asymmetric. The other reasons are the algorithm of computing and numerical error.

Second, we study the effect of time lag between the releasing of heat and smoke concentration to the flow. The result is shown in Figure 4 and 5

The case of there is no time lag of the releasing of heat and smoke concentration, the big vortex appear at the top of the flow. For the case there is time lag between the releasing of heat and smoke concentration, the vortex is not quite big. The smoke of the latter rises up faster at early time and look sharper than the former. Because the heat released first cause the fluid to flow before the smoke is released.

## CONCLUSION

1. Smoke can be simulated using Navier-Stokes equations and advection-diffusion equations of heat and smoke concentration
2. The flow symmetry is broken when the kinematic viscosity is less than  $10^{-4}$ .
3. Higher kinematic viscosity cause the vortex at the top of the flow bigger. The existence of fluid flow also affect the vortex appeared.

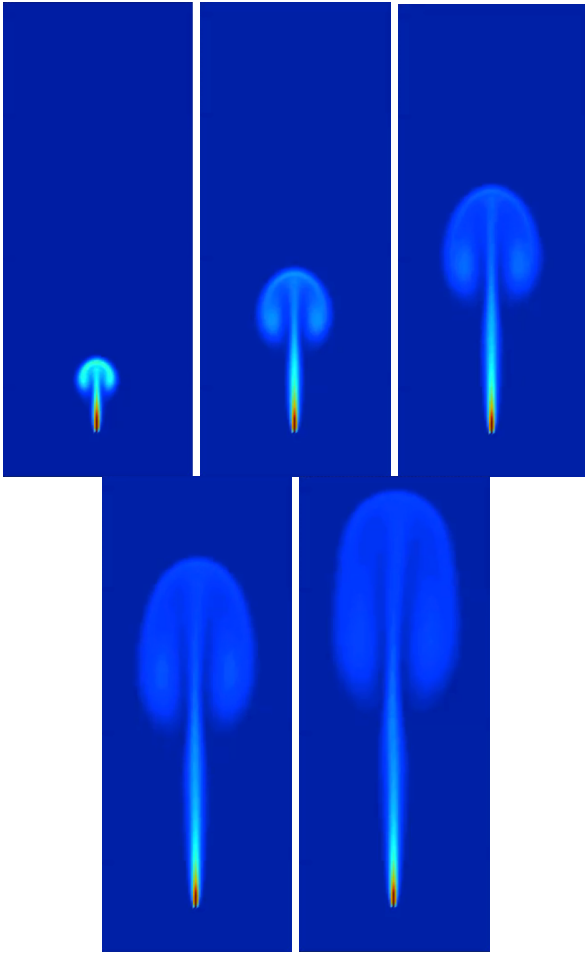


Figure 2: Plot of smoke concentration at different time: 8, 16, 24, 32, and 40 s respectively of fluid with kinematic viscosity  $10^{-3}$

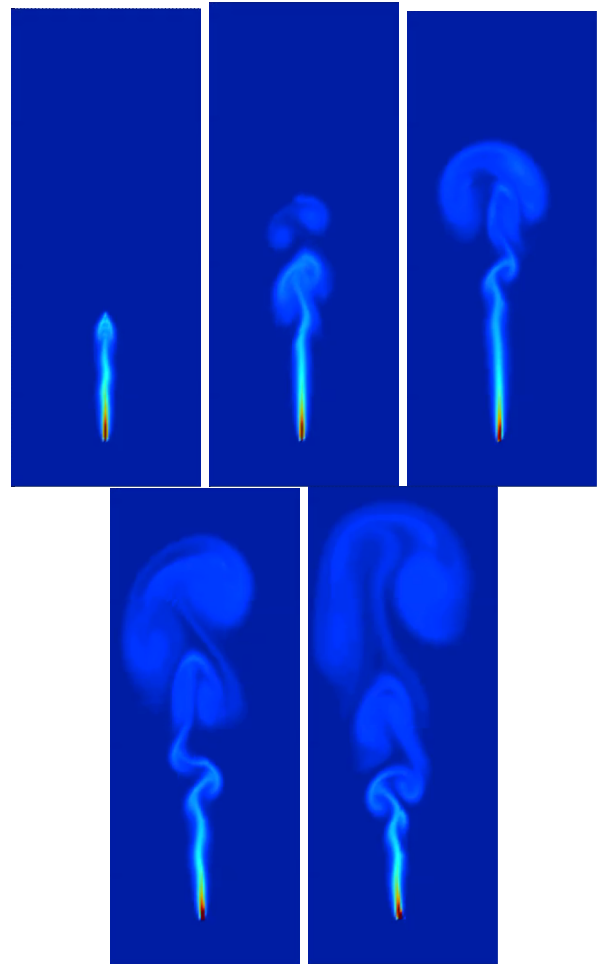


Figure 3: Plot of smoke concentration at different time: 8, 16, 24, 32, and 40 s respectively of fluid with kinematic viscosity  $10^{-5}$

### ACKNOWLEDGMENTS

First of all, I would like to thank my advisor, Dr. Chaiwoot Boonyasiriwat, for all advises and attention. And thank you Development and Promotion of Science and Technology Talents Project (DPST) scholarship for receiving me and all of financial support since the first year. And thank you my family for letting me study science. Thank you Benjamin Seibold for his code used in my project. Finally, thank you my friends for what we have been through.

### REFERENCES

- Bridson, R., 2008, Fluid simulation for computer graphics: A K Peters.
- Fedkiw, R., J. Stam, and H. W. Jensen, 2001, Visual simulation of smoke: In proceedings of the 28th annual conference on Computer graphics and interactive techniques ACM, 15–22.
- Seibold, B., 2008, A compact and fast matlab code solving the incompressible navier-stokes equations on rectangular domains: Massachusetts Institute of Technology.

- Stam, J., 1999, Stable fluids: In Proceedings of SIGGRAPH 99, 121–128.

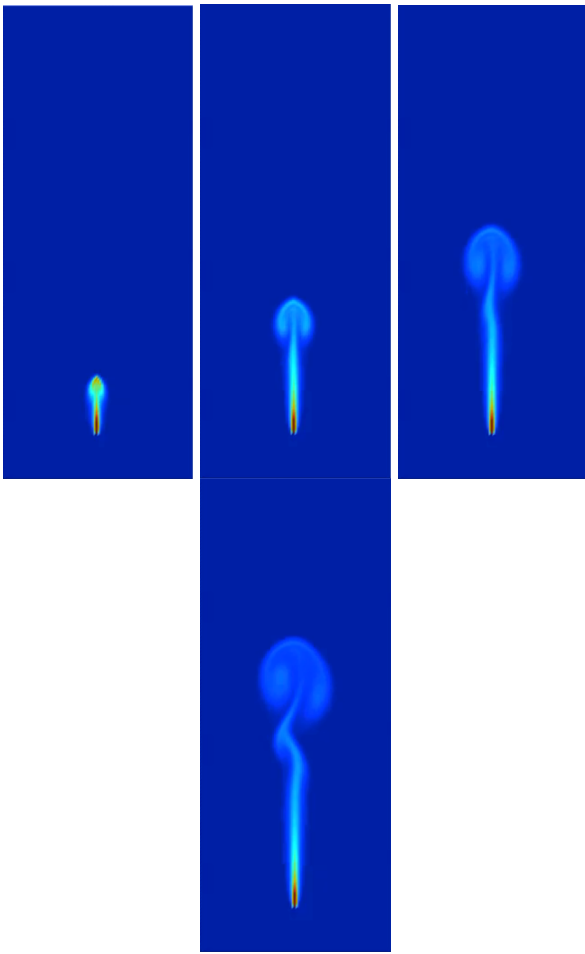


Figure 4: Plot of smoke concentration at different time: 5, 10, 15, and 20 s respectively. Time lag of releasing heat and smoke concentration is 0 s.

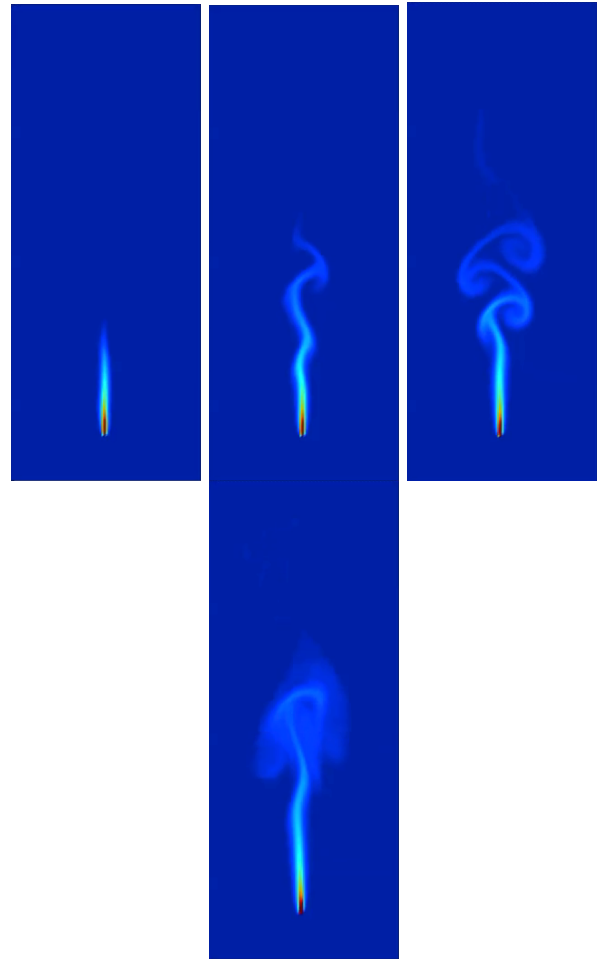


Figure 5: Plot of smoke concentration at different time: 5, 10, 15, and 20 s respectively. Time lag of releasing heat and smoke concentration is 20 s. The heat is released before the smoke is released.



# Simulation of Rayleigh-Taylor Instability in Two Dimensions using Finite Difference Method in MATLAB

Kanisorn Supa and Chaiwoot Boonyasiriwat

## ABSTRACT

The interface between two layers of fluids with different densities can become unstable with the heavier fluid layer is on top of the lighter fluid. This phenomenon is called the Rayleigh-Taylor instability. The heavier fluid is pulled down by gravitational force while the lighter fluid pushes up the heavier fluid. Consequently, fluid advection occur. In this study, the time evolution of interface between two fluids is simulated by solving the Navier-Stokes equations using the finite difference approximation.

## INTRODUCTION

One of the classic example of hydrodynamic instability is the mixing of two fluids that takes place if a heavy initially lies above a lighter one in a gravitational field. This phenomenon is called the Rayleigh-Taylor instability. The heavier fluid is pulled down by gravitational force while the lighter fluid pushes up the heavier fluid. Consequently, fluid advection occur.

In this project, we interest the evolution of interface between two fluids. The instability that occurred by the difference of densities between two fluids cause the shape of interface advection pattern. The shape of spike and bubble will occur in beginning before amplitude of perturbation will grow up quickly and going to turbulent. That is a reason why we rarely see Rayleigh-Taylor instability in from of spike and bubble in real life. So numerical simulation is the one way to study this phenomena easier.

## THEORY OR METHODS

### Governing Equations

The conservation of mass equation for incompressible flow is

$$\nabla \cdot \mathbf{u} = 0 \quad (1)$$

The momentum equation, when the surface tension is neglected, the dynamics viscosity of each fluids are the same, and the one of body force from gravity. Which is

$$\frac{\partial \mathbf{u}}{\partial t} + (\mathbf{u} \cdot \nabla) \mathbf{u} = -\frac{\nabla p}{\rho} + \mathbf{g} + \mu_0 \nabla^2 \mathbf{u} \quad (2)$$

where  $\mathbf{u}$  is partial velocity of fluids,  $p$  is pressure,  $\mu_0$  is dynamics viscosity, and  $\mathbf{g}$  is gravitational force.

### Finite Difference Approximation

Derivative term can approximated by using finite difference approximation, they are central finite difference for the first derivative of spatial domain

$$\frac{\partial f}{\partial x} \approx \frac{f(x + \Delta x) - f(x - \Delta x)}{2\Delta x} \quad (3)$$

central finite difference for the second derivative of spatial domain

$$\frac{\partial^2 f}{\partial x^2} \approx \frac{f(x + \Delta x) - 2f(x) + f(x - \Delta x)}{2\Delta x^2} \quad (4)$$

and forward finite difference for the first derivative of time domain

$$\frac{\partial f}{\partial t} \approx \frac{f(t + \Delta t) - f(t)}{\Delta t} \quad (5)$$

### Staggered Grid

Staggered grid is rectangular domain which each cell compose by any variables at different location. Middle of cell stored by pressure and density, vertical edges stored by velocity of fluid in x direction, and horizontal edges stored

by velocity of fluid in  $y$  direction. Shown in Figure 2.1

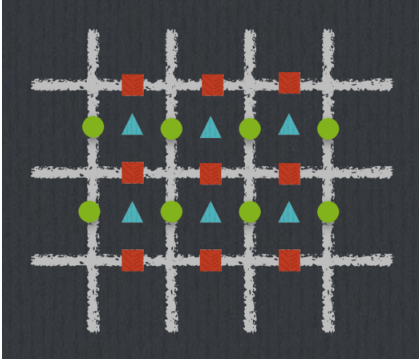


Figure 1: Staggered Grid, triangle is  $p$ , pressure, square rectangle is  $v$ , the velocity in  $y$  direction, and circle is  $u$ , the velocity in  $x$  direction.

## Method of Solving

First, we split the momentum equation(2.2) and calculate the velocity without the pressure term.

$$\frac{\mathbf{u}^* - \mathbf{u}^n}{\Delta t} = -\mathbf{A}^n + \mathbf{g} + \frac{1}{\rho^n} \mathbf{D}^n \quad (6)$$

and then adding the pressure

$$\frac{\mathbf{u}^{n+1} - \mathbf{u}^*}{\Delta t} = -\frac{\nabla_h p}{\rho^n} \quad (7)$$

the superscript  $n$  denotes a variable at current time,  $t$ , and  $n + 1$  denotes a variable at next time step,  $t + \Delta t$ .  $\mathbf{A}$  is the discrete approximation of advection term.  $\mathbf{D}$  is the discrete approximation of diffusion term.  $\mathbf{u}^*$  is temporary velocity.  $\nabla_h$  is a discrete approximation of gradient.

By taking the divergence of equation (2.7) and using equation (2.1) in discrete approximation at the end of time step that is equation (2.8)

$$\nabla_h \cdot \mathbf{u}^{n+1} = 0 \quad (8)$$

we get the Poisson's equation

$$\nabla_h^2 p = \frac{\rho^n}{\Delta t} \nabla_h \cdot \mathbf{u}^* \quad (9)$$

then we solve Poisson's equation of pressure term and find  $\mathbf{u}^{n+1}$ . Finally, we advect the density field by using continuity equation add the term of diffusion, which is

$$\frac{\partial \rho}{\partial t} = -(\nabla \cdot \mathbf{u})\rho + \mu_0 \nabla^2 \rho \quad (10)$$

## Computational Domain

Computational domain is rectangular domain.  $L_x$ , the domain height.  $L_y$ , the domain width. Inside of domain

composed by any cells which size is  $\Delta x \Delta y$ , multiple of spatial grid spacing in  $x$  and  $y$  direction.  $n_x$ , the number of rows of domain width.  $n_y$ , the number of domain height. In addition, we need to add one row of ghost cell outside the domain for help with implementing boundary conditions. So we get the pressure arrays is dimensioned  $p(n_x + 2, n_y + 2)$ . Similarly, we need ghost point for tangential velocity. The velocity arrays dimensioned  $u(n_x + 1, n_y + 2)$  and  $v(n_x + 2, n_y + 1)$ .

## Boundary Conditions

At boundary of domain, we don't have value of velocity. But we can calculate the tangent velocity on the wall by interpolation of the velocity inside the domain and the ghost velocity, which is given by equation (2.11)

$$u_{wall} = \frac{1}{2}(u_{inside} + u_{ghost}) \quad (11)$$

where  $u_{wall}$  is the tangent velocity on the wall,  $u_{inside}$  is the velocity inside the domain, and  $u_{ghost}$  is the ghost velocity.

In this simulation, we use full slip boundary condition which is the tangent velocity on the wall equal to the velocity inside the domain. In the other hand, we set the ghost velocity equal to the velocity inside the domain.

## RESULTS

### Perturbed Interface

We study evolution of interface by adding different initial perturbation at the interface between two fluids. By using domain grid size is 32x96, spatial grid spacing in  $x$  and  $y$  direction are 0.03125, time step is 0.00125, domain height is 3.0, domain width is 1.0, and dynamics viscosity is 0.01. We set the density of heavy fluid is 2.0 and light fluid is 1.0

The interface is advected by following the shape of initial perturbation. From Figure 3.1 and Figure 3.2, the interface are cosine shape which have different spatial wavenumber and growth up of perturbation in time. we can see the growth up rate is depend on spatial wavenumber.

### Unperturbed Interface

We study evolution of interface by no perturbed interface. Similarly, The parameters are the same of perturbed interface case, but the density of heavy fluid is 8.0 and light fluid is 2.0.

In part of unperturbed interface, we expect that interface not change, because Rayleigh-Taylor Instability is unstable fixed point. If no perturbation the interface shouldn't be change. But from Figure 3.4, we can see which have the changing of interface. In this case, we can explain that interface was perturbed by numerical error which occur in each calculation steps.

### CONCLUSION

1. Finite difference approximation can be used to simulate Rayleigh-Taylor instability.
2. Shape of perturbation affect the evolution of interface.
3. Rayleigh-Taylor instability can still occur even though there is no interface perturbation. This could be the effect of numerical error.

### REFERENCES

1. G. Tryggvason. A Front-tracking/Finite-Volume Navier-Stokes Solver for direct Numerical Simulations of Multiphase Flows, 2012
2. A. Prosperetti and G. Tryggvason. Computational Methods for Multiphase Flow. Cambridge University Press, 2007.
3. G. Tryggvason, R. Scardovelli and S. Zaleski. Direct Numerical Simulations of Gas-Liquid Multiphase Flows. Cambridge University Press, 2011

### ACKNOWLEDGMENTS

We would like to thank Gretar Tryggvason for his teaching paper and code.

### REFERENCES

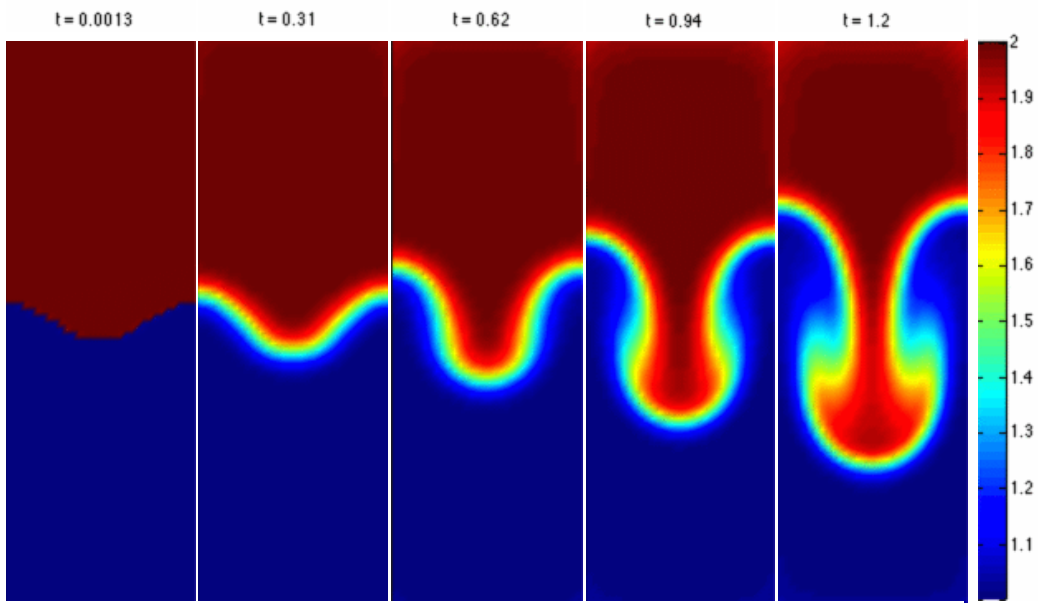


Figure 2: Perturbation is  $(0.1 \times \text{domain width})\cos(2\pi x/\text{domain width})$ , times in sec, and density was shown in different color.

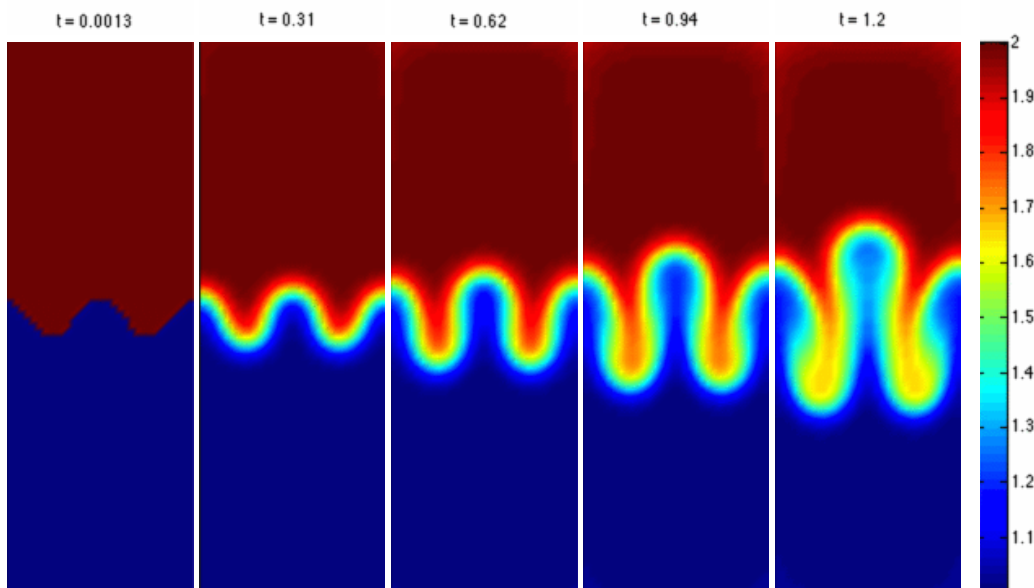


Figure 3: Perturbation is  $(0.1 \times \text{domain width})\cos(4\pi x/\text{domain width})$ , times in sec, and density was shown in different color.

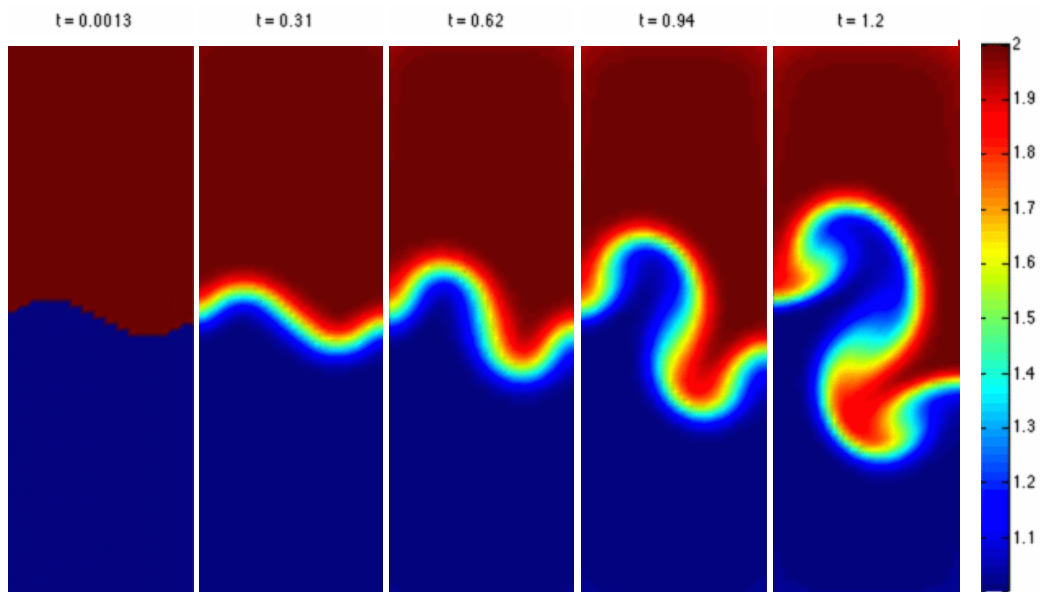


Figure 4: Perturbation is  $(0.1 \times \text{domain width})\sin(2\pi x/\text{domain width})$ , times in sec, and density was shown in different color.

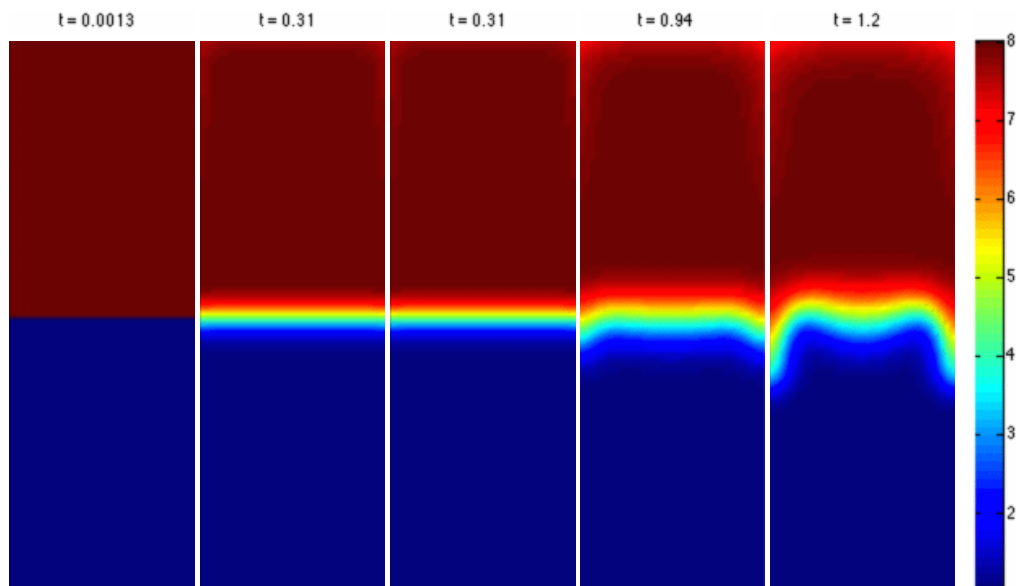


Figure 5: Interface doesn't perturbed, times in sec, and density was shown in different colour.



# A new chaotic circuit based on a single 555 timer IC

Peera Niranartlumphong, Chaiwoot Boonyasiriwat, and Michael A. Allen

## ABSTRACT

Chaotic circuits have been a practical tool for studying chaos for many decades. While some previous works focused on mathematical simplicity or reducing the number of components, this paper proposes a simple circuit in the sense of practical stand point using a well known and widely used component, 555 timer IC, and other common elements such as an inductor and capacitors. The IC produces nonlinearity and acts as a hysteresis switch. Mathematical analysis gives a 4-dimensional system of first order differential equations. Three of dynamical variables have a nonlinearly conditioned function. Simulation and real experiment give solutions of dependent variables such as voltage difference across capacitors and current passing an inductor. Varying concerning parameters, the system exhibits various bifurcations from a fixed point to higher-period limit cycle and eventually to be chaotic in the sense that the trajectories have unmeasurable period and each variable has broad-band spectrum. Reducing the number of components, finding other range of parameters to give an easily observing result, and mathematical proof of chaos are future work.

## INTRODUCTION

The 555 timer IC has been one of the most popular integrated circuit since 1971 among electronics learners and users. It can be used for producing square wave signal with adjustable pulse width and frequency by varying two resistances and one capacitance. Normally, the control port, pin 5, is isolated and protected from the other signal by connecting with another small capacitor and ground in series, otherwise the pulse width of the output signal can be varied if the potential of this pin is not stable Berlin (1979). An interesting problem is how chaotic the system can be if we feedback the processed output signal into this control pin in a simple way.

The oscillating output of 555 timer astable circuit is autonomous or self-oscillated according to the definition by A. Jenkins Jenkins (2013) because it does not have any time dependent source of energy. Although the output signal orbits in a finite range of voltage, it cannot be chaotic because it lacks of a degree of freedom. According to Kenedy (1993), an autonomous continuous chaotic circuit consisting of resistors, capacitors, and inductors must contain (1) at least one nonlinear element, (2) at least one locally active resistor, (3) at least three energy-storage elements. The 555 timer IC plays the role of nonlinear element and we have enough resistors, so we add more energy storage elements, i.e., two capacitors and one inductor. Minimizing the number of components is the further task to do after we can build a chaotic circuit.

There was a chaotic circuit that has some components like the 555 timer IC: comparators (made by op-amps) and a flip-flop: proposed by T. Tsubone and T. Saito in 1998 Tsubone and Saito (1998). These components acts like a hysteresis switch. While the comparators provide non-linearity, the flip-flop exhibits a memory effect Jones et al. (1993). This dependent switch can be described by a delayed-conditioned function of infinitesimally delayed time or a function of another discrete dummy variable  $y$  and other state variables  $x, \dot{x}$ , corresponding to the voltage of the two capacitors in the circuit, at a time. The governing equation of this 3-D dynamical system is a second order differential equation with another dummy variable:

$$\begin{aligned} \ddot{x} - 2\delta\dot{x} + x &= \alpha h(x, \dot{x}, y), \\ h(x, \dot{x}, y) &= \begin{cases} 1, & \text{for } (x, \dot{x}, y) \in D_a \\ -1, & \text{for } (x, \dot{x}, y) \in D_b \end{cases}, \\ D_a &\equiv \{(x, \dot{x}, y) | x > Th, y = 1\} \cup \\ &\quad \{(x, \dot{x}, y) | x < Th, \dot{x} \leq 0, y = 1\} \\ D_b &\equiv \{(x, \dot{x}, y) | x < Th, y = 1\} \cup \\ &\quad \{(x, \dot{x}, y) | x \geq Th, \dot{x} \geq 0, y = 1\} \end{aligned} \quad (1)$$

where  $\delta \in (-1, 1)$ ,  $\alpha \in R$ ,  $Th = 0$  are the system parameters.  $y \in \{-1, 1\}$  is positive and negative if the solution

is in  $D_a$  and  $D_b$ , respectively. It changes its sign just after the state hits boundaries of  $D_a$  or  $D_b$ , so solving this continuous dynamical system in step is inevitable, like solving most of delayed differential equation. By considering the solution at extremum of  $x$ , they can derive a piecewise-linear return map for this system and prove the existence of chaos by showing a positive Lyapunov exponent discretely. Nevertheless, implementation of this circuit is elaborate compared to other simple chaotic circuits Piper (2010).

Instead of making a hysteresis switch using many comparators and a flip-flop, using a single 555 timer IC is simpler in the sense of practical standpoint. The proposed circuit provides three types of attractor, i.e., a stable fixed point, limit cycles, and possibly a chaotic attractor. The limit cycles have the highest frequency component in the range of 5-10 kHz, so the parasitic property of transistors in the IC 555 does not occur making mathematical analysis not too complicated. This circuit is simple to construct and challenging to investigate mathematically.

This proceeding paper is organized as followed. we first describe how to construct the circuit. Then circuit is analysed mathematically and compared with the circuit proposed by Tsubone and Saito (1998) to predict the condition for exhibiting chaos. The results from simulation and real experiment are shown. A summary is given with future work.

### CONSTRUCTION OF CHAOTIC CIRCUIT USING 555 TIMER IC

The proposed circuit consists of 1 timer IC, 3 resistors, 3 capacitors, 1 inductor, and a 9-volt battery as shown in Figure 1. The output port, pin 3, of 555 timer astable circuit connects with RLC damping circuit via the output voltage and the control port, pin 5.

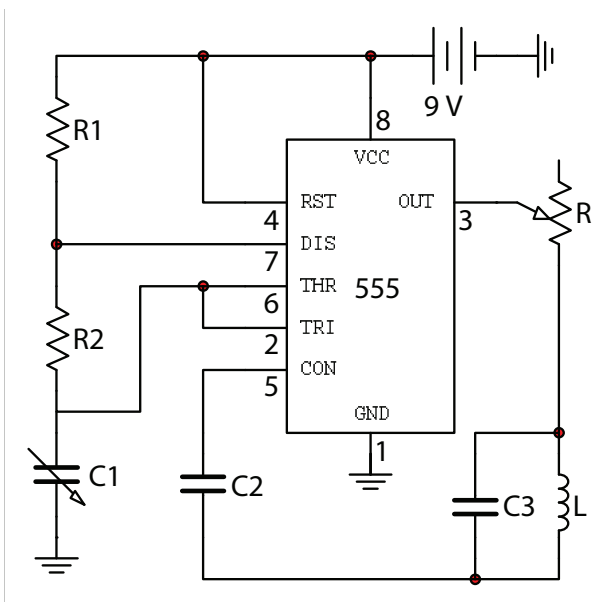


Figure 1: The schematic diagram of the chaotic circuit

where  $V_0$  is the supplying voltage from a 9-volt battery.  $R_1 = 1\text{ k}\Omega \pm 5\%$ ,  $R_2 = 5\text{ M}\Omega \pm 5\%$ , and  $C_1 = 40\text{ pF}$  are, respectively, resistances of two resistors and capacitance of  $100\text{ pF}$  capacitive trimmer, No. 100, in 555 astable circuit. The value of capacitance can be measured by a digital multimeter having tolerance around 3%. We can use other capacitances and resistance as long as this 555 astable circuit produces square wave signal of frequency around  $3.6\text{ kHz}$  with duty cycle  $\approx 50\%$ , e.g.,  $R_1 = 250\ \Omega$ ,  $R_2 = 20\text{ k}\Omega$  and  $C_1 = 10\text{ nF}$ . There are a lot of on-line calculators for computing these values or books providing formula such as Berlin (1979). The resistance of a resistor in 555 timer IC  $r = 4.43\text{ k}\Omega \pm 3\%$  can be determined by directly measuring the resistance across pin 1 and 8 divided by 3.  $C_2$ ,  $C_3$  are the capacitances of buffer capacitors between control pin and another RLC circuit, and the capacitor in RLC parallel bandpass filter, respectively. The coupling capacitor can be composed of compound capacitors in parallel or series to has the value  $C_3$  in the range of  $100 - 250\text{ nF}$ . In this work, we consider  $C_3 = 21\text{ nF}$  and the buffer capacitance  $C_2 = 10\ \mu\text{F}$ . The potentiometer between the 555 timer's output pin and the inductor has its resistance  $R = 0 - 5\text{ k}\Omega$ . The inductor having inductance  $L = 24.8\text{ mH} \pm 3\%$  and series resistance  $r_L = 10.4\ \Omega \pm 3\%$  is made by wrapping enamelled copper wire No. 22 for about 3,200 turns around a PVC tube of outer diameter of 1 inch. The picture of the real circuit is shown in Figure 2.

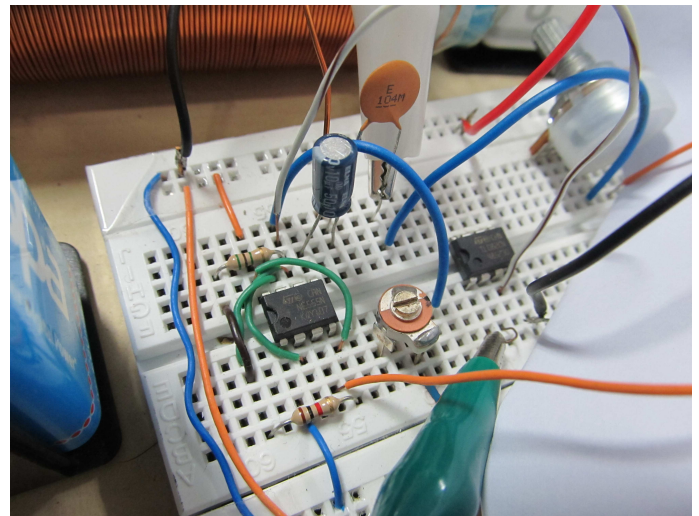


Figure 2: Real circuit with a voltage follower

In order to observe the voltage difference across  $C_1$ , we use an op-amp as a voltage follower to prevent perturbing the 555 astable circuit as we shall see the IC on the right of the Figure 2.

## MATHEMATICAL ANALYSIS OF THE SYSTEM

The system variables  $V_1, V_2, V_3$ , and  $I_L$  correspond to the voltage across three capacitors  $C_1, C_2, C_3$ , and the current passing the inductor, respectively. When  $C_1$  is charging, the current directly passes  $R_1, R_2$  and  $C_1$  from battery to the ground giving  $\dot{V}_1 = \frac{\varepsilon - V_1}{(R_1 + R_2)C_1}$ . After the potential of  $C_1$  reaches the potential of control pin, the node between  $R_1$  and  $R_2$  or discharge port, pin 7, is shorted to the ground, so  $C_1$  is discharging, giving  $\dot{V}_1 = \frac{-V_1}{R_2C_1}$ , until its potential reach 1/2 of that of control pin. We will call the voltage of control pin as ‘‘roof’’ and half of that as ‘‘floor’’. There are three equal resistors  $r$  inside the 555 timer IC connecting the voltage supply port, pin 8, to the ground Berlin (1979). The control port connects to the node between the first and second resistors inside the IC. By Kirchhoff’s voltage law, we get

$$\dot{V}_2 = \frac{V_0/3 - V_2 - V_3}{(R + 2r/3)C_2}, \dot{V}_3 = \left( \frac{V_0/3 - V_2 - V_3}{(R + 2r/3)} + I_L \right) \frac{1}{C_3}$$

for charging period of  $C_1$  and

$$\dot{V}_2 = \frac{2V_0/3 - V_2 - V_3}{(R + 2r/3)C_2}, \dot{V}_3 = \left( \frac{2V_0/3 - V_2 - V_3}{(R + 2r/3)} + I_L \right) \frac{1}{C_3}$$

for charging period of  $C_1$ . Dynamic of current passing the inductor is found by Faraday’s law of induction:  $\dot{I}_L = \frac{-V_3 - I_L r L}{L}$ . The governing equations are then given by

$$\begin{aligned} \dot{w} &= \begin{cases} a(1-w), & \text{charge} \\ -bw, & \text{discharge} \end{cases} \\ \dot{x} &= \begin{cases} cd(1/3 - x - y), & \text{charge} \\ cd(2/3 - x - y), & \text{discharge} \end{cases} \\ \dot{y} &= \begin{cases} e(c(1/3 - x - y) + z), & \text{charge} \\ e(c(2/3 - x - y) + z), & \text{discharge} \end{cases} \\ \dot{z} &= -fy - gz, \end{aligned} \quad (2)$$

where the variables  $V_1/V_0, V_2/V_0, V_3/V_0, I_L$  are replaced by  $w, x, y, z$  and the parameters  $\frac{1}{(R_1 + R_2)C_1}, \frac{1}{R_2C_1}, \frac{1}{R + 2r/3}, \frac{1}{C_2}, \frac{1}{C_3}, V_1/L, rL/L$  are replaced by  $a, b, c, d, e, f, g$ , respectively. The charging condition occurs, at time  $t$ , when

$$\left( w(t) < v_{\uparrow}(T) \wedge \lim_{T \rightarrow t^-} \dot{w}(T) > 0 \right) \vee w(t) \leq v_{\downarrow}(T)/2,$$

and the discharging condition occurs when

$$\left( w(t) > v_{\downarrow}(T)/2 \wedge \lim_{T \rightarrow t^-} \dot{w}(T) < 0 \right) \vee w(t) \geq v_{\uparrow}(T),$$

where

$$v = \begin{cases} v_{\uparrow} = 1 - x - y, & \text{charge} \\ v_{\downarrow} = \frac{2}{3} - \frac{2rc}{3}(2/3 - x - y), & \text{discharge} \end{cases}. \quad (3)$$

The nonlinear effect in (2) comes from the conditions of charging and discharging which depend on the comparison between the states of  $w, x$ , and  $y$  at infinitesimally earlier and current time. It has a delayed effect because of an infinitesimally delay time, but the dependence is only from the sign of comparison. Despite the conditions, there is no delayed term in the governing equations. Furthermore, in the first equation,  $w$  does not depend on other state variables directly. It connects to the others by the conditions of charge and discharge.

The equilibrium or fixed points are where the system does not change its state variable. We can analytically predict them by setting all of  $\dot{w}, \dot{x}, \dot{y}, \dot{z}$  to zero and equate equations. We get the fixed points at  $(W_{1,2}, X_{1,2}, Y_{1,2}, Z_{1,2}) = (1, 1/3, 0, 0)$  and  $(0, 2/3, 0, 0)$  for charging and discharging, respectively. Because of linearity, the system (2) can be written in the matrix form:

$$\begin{pmatrix} \dot{w} \\ \dot{x} \\ \dot{y} \\ \dot{z} \end{pmatrix} = \begin{cases} - \begin{pmatrix} a & 0 & 0 & 0 \\ 0 & cd & cd & 0 \\ 0 & ce & ce & -e \\ 0 & f & 0 & g \end{pmatrix} \begin{pmatrix} w \\ x \\ y \\ z \end{pmatrix} + \begin{pmatrix} 1 \\ 1/3 \\ 1/3 \\ 0 \end{pmatrix}, & \text{charge} \\ - \begin{pmatrix} b & 0 & 0 & 0 \\ 0 & cd & cd & 0 \\ 0 & ce & ce & -e \\ 0 & f & 0 & g \end{pmatrix} \begin{pmatrix} w \\ x \\ y \\ z \end{pmatrix} + \begin{pmatrix} 0 \\ 2/3 \\ 2/3 \\ 0 \end{pmatrix}, & \text{discharge} \end{cases} \quad (4)$$

The solution near fixed points is

$$\delta \vec{s} = \sum_{i=1}^4 A_i e^{\lambda_i t} \vec{e}_i,$$

where  $\delta \vec{s}$  is the position vector from a fixed point,  $A_i$ ’s are constant from initial conditions,  $\lambda_i$  and  $\vec{e}_i$  are the  $i^{th}$  eigenvalue and eigenvector, respectively.

It is difficult to find all eigenvalues without substituting the parameters, but we could find, at least, the first one,  $\lambda_1 = -a$  or  $-b$  for respectively charge and discharge in which the trajectory is attracted in this corresponding eigenvector axis. Three remaining eigenvalues are the roots of the cubic equation obtained by equating to zero the characteristic polynomial can be 1 real and 2 complex conjugate numbers because a cubic function must at least cross the x-axis once. Consequently, a trajectory near a fixed point could be attracted or repelled exponentially in one direction and moves spirally into a fixed point in a plane.

In the last decade, chaotic systems written as high-order

differential equations (DE) in one dimension have come into fashion Piper (2010). The system (2) can be written in the form (1) as proposed in Tsubone and Saito (1998) because each derivative of a variable with different order is independent of each other. The simplest way to transform a high-order differential equations into a system of first-order differential equations is to substitute the first to highest order derivative by new distinct variables. The consequently linearly independent variable can be superposed to give a new system with new basis having the form as we used in (2). So, in principle, our system can be expressed in the form of 4<sup>th</sup> order differential equations. The remaining point to compare is to write the condition of charge and discharge by the method of new dummy variable in (1). Let  $p = 1$  and  $p = -1$ , respectively, correspond to  $\lim_{T \rightarrow t^-} \dot{w} > 0$  and discharge or  $\lim_{T \rightarrow t^-} \dot{w} < 0$ . The differences between charge and discharge condition are constant terms and coefficient of  $w$  in the system (2), so we can combine each conditioned equations into an equation with terms of  $(1+h)/2$ , where  $h = h(w, x, y, p)$ :

$$\begin{aligned} h(w, x, y, p) &= \begin{cases} 1, & \text{for } (w, x, y, p) \in D_a \\ -1, & \text{for } (w, x, y, p) \in D_b \end{cases} \\ D_a &\equiv \{(w, x, y, p) | w < v_{\uparrow}(x, y), y = 1\} \cup \\ &\quad \{(w, x, y, p) | w \leq v_{\downarrow}(x, y)/2\} \\ D_b &\equiv \{(w, x, y, p) | w > v_{\downarrow}(x, y)/2, y = 1\} \cup \\ &\quad \{(w, x, y, p) | w \geq v_{\uparrow}(x, y)\} \end{aligned}$$

Although this is a 4-dimensional system, the first variable,  $w$ , almost does not interact with the other dependent variables. It is just the charging and discharging exponential function of R-C circuit without distortion. Increasing the capacitance  $C_1$  enhances the time rate of change of  $V_1$ , while  $R_1$  and  $R_2$  control the ratio of charge and discharge time. Consequently, higher  $C_1$  allows each damped oscillation to sustain itself longer before switching. The capacitor  $C_3$  and the inductor  $L$  produce an impedance oscillation: exchange of potential energy between a capacitor and an inductor back and forth. Both  $C_3$  and  $L$  dilate the period of oscillation, but  $C_3$  decreases the amplitude, while  $L$  increases it. The resistor  $R$ , of course, consumes energy and attenuates the oscillation. The capacitor  $C_2$  acts as a buffer of overall signal, the last three variables. It is charged and discharged as the output voltage is high or low, but also oscillates according to the impedance oscillation. The higher capacitance  $C_2$ , the lower amplitude of influenced oscillation is. The resultant signal  $v$  is the superposition of voltage difference across each element.

For convenience, we consider 2 linearly independent variables  $w$  and  $v$  for adjusting parameters because the former relates to the other only via the condition of  $v$  that is a combination of damped oscillation and exponential function. As the charging  $w$  is equal to  $v$  curve, the condition changes to discharge. On the other hand, it changes to charging again when  $w$  hits on  $v$  while discharging. The sudden change stimulates a new oscillation which, later on, behaves like a 3-dimensional system with a new set

of initial conditions as shown on the right side of Figure 5. Our assumption is that the charge/discharge function of  $w$  should be similar to the envelope of  $v$  to make the intersecting points be in the vicinity of various troughs of  $v_{\uparrow}$  and crests of  $v_{\downarrow}/2$ .

## SIMULATION AND REAL EXPERIMENT

After varying parameters in the simulation using a virtual circuit software, NI Multisim 10, we found an appropriate range of  $R, L, C_{1,2,3}$  to produce bifurcations and chaos. These parameters are  $R_1 = 28.9 \text{ k}\Omega, R_2 = 57.7 \text{ k}\Omega, C_1 = 1 \text{ nF}, R = 6 \text{ }\Omega, L = 60 \text{ mH}, C_3 = 50 \text{ nF}, C_2 = 5 \text{ }\mu\text{F}$  with a 9V-battery. The results of the simulation are shown in Figure 3.

The orbit experiences period 1 limit cycle when  $R$  is in the range of  $800 \text{ }\Omega - 5 \text{ k}\Omega$ , then period doubling bifurcates once around  $R = 700 \text{ }\Omega$  and enters another basin of attraction when  $R$  is around  $600 \text{ }\Omega$ . When  $R$  is below  $455 \text{ }\Omega$ , the two basins merge together letting the trajectory passes two local maxima of  $v$ . Decreasing  $R$ , the number of events that charging curve  $V_1$  passes the crest of damped oscillation  $v$  compared to that of another event that charging curve  $V_1$  does not passes is higher. The smaller loops split into 3 bands. Finally, the attractor ends up with period 3 limit cycle for  $R < 150 \text{ }\Omega$ .

We realize that NI Multisim 10 does not provide an accurate calculation for the 555 timer IC. It treats the IC as a black box giving the output voltage from a given input signal from pins 5, but does not take the resistance of voltage divider inside the IC into account. So we reconstruct the IC according to real one we have by 3 resistors  $r = 4.43 \text{ k}\Omega$ , 2 comparators, 1 SR flip-flop, 1 controlled switch instead of a transistor to avoid continuous response as illustrated in Figure .

The internal resistors of the IC cause damped oscillation to decay faster and to have higher frequency and smaller amplitude. After briefly sweeping our parameters, we found period doubling or adding bifurcation as shown in Figure 3.

In real circuit, we set the parameters according to the mentioned values in Section 2. The circuit exhibits period doubling bifurcations back and forth frequently as we decrease the resistance  $R$  from  $5 \text{ k}\Omega$  to  $40 \text{ }\Omega$  because  $V_1$  changes the point between adjacent pulse of damped oscillation. Then the period suddenly grows up to infinity (Figure 6).

According to the spectrum analysis, the limit cycle is period 1 at  $R = 3.67 \text{ k}\Omega$ , period 2 at  $R = 3.00 \text{ k}\Omega$ , period 1 at  $R = 2.55 \text{ k}\Omega$ , period 2 at  $R = 1.65 \text{ k}\Omega$ , period 1 at  $R = 1.40 \text{ k}\Omega$ , period 2 at  $R = 1.19 \text{ k}\Omega$ , period 1 at  $R = 1.02 \text{ k}\Omega$ , and so on with smaller intervals of  $R$ : Figures (6a-6e). Then it suddenly bifurcates many times to chaos at  $R = 0.41 \text{ k}\Omega$ , exhibits intermittency at  $R = 89 \text{ }\Omega$ , and becomes chaotic again through the lowest series resistance we can have  $R = 16.3 \text{ }\Omega$  (Figures 7f-7h).

SUMMARY

For the first time, the well known and widely used 555 timer IC was combined with an RLC damping circuit to create a new chaotic circuit. The corrected simulation result and the result from experiment was more damped than the former result shown in Figure 3 because there are 3 more resistors in the 555 time IC, so the real results are in another range of period. New corrected circuit had been simulated both in Matlab and NI Multisim 10, but the accurate parameters of bifurcations was not found yet. However, after correcting the simulation, the result was consistent with real experiment. We found bifurcations route to increase period, intermittency and broad-band spectrum signal.

FUTURE WORK

There are 8 essential tasks to be accomplished in the future.

1. Modify the simulation to be more realistic.
2. Verify that the simulation results from Matlab and NI Multisim are consistent or find the reason if they are not.
3. Determine the parameters for exhibiting bifurcation accurately both in real experiment and simulation.
4. Try to vary other parameters such as  $L$ ,  $R_1$ ,  $R_2$ ,  $C_1$ ,  $C_2$ ,  $C_3$  and observe bifurcations.
5. Find chaos in other range of parameters such that the mean frequency of oscillation can be observed by eyes if an LED is applied and flashed.
6. Reduce the number of energy storage element,  $L$ ,  $C$ , to make the system simpler.
7. If the reduced system has only two energy storage element, solve it analytically and transform into a discrete map as in Tsubone and Saito (1998).
8. Mathematically guarantee the chaos by showing that the system has a positive Lyapunov exponent.

REFERENCES

Berlin, H. M., 1979, 555 timer applications sourcebook with experiments: Sams Publishing.  
 Jenkins, A., 2013, Self-oscillation: Physics Reports, **525**, no. 2, 167222.  
 Jones, G. R., M. A. Laughton, and M. G. Say, 1993, Electrical engineer's reference book: Butterworth-Heinemann.  
 Kenedy, M. P., 1993, Three steps to chaos part II: a chuas circuit primer: IEEE Transactions on Circuit and System I, **40**, no. 10, 1057-7122.  
 Piper, J. R., 2010, Simple autonomous chaotic circuits: IEEE Transactions on Circuit and System II, Express Briefs, **57**, no. 9, 730-734.

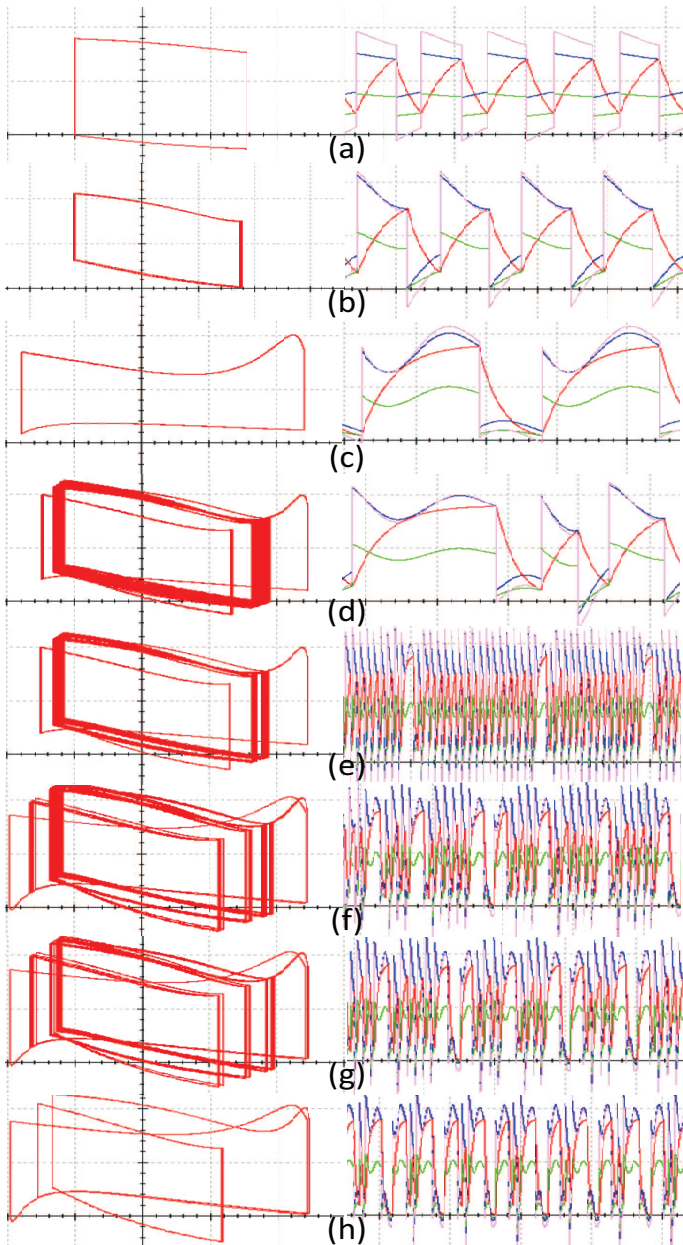


Figure 3: X-Y plot and time series of  $V_1$  (red) and  $v$  (blue) for (a-d)  $R = 5\text{ k}\Omega$ ,  $700\ \Omega$ ,  $600\ \Omega$ ,  $455\ \Omega$ ,  $2:2\ \text{V/div}$  (left),  $200\ \text{s/div}$ - $5\ \text{V/div}$  (right), and (e-h)  $R = 400\ \Omega$ ,  $200\ \Omega$ ,  $175\ \Omega$ ,  $100\ \Omega$ ,  $2:2\ \text{V/div}$  (left),  $2\ \text{ms/div}$ - $5\ \text{V/div}$  (right.)

ACKNOWLEDGEMENT

I would like to express my appreciation to all those who provided me the possibility to complete this report. I would like to express my special thanks of gratitude to my teacher, Aj.Chaiwat Laowattanakul, who taught me electronics and suggested me how to observed the signal from the circuit with less perturbing and less noise. I also acknowledge Dr.Ratchapak Chitaree, who gave the permission to use all required equipment and the necessary materials to complete the task.

Tsubone, T. and T. Saito, 1998, Stabilizing and destabilizing control for a piecewise-linear circuit: *IEEE Transactions on Circuits and System I, Fundamental Theory and Applications*, **45**, no. 2, 172–177.

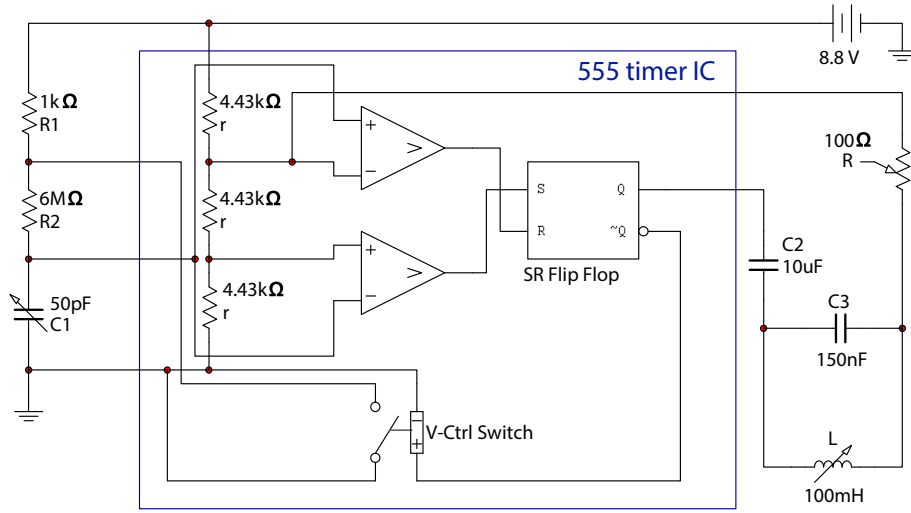


Figure 4: The schematic diagram showing corrected circuit component for simulation

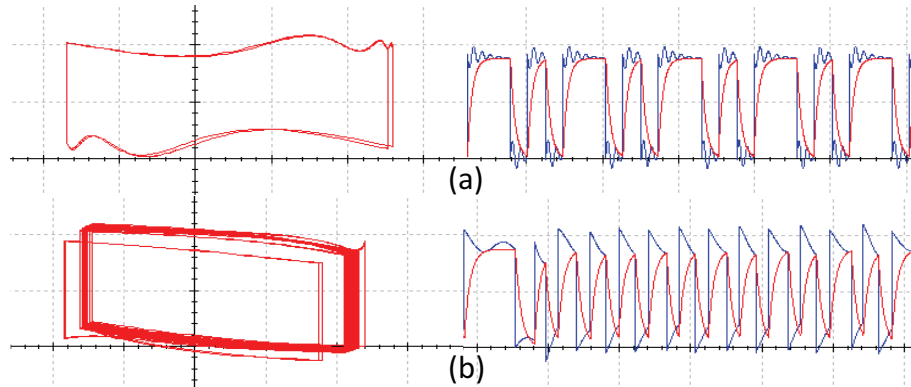


Figure 5: X-Y plot , 2:5 V/div (left), and time series of  $V_1$  (red) and  $v$  (blue), 2ms/div-5V/div (right), for  $R = 0 \Omega$ , (a) period 2:  $C_1 = 27 \text{ pF}$ ,  $C_2 = 10 \mu\text{F}$ ,  $C_3 = 150 \text{ nF}$ ,  $L = 50 \text{ mH}$ , and (b) period 64:  $C_1 = 50 \text{ pF}$ ,  $C_2 = 1 \mu\text{F}$ ,  $C_3 = 360 \text{ nF}$ ,  $L = 158 \text{ mH}$ .

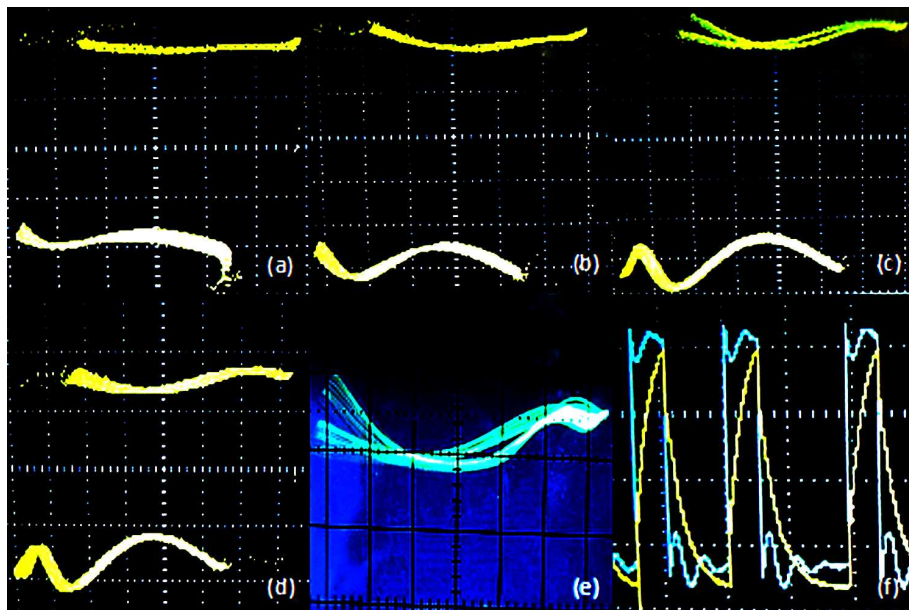


Figure 6: X-Y plot of  $V_1$  and  $v$  for period 1, period 2, chaotic, and intermittent limit cycle attractors (a-d). (e) zooms to a part of chaotic chaotic attractor. (f) shows the time series of  $V_1$  (yellow) and  $v$  (blue), 1ms/div, 2V/div

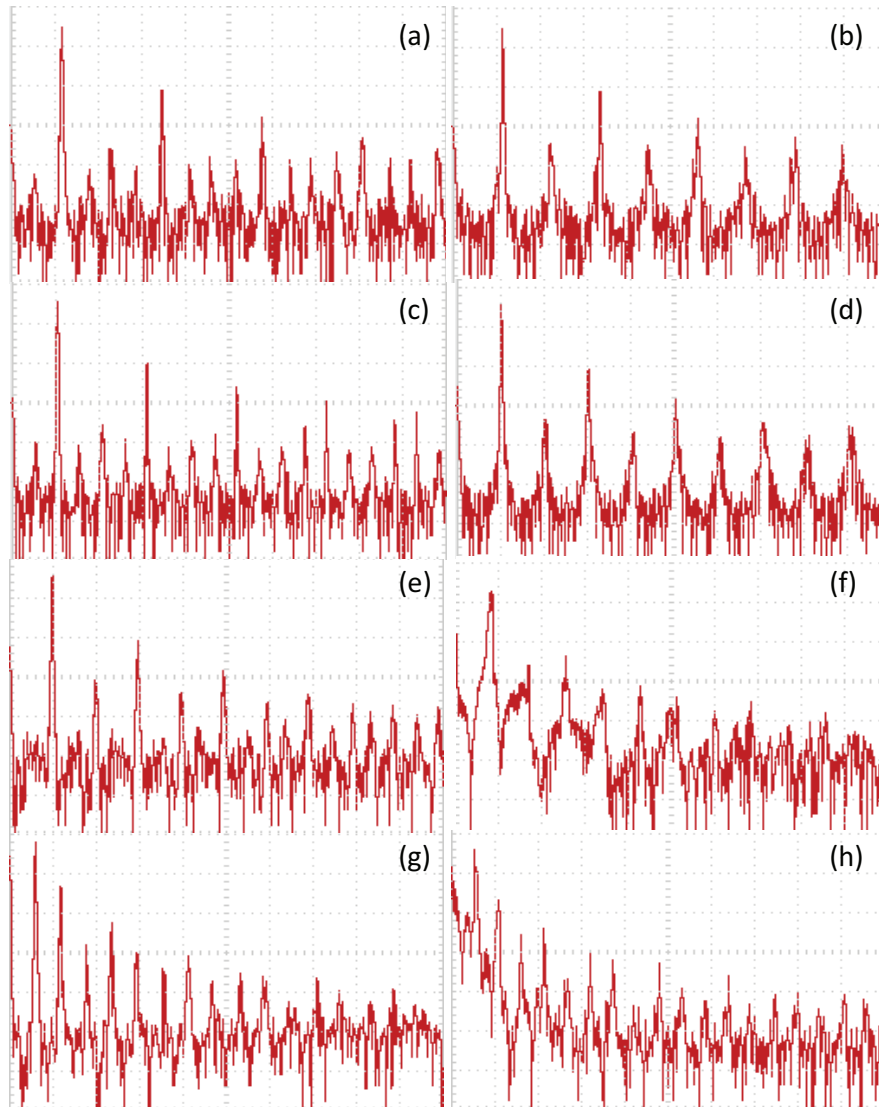


Figure 7: spectrum of  $V_1$  time series,  $1.25 \text{ kHz/div}$ ,  $10 \text{ dB/div}$ . (a-e) represent period 2, 1, 2, 1, 2 limit cycle at  $R = 3.00 \text{ k}\Omega$ ,  $2.55 \text{ k}\Omega$ ,  $1.65 \text{ k}\Omega$ ,  $1.40 \text{ k}\Omega$ ,  $1.19 \text{ k}\Omega$ ,  $1.02 \text{ k}\Omega$ . (f,g,h) are of chaos at  $R = 0.41 \text{ k}\Omega$ , intermittency at  $R = 89 \text{ }\Omega$ , and chaotic attractor at  $R = 16.3 \text{ }\Omega$



# Mathematical Modeling of Magnetic Pendulum

Harirak Intarak and Chaiwoot Boonyasiriwat

## ABSTRACT

In this work, we study the dynamics of a pendulum with a small magnet attached at the end of the pendulum arm. The magnet interacts with a fluctuating magnetic field generated by an electromagnet with an alternative current passing through. The magnetic field acts as the driving force so the system can be described as a damped, forced oscillation. Unlike conventional forced oscillation, the magnetic pendulum can exhibit large-amplitude undamped oscillations at driving frequencies higher than the resonance frequency. The key difference is that in the magnetic pendulum system, the driving force only acts at low angular displacement. Experimental results show that the undamped oscillation amplitude is in the range of 10-20 Hz and oscillation amplitude is in the range of 12-24 degrees. Numerical results from our mathematical model can simulate undamped oscillation but are not yet in agreement with the experimental results. The further model development is required.

## INTRODUCTION

There are various types of magnetic pendulum. The main idea of the magnetic pendulum is that it is the pendulum with magnet at the end of the arm. And there is the force interacted with the pendulum which is the magnetic force that come from other magnet or the interaction with the magnetic field generated by the electromagnet from Biot-Savart's law described that when the electric current passing through the electromagnet, it will generate the magnetic field. In this case, the force act on pendulum is due to the interaction with the magnetic field from the electromagnet generated by alternative current (AC). We called this oscillation is driven forced oscillation.

Speaking of forced pendulum, this magnetic pendulum is difference. Because of the driving force only acts at low

angular displacement, the large-amplitude undamped oscillation occurs not only at the resonance frequency but also at the certain frequencies. This is the key of undamped behavior.

Damgov (2000) thought that the force in interaction zone can be represented by boxcar function which equal  $F$  in the interval  $\pm \frac{d}{2}$  and zero otherwise, while  $F$  is the force coefficient. But in fact, it shouldn't be boxcar function because the magnetic force is the inverse square force. It just like the electric force  $F = kq_1q_2/r^2$  but it is not charge it is magnetic moment,  $F = km_1m_2/r^2$ . It should represent by other function, in this study show that it represented by gaussian function. The advantage of using gaussian function is it can represent the slow change of the force when it away from the center and gently fade away as force depend on  $1/r^2$ .

We would like to introduce the apparatus in this experiment. As shown in Figure 1, there are function generator on the left side that creates sine wave current. The right hand side is amplifier that amplifies the signal from function generator through the output at center that is electromagnet to create magnetic field. The pendulum arm in this case is the physical pendulum. This apparatus based on Tennenbeum (2005), but the pendulum in this case is the physical pendulum.

In this report, it will cover the concept of being undamped oscillation, how we study the pendulum, the results from both experiment and numerical, and the problem with experiment.

## THEORY AND METHODS

This section contains three parts, first is type of oscillation, the second is the concept in which the pendulum stay undamped, and the last one is how we study the pendulum, it also cover the model that we study and how we find it.

I will introduce the three types of oscillation which are simple harmonic oscillation, damped oscillation, and driven forced oscillation plus this magnetic pendulum os-

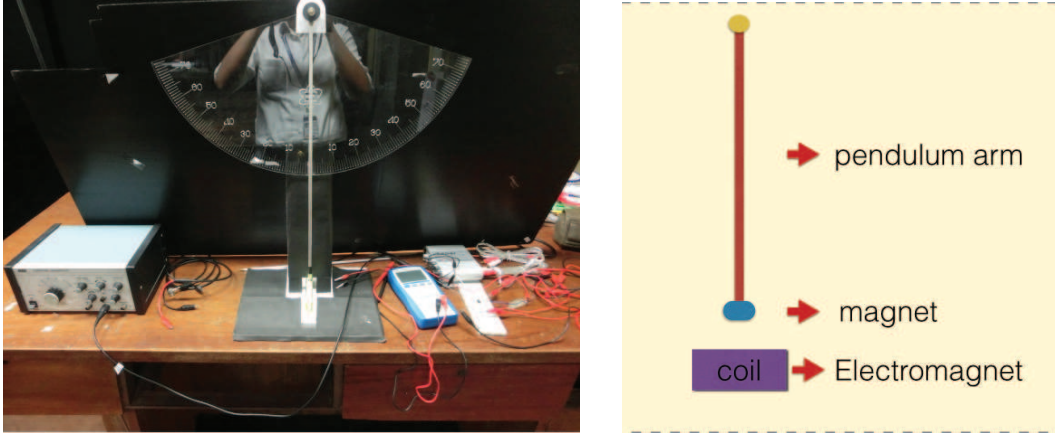


Figure 1: The apparatus in this experiment

cillation. First of all, we need to introduce the concept of oscillation. In ideal system, there are two force on the system that are restoring force and force from inertia. The restoring force is the force that bring the system to the equilibrium and inertia is the resistance of any physical object to any change in its state of motion.

In case of simple harmonic oscillation, the restoring force is propotional to displacement, such as angular displacement. The amplitude of oscillation is stay the same, since there is no force that lose energy from the system. We can write the equation of motion from Newton's law of motion in angular part

$$\tau_{net} = I\alpha \quad (1)$$

$$-mgl \sin \theta = I\ddot{\theta} \quad (2)$$

Since angle in simple harmonic oscillation isn't large, we can approximate  $\sin \theta \approx \theta$ . And the moment of inertia of light pendulum is  $I = ml^2$ . Therefore the equation of motion in simple harmonic oscillation is

$$\ddot{\theta} + \frac{g}{l}\theta = 0 \quad (3)$$

$$\ddot{\theta} + \omega_0^2\theta = 0 \quad (4)$$

Which we call  $\omega_0$  is the natural frequency of the system which equal to  $\sqrt{g/l}$ . We can find the exact solution is

$$\theta(t) = A \cos(\omega_0 t - \phi) \quad (5)$$

While  $A$  is the amplitude of the oscillation at  $t = 0$  and  $\phi$  is initial phase. The graph relation between time and angular displacement as seen in Figure 2

The figure 2 shows that the in simple harmonic oscillation, it oscillate at frequency equal to natural frequency  $\sqrt{g/l}$  with the constant amplitude.

When the system has the force that lose energy from system, we call this oscillation is damped oscillation, such as drag force, friction force. The damping force that add to the system depends on velocity, therefore we can ap-

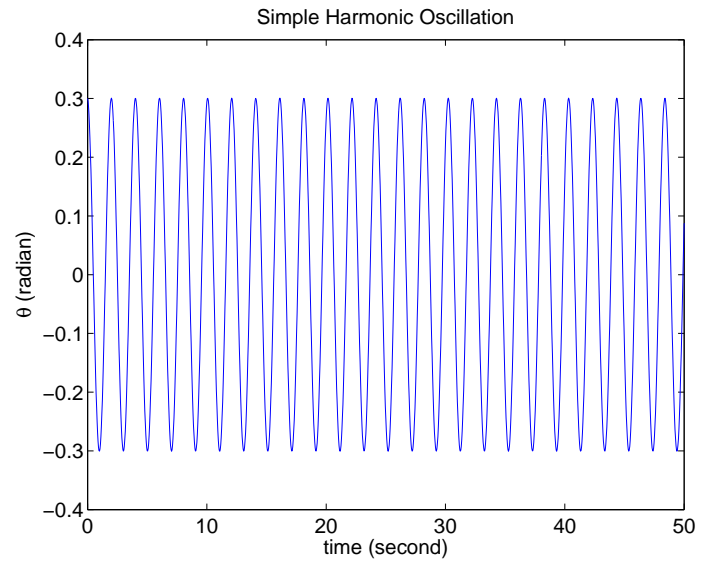


Figure 2: The function of angular displacement respect to time of simple harmonics oscillation

proximate using only linear term as  $F_d = b\omega$ , while  $b$  is drag coefficient and  $\omega$  is angular velocity. The equation of motion becomes

$$-mgl\theta - bl^2\dot{\theta} = I\ddot{\theta} \quad (6)$$

$$-\frac{g}{l}\theta - \frac{b}{m}\dot{\theta} = \ddot{\theta} \quad (7)$$

Define  $\omega_0 = \sqrt{g/l}$  and  $a = b/m$  then the equation of motion becomes

$$\ddot{\theta} + \omega_0^2\theta + a\dot{\theta} = 0 \quad (8)$$

The exact solution of this equation is

$$\theta(t) = Ae^{-(a/2)t} \cos(\omega_1 t - \phi) \quad (9)$$

While  $A$  is the amplitude of the oscillation at  $t = 0$  and  $a$

is the drag coefficient and  $\omega_1 = \sqrt{\omega_0^2 - b^2/4}$  and  $\phi$  is initial phase. The graph relation between time and angular displacement as seen in Figure 3

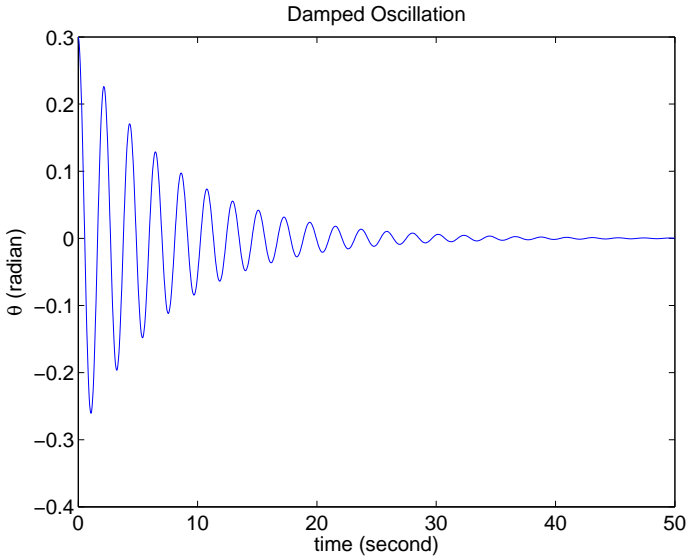


Figure 3: The function of angular displacement respect to time of damped oscillation

As you can see in Figure 3, the amplitude of the oscillation gradually decrease until it is zero. As in the solution equation 9, the exponential term is the decreasing term that make the oscillation decreased until the time the amplitude is zero.

And when we have external force acts on system, we call this oscillation is forced oscillation. Such as sinusoidal force :  $F_{driv}(t) = F \sin(\omega_f t + \phi_f)$ , while  $F$  is the amplitude of driving force. The equation of motion becomes

$$\ddot{\theta} + \omega_0^2 \theta + a\dot{\theta} = F \sin(\omega_f t + \phi_f) \tag{10}$$

There is a exact solution comes from the homogeneous solution plus only one particular solution as

$$\theta(t) = Ae^{-(a/2)t} \cos(\omega_1 t - \phi) + B \cos(\omega_f t - \delta)$$

While  $A$  is the amplitude of the oscillation at  $t = 0$ ,  $\phi$  is initial phase, both of it come from initial condition. And  $B$  and  $\delta$  can be calculated from

$$B = \sqrt{\frac{F^2}{(\omega_0^2 - \omega_f^2)^2 + a^2 \omega_f^2}}$$

$$\delta = \arctan\left(\frac{a\omega_f}{\omega_0^2 - \omega_f^2}\right)$$

We can see that at the first term it is the transient once in long time the first term is decay and the second term is dominated. The oscillation will oscillate at frequency  $\omega_f$  with unchanging amplitude for as long as the driving force is maintained. But this solution isn't the

general solution, therefore this solution can't predict motion at all time, this particular solution can describe the oscillation at long time but not at transient time. Therefore there should be more particular solutions that corresponding to homogeneous equation add to be the general solution.

The graph relation between time and angular displacement as seen in Figure 4

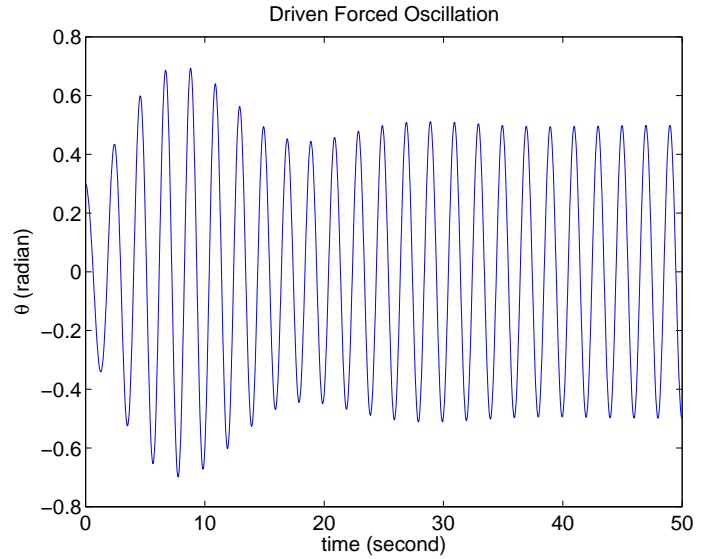


Figure 4: The function of angular displacement respect to time of driven forced oscillation

As shown in Figure 4, the amplitude at long time is constant and oscillate with some certain frequency. As in equation 11, if the time is long, the first term will disappear and second term is dominated.

If we talk about large amplitude of the oscillation at long time, we will see that if  $\omega_f$  is equal to  $\omega_0$ , the amplitude of the oscillation at long time will be  $B = F/(a\omega_f)$ . If we plot graph with frequency to square amplitude, as shown in Figure 5

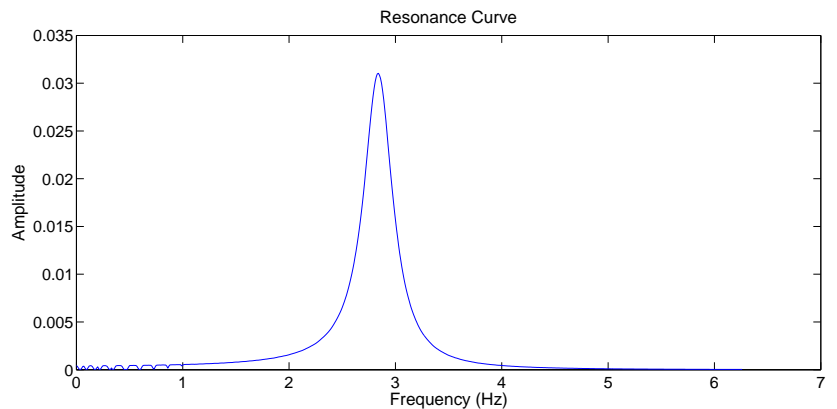


Figure 5: Resonance curve of forced oscillation

There is only one frequency that take the amplitude of

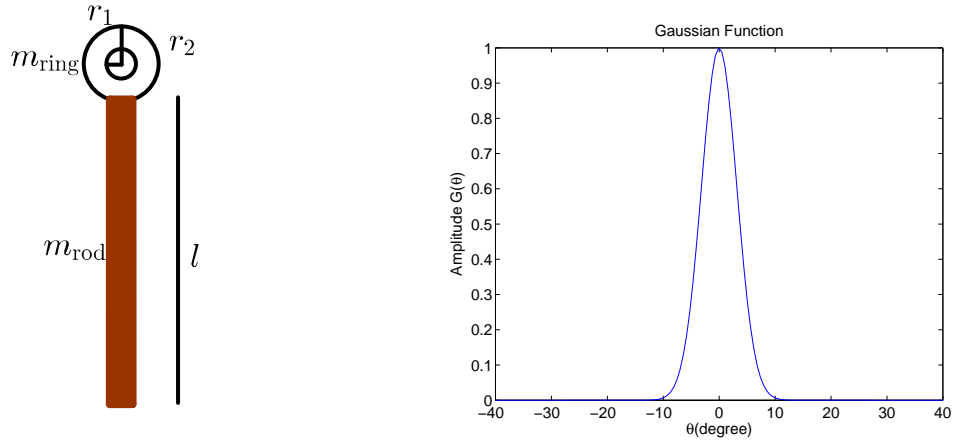


Figure 6: (Left)The illustration of the pendulum. (Right) Gaussian function

the oscillation to be large and gives undamped oscillation. That frequency is called resonance frequency.

But if we talk about the magnetic pendulum in this study, as we said earlier, we observe that large amplitude undamped oscillation occur not only at resonance frequency but also at other certain frequency. And sinusoidal force in this case is causing from passing AC through electromagnet that create magnetic field with north pole alternate with south pole. The equation of motion of magnetic pendulum is

$$I\ddot{\theta} + mgl \sin \theta + bl\dot{\theta} = F(\theta) \sin(\omega_f t + \phi_f) \quad (14)$$

In this case, we need to introduce the moment of inertia of this pendulum, because the our apparatus is the physical pendulum as Figure 6 (Left) then

$$I = I_{\text{ring at end}} + I_{\text{rod at end}} + \text{parallel axis contribution} \quad (15)$$

$$I = \frac{1}{2}m_{\text{ring}}(r_1^2 + r_2^2) + \frac{1}{3}m_{\text{rod}}l^2 + m_{\text{rod}}r_2^2 \quad (16)$$

and we cannot approximate  $\sin(\theta) \approx \theta$ , since the angle isn't small as it have been. And the term  $F(\theta)$  is the  $FG(\theta)$ , while  $F$  is the force amplitude and  $G(\theta)$  is the gaussian function. As Figure 6 (Right)

Term  $\phi_f$  is added due to the initial phase of the function generator.

Since equation of motion in equation (14) isn't linear differential equation, the exact solution doesn't exist. There is approximate solution but it is quite difficult to solve analytically. We can solve this equation by using numerical calculation and obtain the numerical solution that have only the numeral. We can plot solution to see trend of the solution. To calculate numerically second order ODE, we can split into two first order ODE.

$$\begin{aligned} \frac{d\dot{\theta}}{dt} &= -\frac{mgl}{I} \sin \theta - \frac{bl}{I} \dot{\theta} + \frac{Fl}{I} \sin(\omega_f t + \phi_f) \\ \frac{d\theta}{dt} &= \dot{\theta} \end{aligned}$$

And using the numerical method that calculate the differentiate, such as 4th order Runge-Kutta (RK4). We use this method because of it have the most accuracy compare with computer cost. Denote that  $f(x, y)$  is the slope at  $(x, y)$ . RK4 method using four slope ( $k_1 - k_4$ ) and weight to be the average slope that use to predict next point.

$$\begin{aligned} k_1 &= f(x_0, y_0) \\ k_2 &= f\left(x_0 + \frac{h}{2}, y_0 + \frac{h}{2}k_1\right) \\ k_3 &= f\left(x_0 + \frac{h}{2}, y_0 + \frac{h}{2}k_2\right) \\ k_4 &= f(x_0 + h, y_0 + hk_3) \\ y_1 &= y_0 + \frac{h}{6}(k_1 + 2k_2 + 2k_3 + k_4) \end{aligned}$$

The key concept of large amplitude undamped oscillation is that when the pendulum begins at large amplitude and go to the interaction zone if the pendulum gain energy from the driving force enough to compensate the losing energy from drag force, the oscillation will be undamp and can visualize as Figure 7 that plus side is gaining energy and minus sign is losing energy.

But saying that doesn't quite true, it should add the word "at asymptotic time" because at the transient time the pendulum doesn't oscillate undamped evenly. It seem to be undamped oscillation but the amplitude is not the same, it up and down until it is in steady state. Therefore at asymptotic time the system will oscillate undamped.

The method how we study is first of all we need the data in the experiment obtained by recorded the video in 120 frames per second, and using MATLAB to track the pendulum and obtain data. The reason why we use MAT-

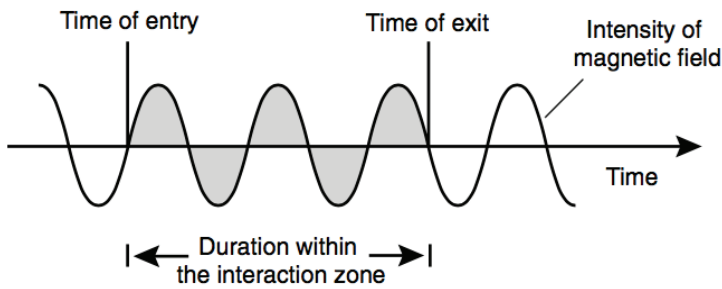


Figure 7: The visualization of how the pendulum stay undamped

LAB instead of Tracker program. Because when we track in Tracker, the position of the pendulum shift little by little, after that the tracking position is missing as shown in Figure 8 (Left). Therefore we develop the graphic user interface (GUI) in MATLAB program as shown in Figure 8 (Right) to track the position of the pendulum instead.

When we have real data we need to know the parameter in our model, such as drag coefficient. We use the numerical simulation, RK4 in this case, to estimate the parameter by matching with real data. We also develop the GUI MATLAB program for estimating the parameter easily as shown in Figure 9

After obtain parameter, we will simulate to find the condition that is large amplitude undamped oscillation. And compare with the real experiment.

## RESULTS

The result from finding parameter is that the linear drag coefficient is about 0.8 and quadratic drag coefficient is about 0.01 as shown in Figure 9 .

The result from experiment is that the large amplitude undamped oscillation occur at frequency equal to 10-20 Hz which has amplitude equal to 12-24 degree. As in figure 10

And from the results show that at difference initial phase of driving force, the results of the experiment is different. We cannot know initial phase of driving force exactly what it is. It affects the result that at one initial phase it is undamped oscillation, while at other one this result isn't undamped oscillation as shown in Figure 11

But in the numerical simulation, we found that the large amplitude undamped oscillation is at frequency 3.78 and 5.41 Hz with amplitude equal to 15 and 16 degree as shown in Figure 12

There are several drawbacks in this experiment. First is the friction on the system. Since this pendulum arm is the physical pendulum, the friction is large. When the friction is large, it means that the energy losing from the system is large. Therefore the system can't sustain the undamped behavior. Causing that we can't find the large amplitude undamped oscillation at higher initial angular displacement. Second problem is unknowing initial

phase of driving force. Therefore we have to try several times to occur large amplitude undamped oscillation. The key problem is that we can't know and control the initial phase of driving force. Resulting in we may missing some initial angular displacement that make large amplitude undamped oscillation and hard to analysis. The last problem is that the waveform of the function generator at low frequency isn't seem to be sine wave. It may be the result of function generator cutt a square wave to be sine wave, but in lower frequency it doesn't have efficiency enough. So the sine wave is not pure sine wave and when it is amplified the wave form looks terribly. The key is that this pendulum has the natural frequency about 0.76 Hz. And we cannot generate the wave that is pure sine wave at low frequency as shown in Figure 13. As you can see this is not sine wave at all.

## SUMMARY

The experiment shows that the large amplitude undamped oscillation occurs at frequency 10 and 20 Hz and has amplitude at 12 and 24 degree respectively.

There are several drawbacks that make it is hard to analysis. Those are large riction in system, unknowing initial phase of driving force and also it is uncontrollable, and last one is function generator can't generate sine wave, which is pure sine wave at low frequency.

The numerical simulation from our model can simulate the undamped oscillation that occur at frequency 3.78 and 5.41 Hz. But cannot be agreement well with real experiment. Therefore the further model need to be developed.

## ACKNOWLEDGMENTS

We would like to thank Mr. Suriya from ISPT to make the intrument in research and also thank Aj. Chaiwat to give us suggestions about oscilloscope, Peera for lending us some wire and giving suggestion on nonlinear motion. Finally, we would like to thank the members of MCSC group to make the colorful working environment.

## REFERENCES

- Damgov, V. Popov, I., 2000, Discrete oscillations and multiple attractors in kick-excited system: Discrete Dynamics in Nature and Society, **4**, no. 2, 99–124.
- Tennenbeum, J., 2005, Amplitude quantization as an elementary property of microscopic vibrating systems. 21st Century Science & Techonology.

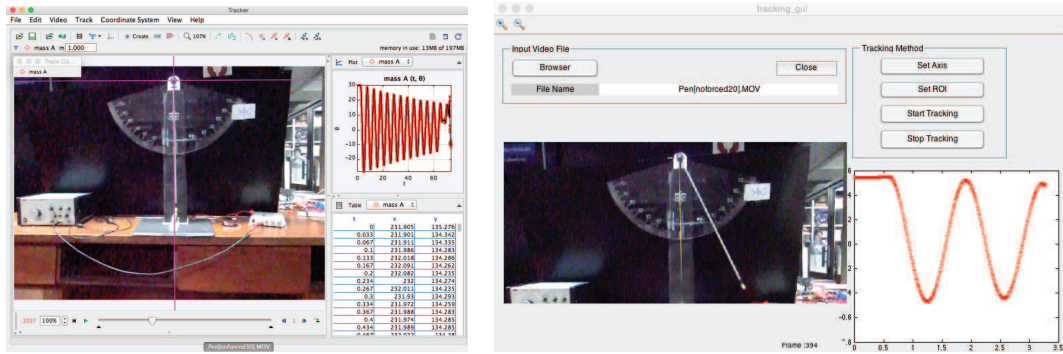


Figure 8: (Left) Drawback of Tracker program. (Right) GUI tracking program

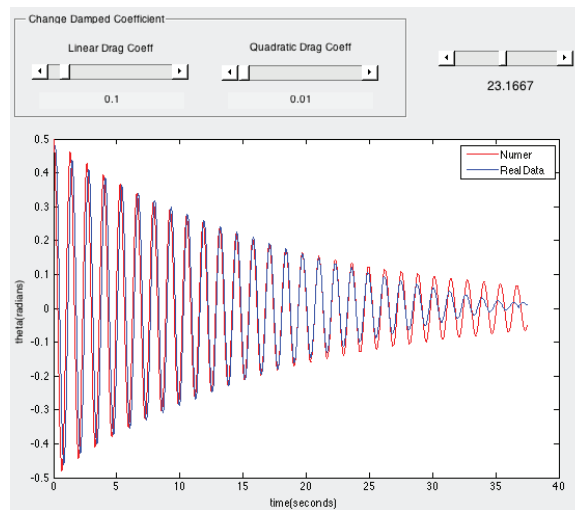


Figure 9: GUI for estimating parameter in MATLAB

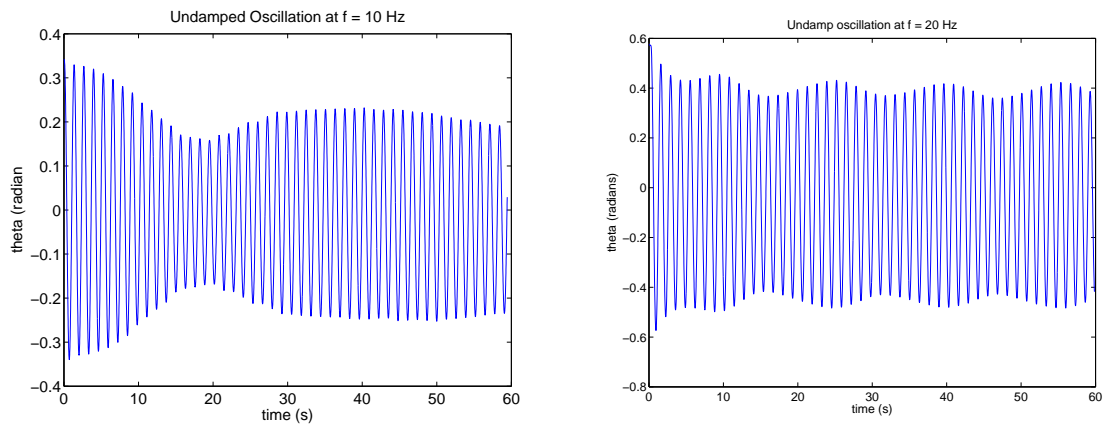


Figure 10: Undamped oscillation at frequency 10 Hz with amplitude 12 degrees (left) and at frequency 20 Hz with amplitude 24 degrees (right)

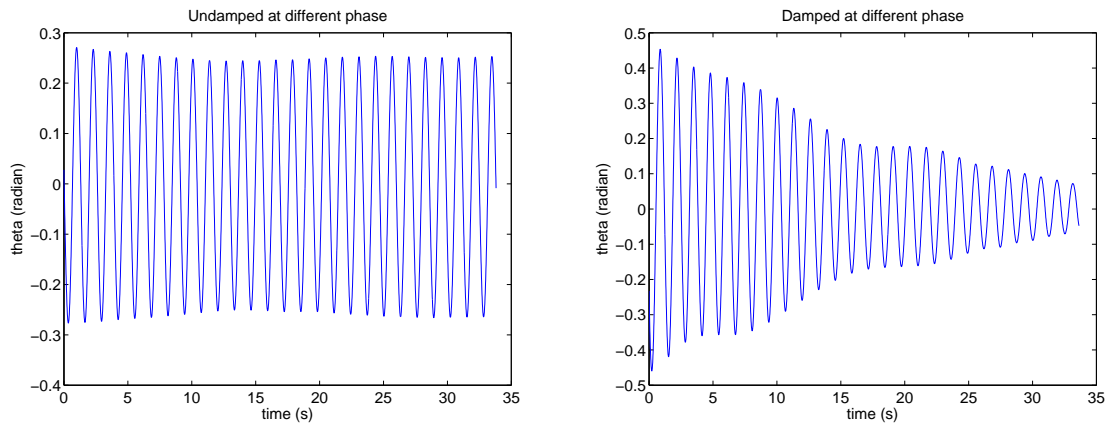


Figure 11: The difference between two figures is the difference in phase, the rest is the same

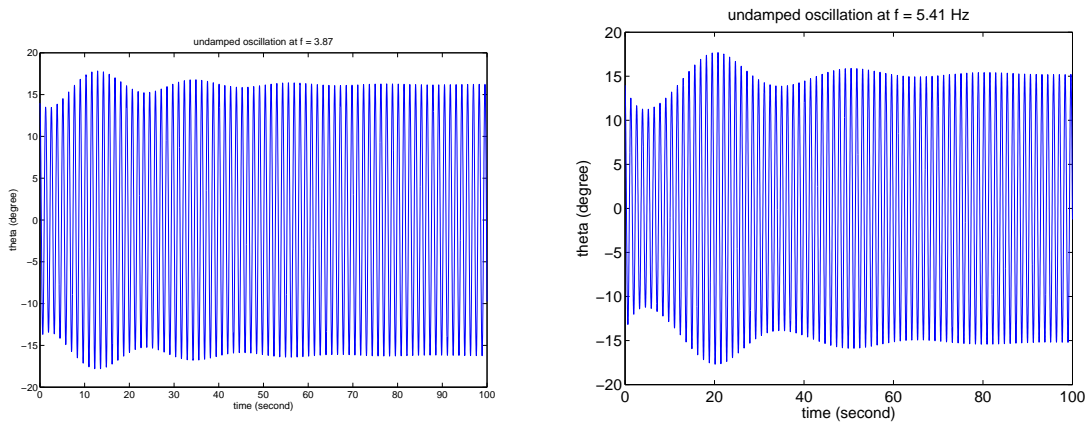


Figure 12: Undamped oscillation at frequency 3.78 Hz with amplitude 15 degrees (left) and at frequency 5.41 Hz with amplitude 16 degrees (right)

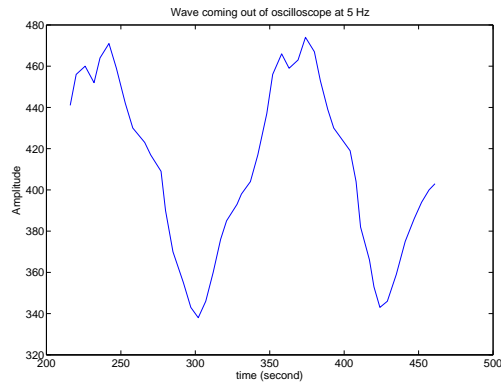


Figure 13: The signal from oscilloscope at low frequency (5 Hz)



# PML formulation for full-waveform modeling of P-SV wave propagation

*Chaiwoot Boonyasiriwat*

## ABSTRACT

Perfectly matched layer (PML) is the most widely used boundary layer for absorbing wavefield energy at the domain boundary to reduce spurious reflections. In this report I presents the PML formulation of the P-SV elastic wave equations for full-waveform modeling using explicit finite-difference method. A free surface boundary crucial for surface-wave modeling is also described.

## INTRODUCTION

Numerical modeling has been an essential tool for research in seismology for many decades. To simulate seismic wave propagation, an acoustic or elastic wave equation is numerically solved using a numerical method, e.g., finite-difference or finite-element method. In exploration seismology, the domain size is in the order of tens of kilometers. To avoid spurious reflections from the domain boundary, an absorbing boundary condition or layer is usually applied. The most widely used absorbing boundary layer is PML (Berenger, 1994).

In this report, I present a PML formulation for modeling of P-SV wave equations in the velocity-stress form used by Levander (1988). The PML formulation is then solved by an explicit finite-difference method to simulate seismic body and surface wave propagation in a synthetic model.

## PML FORMULATION OF P-SV WAVE EQUATIONS

The P-SV wave equations in the velocity-stress form are given by

$$\rho \frac{\partial u}{\partial t} = \frac{\partial \tau_{xx}}{\partial x} + \frac{\partial \tau_{xz}}{\partial z}, \quad (1)$$

$$\rho \frac{\partial w}{\partial t} = \frac{\partial \tau_{zx}}{\partial x} + \frac{\partial \tau_{zz}}{\partial z}, \quad (2)$$

$$\frac{\partial \tau_{xx}}{\partial t} = (\lambda + 2\mu) \frac{\partial u}{\partial x} + \lambda \frac{\partial w}{\partial z}, \quad (3)$$

$$\frac{\partial \tau_{zz}}{\partial t} = (\lambda + 2\mu) \frac{\partial w}{\partial z} + \lambda \frac{\partial u}{\partial x}, \quad (4)$$

$$\frac{\partial \tau_{xz}}{\partial t} = \mu \left( \frac{\partial u}{\partial z} + \frac{\partial w}{\partial x} \right), \quad (5)$$

where  $u$  and  $w$  are particle velocities in  $x$  and  $z$  directions,  $\tau_{xx}$ ,  $\tau_{zz}$  are normal stresses,  $\tau_{xz} = \tau_{zx}$  is shear stress,  $\lambda$  and  $\mu$  are the Lamé's parameters, and  $\rho$  is the mass density.

Equations 1 and 2 are the equation of motion obtained by the application of the Newton's second law of motion. Equations 3-5 are the constitutive laws that relate the wavefields to the material properties.

The first step in the process of deriving the PML formulation is to apply the temporal Fourier transform to the wave equations 1-5. This yields

$$-i\omega\rho\tilde{u} = \frac{\partial\tilde{\tau}_{xx}}{\partial x} + \frac{\partial\tilde{\tau}_{xz}}{\partial z}, \quad (6)$$

$$-i\omega\rho\tilde{w} = \frac{\partial\tilde{\tau}_{zx}}{\partial x} + \frac{\partial\tilde{\tau}_{zz}}{\partial z}, \quad (7)$$

$$-i\omega\tilde{\tau}_{xx} = (\lambda + 2\mu)\frac{\partial\tilde{u}}{\partial x} + \lambda\frac{\partial\tilde{w}}{\partial z}, \quad (8)$$

$$-i\omega\tilde{\tau}_{zz} = (\lambda + 2\mu)\frac{\partial\tilde{w}}{\partial z} + \lambda\frac{\partial\tilde{u}}{\partial x}, \quad (9)$$

$$-i\omega\tilde{\tau}_{xz} = \mu\left(\frac{\partial\tilde{u}}{\partial z} + \frac{\partial\tilde{w}}{\partial x}\right), \quad (10)$$

where  $\tilde{u}, \tilde{w}, \tilde{\tau}_{xx}, \tilde{\tau}_{xz}, \tilde{\tau}_{zz}$  are the Fourier transforms of  $u, w, \tau_{xx}, \tau_{xz}, \tau_{zz}$ , respectively,  $i = \sqrt{-1}$ , and  $\omega$  is the angular frequency. Note that the material properties,  $\rho, \lambda, \mu$  are assumed to be time-independent.

The next step is to apply analytic continuation the frequency-domain wave equations 6-10. We then obtain

$$-i\omega\rho\tilde{u} = \left(\frac{1}{1 + \frac{i\sigma_x}{\omega}}\right)\frac{\partial\tilde{\tau}_{xx}}{\partial x} + \left(\frac{1}{1 + \frac{i\sigma_z}{\omega}}\right)\frac{\partial\tilde{\tau}_{xz}}{\partial z}, \quad (11)$$

$$-i\omega\rho\tilde{w} = \left(\frac{1}{1 + \frac{i\sigma_x}{\omega}}\right)\frac{\partial\tilde{\tau}_{zx}}{\partial x} + \left(\frac{1}{1 + \frac{i\sigma_z}{\omega}}\right)\frac{\partial\tilde{\tau}_{zz}}{\partial z}, \quad (12)$$

$$-i\omega\tilde{\tau}_{xx} = (\lambda + 2\mu)\left(\frac{1}{1 + \frac{i\sigma_x}{\omega}}\right)\frac{\partial\tilde{u}}{\partial x} + \lambda\left(\frac{1}{1 + \frac{i\sigma_z}{\omega}}\right)\frac{\partial\tilde{w}}{\partial z}, \quad (13)$$

$$-i\omega\tilde{\tau}_{zz} = (\lambda + 2\mu)\left(\frac{1}{1 + \frac{i\sigma_x}{\omega}}\right)\frac{\partial\tilde{w}}{\partial z} + \lambda\left(\frac{1}{1 + \frac{i\sigma_z}{\omega}}\right)\frac{\partial\tilde{u}}{\partial x}, \quad (14)$$

$$-i\omega\tilde{\tau}_{xz} = \mu\left[\left(\frac{1}{1 + \frac{i\sigma_x}{\omega}}\right)\frac{\partial\tilde{u}}{\partial z} + \left(\frac{1}{1 + \frac{i\sigma_z}{\omega}}\right)\frac{\partial\tilde{w}}{\partial x}\right], \quad (15)$$

where  $\sigma_x$  and  $\sigma_z$  are the PML damping coefficients which are positive and nonzero within the PML zone, and are zero in the physical domain.

Rearranging equations 11-15 yields

$$\left(-i\omega + \sigma_x + \sigma_z + \frac{\sigma_x\sigma_z}{-i\omega}\right) \rho\tilde{u} = \left(1 + \frac{\sigma_z}{-i\omega}\right) \frac{\partial\tilde{\tau}_{xx}}{\partial x} + \left(1 + \frac{\sigma_x}{-i\omega}\right) \frac{\partial\tilde{\tau}_{xz}}{\partial z} \quad (16)$$

$$\left(-i\omega + \sigma_x + \sigma_z + \frac{\sigma_x\sigma_z}{-i\omega}\right) \rho\tilde{w} = \left(1 + \frac{\sigma_z}{-i\omega}\right) \frac{\partial\tilde{\tau}_{zx}}{\partial x} + \left(1 + \frac{\sigma_x}{-i\omega}\right) \frac{\partial\tilde{\tau}_{zz}}{\partial z} \quad (17)$$

$$\left(-i\omega + \sigma_x + \sigma_z + \frac{\sigma_x\sigma_z}{-i\omega}\right) \tilde{\tau}_{xx} = (\lambda + 2\mu) \left(1 + \frac{\sigma_z}{-i\omega}\right) \frac{\partial u}{\partial x} + \lambda \left(1 + \frac{\sigma_x}{-i\omega}\right) \frac{\partial w}{\partial z} \quad (18)$$

$$\left(-i\omega + \sigma_x + \sigma_z + \frac{\sigma_x\sigma_z}{-i\omega}\right) \tilde{\tau}_{zz} = \lambda \left(1 + \frac{\sigma_z}{-i\omega}\right) \frac{\partial u}{\partial x} + (\lambda + 2\mu) \left(1 + \frac{\sigma_x}{-i\omega}\right) \frac{\partial w}{\partial z} \quad (19)$$

$$\left(-i\omega + \sigma_x + \sigma_z + \frac{\sigma_x\sigma_z}{-i\omega}\right) \tilde{\tau}_{xz} = \mu \left[ \left(1 + \frac{\sigma_x}{-i\omega}\right) \frac{\partial u}{\partial z} + \left(1 + \frac{\sigma_z}{-i\omega}\right) \frac{\partial w}{\partial x} \right]. \quad (20)$$

Let's introduce the auxilliary fields

$$-i\omega\tilde{\phi}_u = \tilde{u}, \quad (21)$$

$$-i\omega\tilde{\phi}_w = \tilde{w}, \quad (22)$$

$$-i\omega\tilde{\psi}_{xx} = \tilde{\tau}_{xx}, \quad (23)$$

$$-i\omega\tilde{\psi}_{zz} = \tilde{\tau}_{zz}, \quad (24)$$

$$-i\omega\tilde{\psi}_{xz} = \tilde{\tau}_{xz}. \quad (25)$$

The last step in the process is to apply invert Fourier transform to the wave equations 16-20. This results in the PML formulation given by

$$\rho \left[ \left( \frac{\partial}{\partial t} + \sigma_x + \sigma_z \right) u + \sigma_x \sigma_z \phi_u \right] = \left( \frac{\partial\tau_{xx}}{\partial x} + \sigma_z \frac{\psi_{xx}}{\partial x} \right) \left( \frac{\partial\tau_{xz}}{\partial z} + \sigma_x \frac{\psi_{xz}}{\partial z} \right), \quad (26)$$

$$\rho \left[ \left( \frac{\partial}{\partial t} + \sigma_x + \sigma_z \right) w + \sigma_x \sigma_z \phi_w \right] = \left( \frac{\partial\tau_{zx}}{\partial x} + \sigma_z \frac{\psi_{zx}}{\partial x} \right) \left( \frac{\partial\tau_{zz}}{\partial z} + \sigma_x \frac{\psi_{zz}}{\partial z} \right), \quad (27)$$

$$\left( \frac{\partial}{\partial t} + \sigma_x + \sigma_z \right) \tau_{xx} + \sigma_x \sigma_z \psi_{xx} = (\lambda + 2\mu) \left( \frac{\partial u}{\partial x} + \sigma_z \frac{\phi_u}{\partial x} \right) + \mu \left( \frac{\partial w}{\partial z} + \sigma_x \frac{\phi_w}{\partial z} \right), \quad (28)$$

$$\left( \frac{\partial}{\partial t} + \sigma_x + \sigma_z \right) \tau_{zz} + \sigma_x \sigma_z \psi_{zz} = \lambda \left( \frac{\partial u}{\partial x} + \sigma_z \frac{\phi_u}{\partial x} \right) + (\lambda + 2\mu) \left( \frac{\partial w}{\partial z} + \sigma_x \frac{\phi_w}{\partial z} \right), \quad (29)$$

$$\left( \frac{\partial}{\partial t} + \sigma_x + \sigma_z \right) \tau_{xz} + \sigma_x \sigma_z \psi_{xz} = \mu \left[ \left( \frac{\partial u}{\partial z} + \sigma_x \frac{\phi_u}{\partial z} \right) + \left( \frac{\partial w}{\partial x} + \sigma_z \frac{\phi_w}{\partial x} \right) \right]. \quad (30)$$

The auxilliary fields also have the time evolution equations, given by

$$\frac{\partial \phi_u}{\partial t} = u, \quad (31)$$

$$\frac{\partial \phi_w}{\partial t} = w, \quad (32)$$

$$\frac{\partial \psi_{xx}}{\partial t} = \tau_{xx}, \quad (33)$$

$$\frac{\partial \psi_{zz}}{\partial t} = \tau_{zz}, \quad (34)$$

$$\frac{\partial \psi_{xz}}{\partial t} = \tau_{xz}. \quad (35)$$

Solving equations 26-35, one can simulate P-SV wave propagation in two dimensions without spurious boundary reflections. Nonetheless, to simulate surface wave propagation along the free surface, we still need to apply a free surface boundary condition whose details are given in the next section.

## FREE SURFACE BOUNDARY CONDITION

The Earth's surface, the interface between air and solid rocks or sediments, is usually considered as a free surface at which the normal and shear stresses perpendicular to the interface are zero. In the case of a horizontal free surface,  $\tau_{xz} = \tau_{zz} = 0$  (Robertsson, 1996). Equations 4 and 5 then reduce to

$$\frac{\partial u}{\partial z} = -\frac{\partial w}{\partial x}, \quad (\tau_{xz} = 0) \quad (36)$$

$$\frac{\partial w}{\partial z} = -\frac{\lambda}{\lambda + 2\mu} \frac{\partial u}{\partial x}, \quad (\tau_{zz} = 0) \quad (37)$$

which are used as constraints at the free surface. When a staggered grid is used, these two constraints cannot be both utilized at the same time. This is due to the fact that normal stresses ( $\tau_{xx}$  and  $\tau_{zz}$ ) and the shear stress ( $\tau_{xz}$ ) are located at different locations within the grid cell. If the horizontal free surface passes through the normal stresses, it will not pass through the shear stress. So, in this case, only  $\tau_{zz} = 0$  and equation 37 is solely applied.

## REFERENCES

- Berenger, J., 1994, A perfectly matched layer for the absorption of electromagnetic waves: *Journal of Computational Physics*, **114**, 185–200.
- Levander, A., 1988, Fourth-order finite-differences p-sv seismograms: *Geophysics*, **53**, 1425–1436.
- Robertsson, J. O. A., 1996, A numerical free-surface condition for elastic/viscoelastic finite-difference modeling in the presence of topography: *Geophysics*, **61**, 1921–1934.